Scuola Superiore
Sant'Anna
di Studi Universitari e di Perfezionamento

Anno Accademico
2014-2015

Corso di perfezionamento/dottorato
Telecomunicazioni

Distributed Optical Fiber Radiation and Temperature Sensing at High Energy Accelerators and Experiments

Autore
Iacopo Toccafondo

SSSA Tutor
Prof. Fabrizio Di Pasquale

CERN Tutor
Dr. Markus Brugger

To my family

Contents

List of Figures xiv

List of Tables xv

1 Introduction 1

2 Fundamentals of dosimetry 7

2.1 Radiation matter interaction 7

2.1.1 Ionizing radiation 7

2.1.2 Neutral Radiation - Indirectly Ionizing Particles 11

2.1.3 Non-ionizing Energy Loss 15

2.2 Quantification of radiation levels and radiation damage in materials 16

2.2.1 Kerma and total ionizing dose 16

2.2.2 NIEL 17

2.3 Radiation detectors and dose measurements 18

2.3.1 Gas filled detectors 19

2.3.2 Scintillation detectors 20

2.3.3 Semiconductor detectors 20

2.3.4 The LHC Radiation Monitoring System - RadMon 21

2.4 Radiation environment at CERN's accelerator complex 22

2.5 Monte Carlo simulation package: FLUKA 24

3 Radiation effects on Silica-based optical fibers 27

3.1 Silica based glasses properties 27

3.2 Radiation effects at the microscopic and macroscopic levels 29

3.2.1 Radiation-damage processes 29

3.2.2 Radiation induced macroscopic changes 31

3.3 Influence of the fiber structure and composition on its radiation response . . . 33
3.3.1 Point defects in optical fibers . . . 33
3.3.2 Pure-Silica Core fibers (PSC) . . . 35
3.3.3 Germanium doped (Ge-doped) . . . 36
3.3.4 Phosphorus doped (P-doped) . . . 37
3.3.5 Aluminum doped (Al-doped) . . . 38
3.3.6 SMF vs MMF . . . 38
3.4 Radiative environment influence on the fiber's radiation response . 39
3.4.1 Dose dependence of the RIA . . . 39
3.4.2 Dose rate dependence of the RIA . . . 39
3.4.3 Temperature dependence of the RIA . . . 40
3.5 Application parameters influence on the fiber's radiation response 41
3.5.1 Wavelength influence . . . 41
3.5.2 Launched power influence . . . 41
3.5.3 Fiber history and pre-treatments influence . . . 42
3.5.4 Radiation type dependence . . . 42
3.6 Optical fiber's radiation response theoretical models . . . 44
3.6.1 Linear model . . . 44
3.6.2 Power law model . . . 44
3.6.3 Semi-empirical model . . . 45
3.6.4 First order kinetic model . . . 45

4 Optical fiber distributed dosimeters based on (RIA) 47

4.1 Spontaneous light scattering . . . 47
4.1.1 Perturbed wave equation . . . 49
4.1.2 Rayleigh scattering . . . 51
4.2 Optical fiber sensors . . . 52
4.3 Distributed fiber optics sensing . . . 54
4.3.1 Optical Time Domain Reflectometry (OTDR) . . . 56
4.3.2 Performance Parameters of DOFS . . . 60
4.3.3 Optical Pulse Coding Techniques for OTDR . . . 61

4.4 Distributed optical fiber radiation sensor (DOFRS) . . . 65
4.4.1 Methodology and requirements for a DORFS at high energy physics accelerator and experiments facilities . . . 66

5 ^{60}Co characterization of selected P-doped fibers 69
5.1 Experimental setup . . . 69
5.1.1 The ^{60}Co source . . . 69
5.1.2 Optical fiber sample preparation . . . 70
5.1.3 Measurement equipment and irradiation conditions . . . 72
5.2 Discrete and spectral measurements results . . . 74
5.2.1 Multimode fibers (MMF) radiation response . . . 74
5.2.2 Single mode fibers (SMF) radiation response . . . 80
5.3 Distributed measurements . . . 88
5.3.1 Experimental setup . . . 89
5.3.2 Results . . . 90
5.4 Limitations of commercially available P-codoped fibers . . . 92
5.4.1 Radiation sensitive optical fiber custom design . . . 93

6 Distributed OTDR based radiation sensing at CHARM 99
6.1 Cern High energy AcceleRator Mixed field facility (CHARM) . . . 99
6.1.1 The mixed-field radiation environment . . . 100
6.2 Experimental setup . . . 103
6.3 Distributed radiation measurements results . . . 105
6.3.1 Pulse duration: 5 ns . . . 105
6.3.2 Pulse duration: 10 ns . . . 115
6.4 In-beam proton characterization . . . 118
6.4.1 Experimental setup . . . 118
6.4.2 Results . . . 122

7 Distributed temperature measurements at CHARM 129
7.1 Temperature dependence of spontaneous Raman . . . 129
7.2 Spontaneous Raman Scattering in Optical Fibers . . . 130
7.3 The Raman Distributed Temperature Sensor (RDTS) . . . 136
7.3.1 Single-ended RDTS . . . 138

7.3.2 Double-ended RDTS 140
7.3.3 Limitations of the RDTS 143
7.4 Optical Pulse Coding for RDTS 144
7.5 Results of Raman distributed temperature measurements 145
7.5.1 Experimental setup 146
7.5.2 Temperature profile 148

8 Final discussion and further developments **155**

Bibliography **161**

List of Publications **171**

Acknowledgements **174**

List of Figures

2.1 $E > 100$ MeV hadron processes cascade 9
2.2 Mean energy loss rate in various materials [23] 10
2.3 Depth dependence of the deposited dose for different radiation type, including the Bragg peak for protons and carbon ions 11
2.4 Cross sections for different photon-material interaction mechanisms as function of photon energy [25] 14
2.5 Relative importance of the three main types of γ-ray interactions [26] 14
2.6 Displacement damage in Silicon for neutrons, protons, pions and electrons [28] 18
2.7 Operation regions of gas filled detectors [24] 19
2.8 CERN Accelerator Complex [29] 23
2.9 Particle energy spectra representative for tunnel areas in the LHC [9] 24
2.10 FLUKA's geometry editor: 3D topview of LHC IR7 Dispersion Suppressor 25

3.1 Structure of amorphous silica, showing the silicon (Si) atoms (in grey) and the binding oxygen (O) atoms (in back) 28
3.2 Comparison between (a) ideal pure-silica glass structure and (b) defective pure-silica glass structure [14] 29
3.3 Diagram of the most relevant radiation-damage effects in glass material [27] 30
3.4 Radiation-induced attenuation spectra of pure silica and doped silica core fibres measured one hour after an irradiation of 10^5 rad [36] 32
3.5 Representation of different point defects. The arrows indicate the electron spins and the ellipsoids the orbit [40] 35

3.6 Absorption bands associated with different Si-related point defect structures[14] 36
3.7 Absorption bands associated with different Ge-related point defect structures[14] 37
3.8 Absorption bands associated with different P-related point defect structures[14] 38

4.1 Spectral components resulting from light scattering in an inhomogeneous medium 48
4.2 Block diagram of a typical OTDR system (PD: Photo-detector, ADC: Anolog-to-digital converter) [79] 57
4.3 Propagation of pulse and its respective backscattering along an optical fiber in conventional OTDR technique) [79] 58
4.4 Measured temperature with (a) 255 bit coded and (b) conventional DTS Inset: LD output (first 30 bits of 255 code pattern)[92] 64
4.5 Increase in measurement range as a function of code length [92] . . 64
4.6 DOFRS system schematic block diagram 67

5.1 Experimental setup for irradiation tests on optical fibers using the Gammamat TK1000 ^{60}Co source at Fraunhofer INT [60] 70
5.2 The Gammamat TK1000 ^{60}Co irradiation system with reels mounted on it 71
5.3 Different size aluminium reels for fiber sample spooling 72
5.4 RIA as function of absorbed dose for different dose rates at 830 nm 75
5.5 RIA as function of absorbed dose for different dose rates at 1312 nm 75
5.6 Spectral response at 1.02 kGy 77
5.7 RIA as function of absorbed dose for different dose rates at 830 nm 78
5.8 RIA as function of absorbed dose for different dose rates at 1312 nm 79
5.9 RIA as function of absorbed dose up to 1 kGy, linear scale, 830 nm 79
5.10 Spectral response at 300 Gy 80
5.11 RIA as function of total absorbed dose for different dose rates at 1312 nm 81
5.12 RIA as function of total absorbed dose for different dose rates at 1570 nm 82
5.13 Spectral response of the Draka at 1 kGy 83

5.14 Fiber X, double logarithmic: RIA as function of total absorbed dose at 1312 nm and 1570 nm, dose rate: 153 mGy/s 84
5.15 Fiber X, linear: RIA as function of total absorbed dose at 1312 nm and 1570 nm, dose rate: 153 mGy/s 85
5.16 Spectral response for fiber X at 1 kGy 85
5.17 RIA as function of absorbed dose in the highly radiation sensitive Al and P codoped fibers at 1550 nm, 30°C 86
5.18 Ratio between the attenuation measurements carried out at SCK-CEN and those at Fraunhofer INT 87
5.19 Ratio of the spectral measurements carried out at SCK-CEN and those at Fraunhofer INT 87
5.20 Spectral response at almost 60 kGy 88
5.21 Experimental setup for the distributed measurements on a fiber under ^{60}Co irradiation 89
5.22 Schematic layout of the fiber's irradiation for distributed measurements 90
5.23 Zoom of OTDR trace at λ_1 = 850 for a total absorbed dose of about 300 Gy 91
5.24 Zoom of OTDR trace at λ_2 = 1300 fora total absorbed dose of about 300 Gy 91
5.25 Scanning Electron Microscope picture of the HACC-Ge fiber [98] . 94
5.26 Scanning Electron Microscope picture of the HACC-Ge fiber [98] . 95
5.27 RIA spectra evolution of the PCe a) and the P-doped b) optical fibers irradiated at room temperature with a dose rate of 5 krad/s up to a a dose of 100 Mrad [99] 96
5.28 RIA as function of the dose for the PCe optical fiber and a P-codoped optical fiber both irradiated at room temperature with a dose rate of 50 Gy/s up to a a dose of 1 MGy, λ = 500nm (adapted from [100]) 97

6.1 (a) 3D view of the facility, (b) FLUKA geometry for the target area: Racks 1 to 18 are the regions representing the test positions. The blue and grey plates are the iron and concrete movable shieldings [101] 100

6.2 HEH flux (cm^{-2}/h) at different locations for the three different target configurations [101] 101
6.3 HEH flux (cm^{-2}/h) at different locations for the different shielding configurations [101] 101
6.4 Fiber layout for distributed radiation sensing at CHARM 103
6.5 Fiber layout for distributed radiation sensing at CHARM 104
6.6 j-fiber, OTDR traces at different moments in time 106
6.7 Savitzky-Golay filtering effect on j-fiber's OTDR trace 107
6.8 j-fiber OTDR trace, direction 1 108
6.9 j-fiber OTDR trace, direction 2 108
6.10 j-fiber, dose profile as function of the distance after 35 hours of irradiation, $\lambda_1 = 850$ nm 109
6.11 j-fiber, dose profile as function of the distance after 35 hours of irradiation, $\lambda_2 = 1300$ nm 110
6.12 Dose profile estimated with the j-fiber at $\lambda = 850$ nm compared to RadFETs measurements 111
6.13 OFS MMF, dose profile as function of the distance after 35 hours of irradiation, $\lambda_1 = 850$ nm 113
6.14 OFS MMF, dose profile as function of the distance after 35 hours of irradiation, $\lambda_2 = 1300$ nm 113
6.15 Draka SMF, dose profile as function of the distance after 35 hours of irradiation, $\lambda = 1550$ nm 114
6.16 j-fiber MMF, OTDR trace after about 20 hours of irradiation, $\lambda = 850$ nm 116
6.17 j-fiber MMF, dose profile as function of the distance after about 20 hours of irradiation compared to FLUKA (green) and FLUKA average over 1 m (blue), $\lambda = 850$ nm 117
6.18 j-fiber MMF, dose profile as function of the distance after about 20 hours of irradiation compared to FLUKA (green) and FLUKA average over 1 m (blue), $\lambda = 1300$ nm 117
6.19 Test box holding the plexiglass card on which the fiber sample is taped to 118
6.20 Fiber layout for in-beam measurements at CHARM 119
6.21 In-beam dose map for $1.5 \cdot 10E15$ protons on target in 1 day 120

6.22 Radfet layout for in-beam dose estimation [102] 121
6.23 Radfet dose estimation [102] 121
6.24 Draka SM: RIA as function of the accumulated dose, proton-^{60}CO comparison, λ =~ 1310 nm 123
6.25 Draka SM: RIA as function of the accumulated dose, proton-^{60}CO comparison, λ =~ 1550 nm 124
6.26 Draka SM's proton irradiation response in the linear range, λ = 1310 nm 125
6.27 Draka SM's proton irradiation response in the linear range, λ = 1550 nm 126
6.28 Ratio $RIA_{protons}/RIA_{^{60}Co}$, λ =~ 1310 nm 127
6.29 Ratio $RIA_{protons}/RIA_{^{60}Co}$, λ =~ 1550 nm 128

7.1 Energy level diagrams describing both the Raman Stokes and anti-Stokes scattering 131
7.2 Raman amplification of the Placzek Stokes sideband and simultaneous absorption of the Placzek anti-Stokes sideband, both at T = 0K [104] 133
7.3 Raman gain spectrum for vitreous silica 134
7.4 Raman anti-Stokes signal measured as a function of the fiber temperature. The vertical axis being normalized at room temperature [109] 136
7.5 Generic block diagram of a typical single-ended OTDR-based RDTS temperature sensor 137
7.6 Double-ended RDTS configuration 141
7.7 RIA as function of wavelenth for the Draka radiation tolerant MM fiber, dose rate: 0.23 Gy/s 146
7.8 2D view of the CHARM facility including the path of the radiation tolerant MM fiber 147
7.9 Dose profile along the fiber's path 148
7.10 RDTS control unit and optical fiber setup 148
7.11 Temperature profiles along the radiation tolerant fiber before the beginning and at the end of irradiation 149

7.12 Raman Stokes trace at the beginning of the measurement (t_{START}) and after 24 hours (t_{END}) 150
7.13 Raman anti-Stokes trace at the beginning of the measurement (t_{START}) and after 24 hours (t_{END}) 151
7.14 Temperature values versus time, comparison between the Raman DTS and the PT100 at position 40 m 153
7.15 Temperature standard deviation versus distance 154

List of Tables

5.1 MMF j-fiber, maximum absorbed dose in the linear range for different tolerance values 76
5.2 MMF OFS, maximum absorbed dose in the linear range for different tolerance values 78
5.3 SMF Draka, Maximum total absorbed dose in the linear range for different tolerance values 82

6.1 Comparison of the HEH hardness factor between the LHC and CHARM 102

1 Introduction

During the last two decades the field of optical fiber sensors (OFS) has demonstrated its capabilities to achieve effective measurement systems for a wide range of applications. Thanks to a great variety of advantages over conventional electromechanical sensors, OFS have attracted significant attention and have become more and more interesting for applied research as well as industrial developments. Among the specific properties of optical fiber sensors we may cite their small size, lightweight, immunity to electromagnetic and mechanical flexibility. One particularly interesting advantage of optical fiber sensors is their ability to perform distributed measurements of environmental variables such as temperature or strain, representing a unique characteristic which does not have any equivalent in conventional sensing technologies [1][2][3][4].
In combination with a deeper understanding of scattering phenomena in optical fibers, together with the development of advanced time- or frequency-domain interrogation techniques for measuring a fiber's impulse response, the abovementioned advantages of OFS have led to a very large range of applications in several industrial fields including automation, aerospace, aeronautical, industrial plants, inspection of oil and gas systems, modern structural health monitoring, power stations or transportation. In particular, just to cite a few examples, stress and strain monitoring of large buildings or structures as well as leakage detection of oil pipelines or temperature monitoring for fire detection in automotive or railways tunnels have found in optical fiber sensing an ideal monitoring mean [4].

Optical fiber sensors have also attracted the interest of nuclear power plants as well as high energy physics accelerators and experiments. In the first case, the ageing of the electrical cables which are fundamental components of nuclear power plant since they are used to link power instrumentation and equipment for monitoring

and controlling the plant, is a major concern. Such cables are degraded by temperature and ionizing radiation which could cause mechanical property changes, cracking of insulators which could then end up with an electrical failure or even with ignition in the worst case [5]. Distributed OFS would be highly suitable in such cases given their sensing fiber could be easily deployed along the cables and they have the ability to monitor the required physical quantity over long distances. In the second case, in order to predict equipment and material lifetimes at accelerators, accurate radiation dosimetry is highly important and very challenging. Complex, intermediate to partly high radiation fields affect installed electronics, limit equipment lifetimes and eventually alter materials with an underlying mixed radiation field consisting of neutrons, protons, pions, electrons and gamma rays, all over a large range of particle energies and intensities, the latter often pulsed. In the Large Hadron Collider tunnel for example, a dosimeter would need to be capable of measuring Total Ionizing Dose (TID) ranging from a few Gy per year up to 100 kGy per year in a mixed radiation field [6][7][8].
Currently the radiation levels in the LHC tunnels and surrounded shielded areas are monitored by the Radiation Monitoring System (RadMon), which provide the measurement of TID in Silicon Dioxide by means of Radiation-sensing Field-Effect Transistors (RadFETs) along with other the Displacement Damage (DD) and the High Energy Hadrons fluence. The RadMon system has therefore also the purpose of predicting the possible degradation and failure of electronic devices. There are 500 RadMon devices placed in different areas of the LHC tunnel capable of measuring doses up to approximately 5 kGy and their digital data is stored at a rate of 1 Hz [9]. One of the disadvantages of the RadMon system however, is that it can only provide the information about the dose in preselected points along the 27 km LHC tunnel, thus not providing a distributed measurement. It is therefore evident that high energy physics particle accelerators and experiments would strongly benefit from a distributed optical fiber radiation sensing system which would allow for the online monitoring of radiation levels with continuous spatial information about the dose values.
As for any tunnel, fire safety is fundamental at accelerators' tunnels as well. Being able to quickly determine the position with great accuracy of a possible fire is highly important for the fire rescue teams to be able to promptly intervene. Leakage detection of coolants used for superconducting magnets is also fundamental to

quickly localize any fault which would heat the magnets and bring the whole accelerator machine to a stop. An optical fiber-based distributed temperature sensor would be an ideal solution for these applications where the fast and precise measurement of temperature is required over long distances. For the above-mentioned sensing scenarios, the knowledge and understanding of the effects of radiation on optical fibres is essential and has been extensively studied over the last four decades. In particular, it is a known fact that optical fibers exhibit a very high increase of their attenuation when exposed to ionizing radiation [10][11][12][13]. Depending on a fiber's structure and composition the response to radiation will be different. For a given fiber the irradiation environment conditions (for example the dose rate or ambient temperature) as well as the application parameters (for example the launched optical power) might have an important impact on the fiber's radiation response [14]. It is therefore fundamental to wisely select the fiber to be used, according to the specific application which will be characterized by its own specific radiation environment. For example, radiotherapy applications require the in vivo monitoring of the absorbed dose during the cancer treatment with dose values usually ranging from 0.5 Gy to 10 Gy per treatment cycle [15] while on the other hand, as previously mentioned, up to 100 kGy of annual doses can be reached in certain parts of the LHC tunnels. For dosimetry in general, phosphorus-doped fibres which show a linear dose dependence response of the RIA at different wavelengths and an independence from dose rate and temperature [16], are considered to be eligible. One of the first demonstrations of an optical fiber-based dosimeter was already provided by Evans et al. in 1978 [17]. Distributed optical fiber-based dosimetry was then demonstrated and tested for the Tera Electron Volt Energy Superconducting Linear Accelerator (TESLA) Test Facility at DESY Hamburg using Optical Time Domain Reflectometry (OTDR) and germanium-doped multimode (MM) graded index (GI) fibers co-doped with phosphorus [18]. The system was capable of measuring on-line doses down to a few Gy with a local resolution of a few meters, which was acceptable for the specific application. This first demonstration of distributed optical fiber dosimetry, needs to be verified in even more challenging environments like those present at CERN's accelerator complex.

The aim of this Thesis is to investigate the feasibility of an distributed optical

fiber radiation sensing system to be used at high energy physics accelerators and experiments where complex mixed-field environments are present and annual dose values range from a few tens of Gy up to 100 kGy. In particular, after having characterized the response of a selection of optical fibers to ionizing radiation coming from a ^{60}Co source, the results of distributed optical fiber radiation measurements in a mixed-field environment are presented along with method to actually estimate the dose variation. Raman-based optical fiber distributed temperature measurements in a mixed-field environment have also been investigated and are presented in this Thesis work.

The second Chapter of this Thesis introduces the fundamentals of radiation matter interaction, dosimetry, radiation detectors and provides an overview of the radiation environment present at CERN's accelerator complex. A brief summary on the FLUKA Monte Carlo simulation package is also provided. The terminology and concepts explained in this Chapter is necessary to fully understand the results presented later in Chapters 5-7.

The third Chapter provides an overview about the radiation effects on optical fibers. The fundamental effects taking place when a fiber is irradiated are described along with the influences of the fiber's structure and composition, of the radiation environment characteristics and of the application's parameter on the fiber's response to radiation.

The fourth Chapter provides the theory behind optical fiber sensors. In particular, spontaneous light scattering will be explained by means of the perturbed wave equation in Section 4.1 In the following sections, optical fiber sensors with a focus on distributed optical fiber sensing will be presented. The Optical Time Domain Reflectrometry (OTDR) techique will be explained followed by an introduction to distributed optical fiber radiation sensing.

Chapter five of this Thesis work presents the characterization of a selection of Phosphorous-co-doped multi-mode and single mode fibers irradiated at the ^{60}Co of the Fraunhofer-Institut für Naturwissenschaftlich-Technische Trendanalysen (INT) in Euskirchen (Germany). There, the radiation response in terms of Radiation In-

duced Attenuation (RIA) as a function of the accumulated dose has been studied for different dose rates. These characterizations are fundamental to understand whether a chosen fiber is suitable for dosimetry or not. Chapter five also presents some first promising results of distributed measurements also carried out at Fraunhofer INT.

Chapter six deals with distributed optical fiber radiation sensing measurements carried out in a mixed-field radiation environment at the "Cern High energy AcceleRator Mixed field facility" (CHARM). A selection of the fibers previously characterized at Fraunhofer INT under gamma irradiation have been installed at CHARM such that they are irradiated by a mixed particle radiation field with a great variety of dose rates. By means of an OTDR device, distributed measurements of the attenuation profile of the fiber as function of the dose have been performed with different interrogation and acquisition parameters. Based on the previously presented characterizations relating the induced attenuation to the dose and following an accurate processing including a proposed dedicated method to estimate dose variation, dose profiles along the installed fibers' path have been estimated and compared to FLUKA simulations as well as to RadFETs installed at key positions along the fibers. Both the processing methodology as well as the very interesting results are discussed in detail. In the last section of Chapter six, an experiment dedicated to the investigation of the particle type dependence of the RIA is presented. In particular, a P-co-doped single-mode fiber previously characterized under gamma irradiation at Fraunhofer INT has been irradiated by a high-energy proton beam.

Finally, the seventh Chapter first provides the theory behind Raman-based distributed optical fiber sensing and the presents the results from optical fiber distributed temperature measurements carried out in the mixed-field environment of CHARM using a radiation tolerant sensing fiber. The experimental setup will be shown in detail along with the demonstration that reliable temperature measurements in such harsh environments can be carried out.

2 Fundamentals of dosimetry

2.1 Radiation matter interaction

To understand why optical fibers and photonic components may suffer from exposure to nuclear radiation [19][20] it is first important to recall the underlying physics of radiation-matter interactions. Nuclear radiation may exist in a great variety of forms but in the scope of this thesis we may distinguish two main types of radiation: ionizing and non-ionizing radiation. As will be explained in the next subsections, while some particles such as photons are considered to be purely ionizing radiation as they deposit energy in a material mainly through the creation of secondary electrons, other particles such as protons or neutrons are also able to interact with a material by non-ionizing energy loss, for example through atomic displacement processes.

2.1.1 Ionizing radiation

Ionization is the process of adding or removing an electron from a neutral atom, creating an ion. When charged particles such as α, β or protons pass through matter, they strongly interact with the orbital electrons of the material and loose energy. Charged particles can be classified as *directly ionizing* and may be subdivided into two families based on their mass: heavy charged particles such as protons or α particles and light ones such as the β particles.

Heavy Charged Particles

As explained in [21], heavy charged particles mainly lose energy and are slowed down by Coulomb scattering and interactions with atomic electrons. In fact, when

heavy particles pass through matter they first lose energy by interacting with the field of electrons around the nuclei present in the material in the form of inelastic interactions. The energy loss associated to this process is often called *electronic stopping power* indicating the average energy loss per unit length. It is also possible to define the *mass stopping power* indicating the average energy loss per unit areal mass such as $MeV/(g/cm^2)$. Given the high number of electromagnetic interactions in a normal density media, the slowing down of heavy charged particles is almost continuous through the material. Heavy charged particles follow straight-line paths as, due to their heavy mass, they are not easily deflected by the atomic electrons.
Once the heavy particles' energy isn't sufficient to excite an electron they then lose energy by a variety of processes as shown in Fig. 2.1 including nuclear collisions which are elastic. The nuclear stopping power associated to the energy loss in this case, is much smaller then the electronic stopping power, generally contributing for less than 0.1% of the total energy loss.
An approximation of the electronic stopping power can be obtained and expressed by the Bethe-Bloch formula as follows:

$$-\frac{dE}{dx} = Kz^2\frac{Z}{A}\frac{1}{\beta^2}\left[\frac{1}{2}ln\left(\frac{2m_ec^2\beta^2\gamma^2T_{max}}{I^2}\right) - \beta^2 - \frac{C}{Z} - \frac{\delta}{2}\right] \tag{2.1}$$

where T_{max} is the maximum energy transfer taking place in a single collision, I the mean excitation potential of the target material and Z and A the material's atomic number and mass respectively. Two corrections terms are usually taken into account: the shell effect given by $\frac{C}{Z}$ and the density correction δ. The energy term of the travelling particle is provided by:

$$\beta = \frac{v}{c} \quad and \quad \gamma = \frac{1}{\sqrt{1-\frac{v^2}{c^2}}} \tag{2.2}$$

where v is the relative speed of the travelling particle, c the speed of light and γ the Lorentz factor which can be used in the so-called *Lorentz transformation* to indicate the change in time, length and relativistic mass for a moving object. Fig. 2.2 from [22], shows the stopping power or mean energy loss rate in various materials as function of the projectile energy.

As explained in [22], except in hydrogen, particles travelling with the same ve-

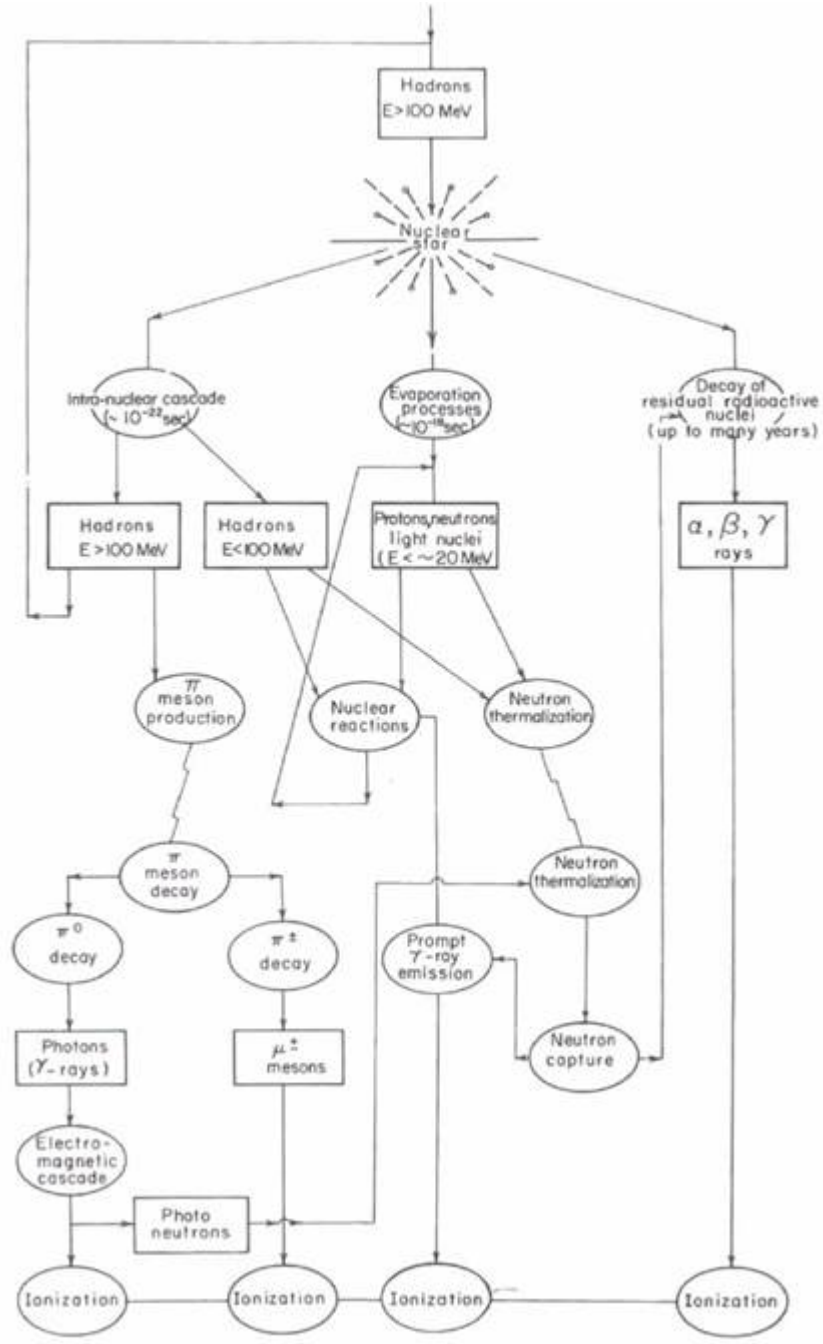

Figure 2.1: $E > 100$ MeV hadron processes cascade

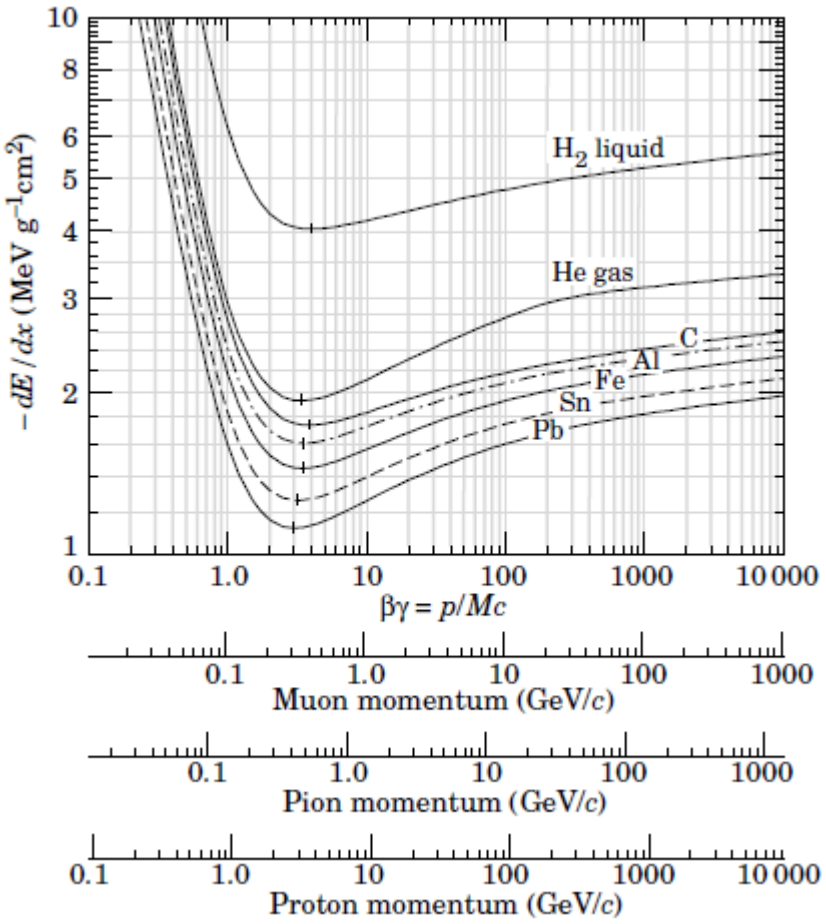

Figure 2.2: Mean energy loss rate in various materials [23]

locity have similar rates of energy loss in different materials, although there is a slow decrease in the rate with increasing Z. At higher energies, the qualitative difference in behavior between a gas such as He and other materials as shown in Figure 2.2 from [23], is due to the density correction term δ present in Equation 2.1. At lower energies, when particles slow down in the material, the energy loss rate increases following $1/\beta^2$ giving rise to what is known as Bragg peak. In other words, when particles are close to stopping their path in the material, a peak in the energy loss rate is observed as shown in Fig. 2.3. This feature of heavy particles such as protons or ions is nowadays commonly used in cancer therapy to maximize the dose deposition on the target tumor while avoiding to damage healthy tissues.

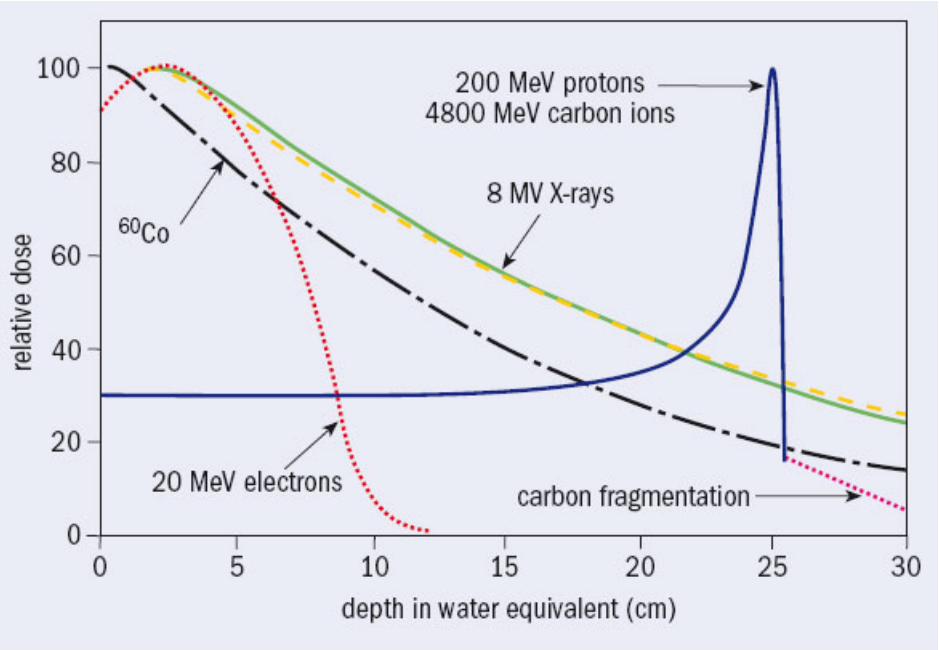

Figure 2.3: Depth dependence of the deposited dose for different radiation type, including the Bragg peak for protons and carbon ions

Light Charged Particles

In addition to energy loss mechanisms similar to the one just described for heavy particles, light charged particles may also interact with matter in the form of *Bremsstrahlung* which consists in the creation of X-rays from electron deceleration. Together with inelastic collisions, Bremsstrahlung is responsible for the main energy loss mechanism of electrons and positrons for low energies up to intermediate ones of several tens of MeV. Bremsstrahlung occurs because electrons may suffer from rapid changes in the direction and magnitude of their velocities as they get deflected in collisions with other electrons. The rapid changes in velocity give rise to strong accelerations which, given the charged nature of electrons, lead to electromagnetic energy being radiated.

2.1.2 Neutral Radiation - Indirectly Ionizing Particles

Uncharged radiation such as neutrons, *Gamma* or X-rays are classified as indirectly ionizing even though they are capable of causing the direct liberation of

charged particles.
Being uncharged, neutrons can travel appreciable distance in matter without interacting. Neutrons can interact with the atomic nucleus following several different mechanisms according to their energy, among these: elastic and inelastic scattering, neutron capture, neutron spallation, nuclear fission and more. More details about neutron interaction with matter can be found in [21] and [24] but are beyond the scope of this thesis.

Photons: Gamma rays and X-rays

Gamma rays (also known as γ-rays) and X-rays refer to electromagnetic radiation and both consist of carrier particles. Originally, the distinction between γ-rays and X-rays was based on their energies, gamma rays being more energetic. Nowadays, modern high-energy X-rays produced by linear accelerators may be as energetic as the gammas, hence the difference mostly resides in their origin: while gamma rays are emitted by a nucleus, by means of particles decays or annihilation events, X-rays are emitted by electrons (for example during Bremsstrahlung).
When photons impinge on matter, their energy is imparted in a two stage process. At first, the photon radiation transfers energy to the secondary charged particles, electrons, through various photon interactions and in the second stage, the charged particles themselves transfer energy to the material through atomic excitations and ionizations. The fundamental interactions which photons undergo are the photoelectric effect, the Compton scattering and pair production.

The photoelectric effect

The photoelectric effect dominates at low energies (< 100 keV) and consists in an interaction between a photon and an atom, in which the photon transfers all of its energy to an orbital electron. As a consequence, the electron, also called photoelectron, is ejected with kinetic energy equal to the incident photon energy less the binding energy (or ionization energy) needed to remove the electron, $E_e = E_\gamma - E_b$. All the photon energy is therefore absorbed into the material while the vacancy left by the ejected electron is filled by electrons from other shells accompanied by the emission of fluorescence and/or Auger electrons.

Compton scattering

The Compton scattering dominates the interactions at medium energies, from 100 keV to a few MeV. It is an inelastic scattering of a photon by an atomic electron of the outer atomic shells. The scattered photon is deflected from its original trajectory and has a lower energy, therefore, a longer wavelength according to the Planck relationship: $E = h\nu$ where h is the Planck constant and ν radiation's frequency. The wavelength shift increases with the scattering angle according to the Compton formula:

$$\Delta_\lambda = \lambda_f - \lambda_i = \frac{h}{m_e c}(1 - cos\theta) \tag{2.3}$$

where λ_f and λ_i are the wavelengths before and after collision respectively, h the Planck's constant, m_e the electron mass and c the speed of light.

Pair production

At higher energies, $E > 1.5$ MeV, the photon matter interactions are dominated by pair production which consist in the absorption of a photon and the creation of a positron-electron pair. Since the the energy of the photon E_γ is directly converted into the mass of the two newly created particles, the pair production is only possible if E_γ is at least twice the rest mass of the electron $m_e = 0.511$ MeV, hence $E_\gamma > 1.022$ MeV.

The probability for photoelectric absorption, Compton scattering and pair production are detailed in [21]. It is however worth putting emphasis on the fact that the energy of the γ-rays usually used in radiation testing, such as the ones emitted by a ^{60}Co source, is around 1 Mev. Given the low atomic number of material such as Silicon or Silica, the dominant interaction taking place when characterizing a photonic component at a ^{60}Co facility, is the Compton scattering as is depicted in Fig. 2.4 from [25] and in Fig. 2.5 from [26].

In particular, Fig. 2.5 shows the relative importance of the three main types of

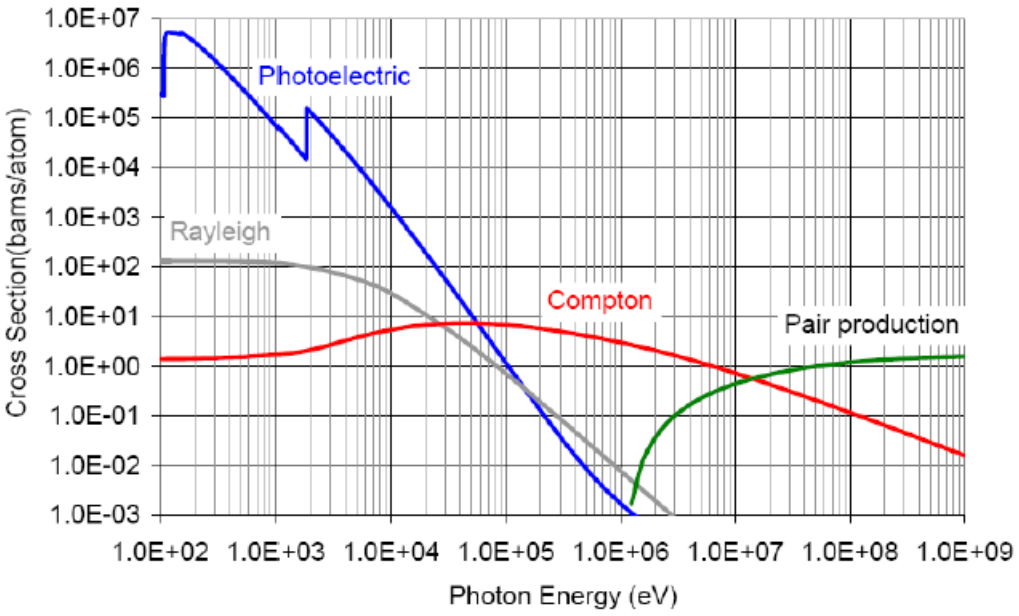

Figure 2.4: Cross sections for different photon-material interaction mechanisms as function of photon energy [25]

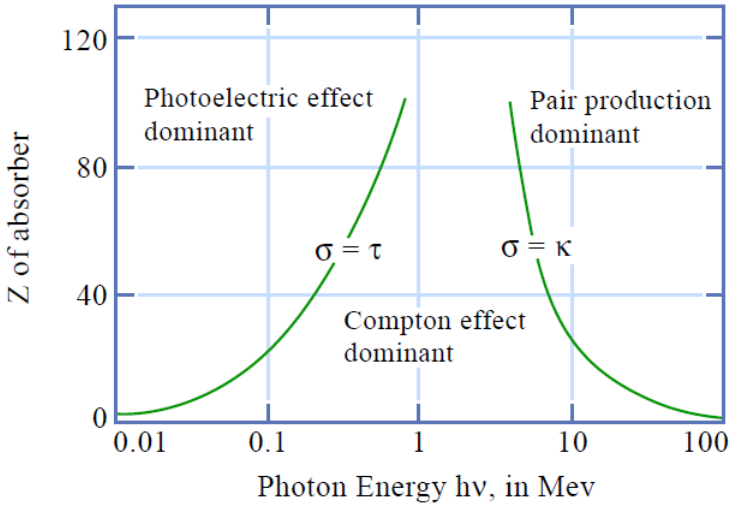

Figure 2.5: Relative importance of the three main types of γ-ray interactions [26]

γ-ray interactions where τ, σ and κ are the probabilities for photoelectric absorption, Compton scattering and pair production respectively.

2.1.3 Non-ionizing Energy Loss

Some particles able to lose energy in matter via ionization processes may also lose energy undergoing non-ionization mechanisms such as *atomic displacement*. This mechanism can occur either through the transfer of kinetic energy to atoms in the material or by conversion of radiation induced excitation into atom motion, that is radiolytically. When an atom is ejected from its normal position by an elastic collision, it is often referred to as *primary knock-on*. This, can then generate a cascade of atomic displacements before eventually reaching a rest situation. A displaced atom is referred to as an *interstitial* while the position it used to occupy is known as *vacancy*. The interstitial-vacancy pair is also known as the *Frenkel pair*.

As a consequence of atomic displacement, the material undergoes *displacement damage* which is a cumulative long-term damage in which lattice defects are created. Displacement damage effects are a function of the impinging neutrons' energy which is transferred to the nuclear recoils produced, this observation goes under the name of "NIEL hypothesis" [27]. Usually, displacement damage is expressed in terms of the damage that would be caused by a given flux of neutrons and by convention (for their use in reactors), we consider a 1 MeV flux of neutrons. The fluence of any other particle however, can be reduced to an equivalent 1 MeV neutron fluence producing the same amount of displacements.

It is worth remembering that the fluence Φ is defined as the number dN of particles incident on a sphere of cross-sectional area da as expressed here:

$$\Phi = \frac{dN}{da} \tag{2.4}$$

The use of a sphere allows to express the idea that the area da is perpendicular to the direction of each particle, so that all particles passing through this volume of space are included. The fluence is express in m^{-2} and can also be seen as the time integral of the incident flux of particles through da over the exposure duration [24].

To quantify the amount of radiation which an optical component or optical fiber

receives, in the next section the definitions of the kinetic energy released in matter (kerma) and the total ionizing dose (TID) will be introduced.

2.2 Quantification of radiation levels and radiation damage in materials

In the following section, based on [27], fundamental concepts allowing to quantify the amount of radiation received by components will be presented. In the case of ionizing energy loss we will introduce the concepts of *kerma*, of *ionizing dose* while for atomic displacements and their associated displacement damage, we will define the NIEL quantity.

2.2.1 Kerma and total ionizing dose

As explained in the previous section, the interaction of uncharged particles with matter occurs in two stages: first the incident particles transfer energy to charged particles in the material and then, that same energy is deposited in the material as the charged particles slow down. These two steps can be quantified by the kinetic energy released in matter (kerma) and the ionizing dose concepts respectively.

Kerma

The kinetic energy released per unit mass, *kerma*, is a nonstochastic quantity applicable to indirectly ionizing radiations such as photons and neutrons. It quantifies the amount of energy transferred from indirectly ionizing radiation to directly ionizing radiation without taking into account the step after this transfer. The kerma can therefore be defined as the energy transferred from the indirectly ionizing radiation to charged particles (electrons) in the medium, dE_T per unit mass dm:

$$kerma = \frac{dE_T}{dm} \tag{2.5}$$

where E_T is the sum of the initial kinetic energies of all charged ionizing particles created by uncharged ionizing particles in the material. The unit of kerma is joule

per kilogram (J/kg). The name for the unit of kerma is the Gray (Gy), where 1 Gy = 1 J/kg. Kerma must be defined with respect to the specific material in which the interaction occurs, for optical fibers for example, we talk about SiO_2 kerma.

Total Ionizing Dose (TID)

Charged particles which received energy from the incident radiation, transfer some of their kinetic energy to the medium resulting in *absorbed dose* or ionizing dose and also lose some of their energy in the form of radiative losses (bremsstrahlung, annihilation in flight). Absorbed dose is a non-stochastic quantity applicable to both indirectly and directly ionizing radiations. The absorbed dose or total ionizing dose D is defined as the energy absorbed per unit mass in a material:

$$D = \frac{dE}{dm} \tag{2.6}$$

where dE is the mean energy imparted by ionizing radiation to matter of mass dm. Like kerma, the total ionizing dose D is also expressed in Gray although an older unit, the "rad", is still in restricted use and 1 $rad = 10^{-2}Gy$. The energy dE is the sum of all the energy entering the volume of interest minus all the energy leaving the volume, taking into account any mass-energy conversion within the volume. When charged particle equilibrium exists in the material at the point of interest and when Brehmsstrahlung and the kinetic energy of the particles produced by nuclear reactions are negligible, the kerma equals the dose D at that point.

2.2.2 NIEL

The Non-Ionizing Energy Loss, NIEL, allows to quantify displacement damage by representing the energy loss to non-ionizing events per unit length and is expressed in $keV \cdot cm^2/g$. The displacement-kerma is then calculated by multiplying the NIEL value by the incident fluence and by the mass in grams of the irradiated material volume as showed in the following equation:

$$kerma[keV] = NIEL\left[keV \cdot \frac{cm^2}{g}\right] \cdot \phi\left[\frac{1}{cm^2}\right] \cdot m[g] \tag{2.7}$$

A quantity equivalent to the NIEL is the displacement damage cross section D to which damage effects by energetic particles in the bulk of any material are proportional. D is normally quantified in $MeV \cdot mb$ and according to an American Society for Testing and Materials (ASTM) standard, the displacement damage cross section for 1 MeV neutrons is set as a normalizing value: $D_n(1MeV) = 95MeV \cdot mb$. The displacement damage in Silicon for neutrons, protons, pions and electrons as function of energy is the depicted in Fig. 2.6.

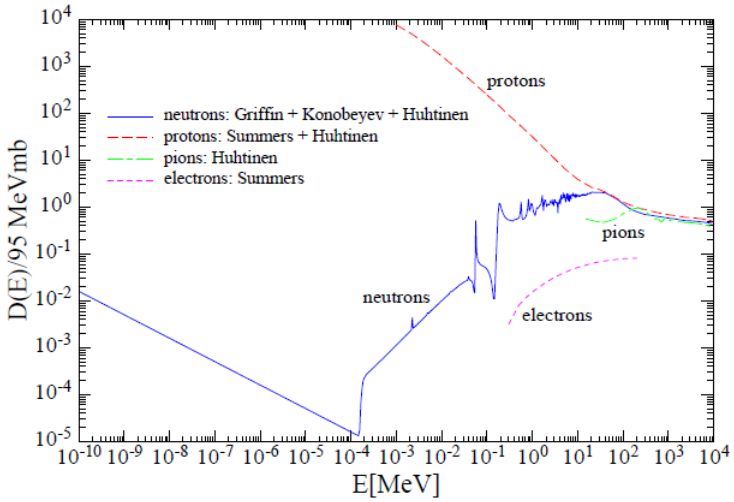

Figure 2.6: Displacement damage in Silicon for neutrons, protons, pions and electrons [28]

Finally, the damage efficiency of any particle with a given kinetic energy E can be described by a hardness factor k as:

$$k = \frac{D_{d,particle}}{D_{d,1MeV\ neutrons}} \tag{2.8}$$

2.3 Radiation detectors and dose measurements

As explained in the previous section, the interaction between radiation and matter is characterized by a number of effects which can be used to detect radiation, measure particle flux density or intensity as well as dose and radiation spectra. Such information is very useful when monitoring and assessing the lifetime of electronic instrumentation present at accelerators. Detector instruments can be in the form of nuclear instrumentation, portable survey instruments and area

monitors or as personnel monitoring devices. In the following, the different general types of radiation detectors will be briefly presented.

2.3.1 Gas filled detectors

Gas filled detectors operate by exploiting the ionization produced by incident radiation as it passes through a gas. Such a counter consists of two electrodes to which a certain electrical potential is applied. The space between the electrodes is filled with a gas contained in cylindrical chamber. Among mostly used gases one can find helium, neon and argon-methane mixtures. When ionizing radiation passes through the chamber, electron-ion pairs are generated which then move under the influence of the electric field. This induces a current on the electrodes which may be measured and related to the incident radiation level. According to the voltage region depicted in Fig. 2.7 in which a gas filled detector operates, the detector is defined and named differently. [24].

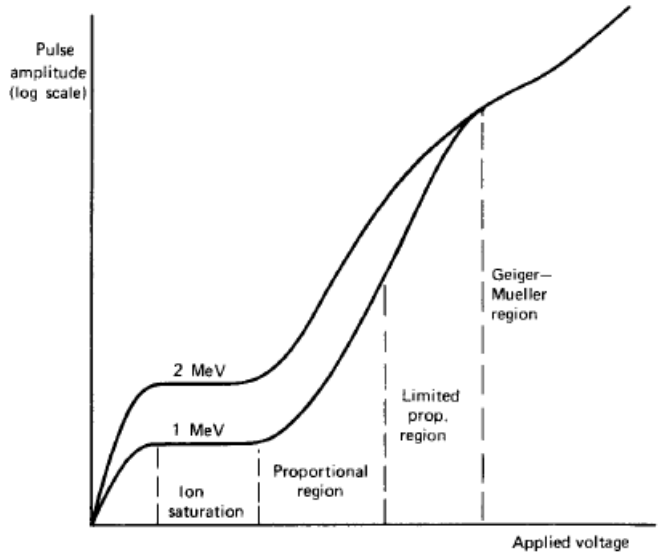

Figure 2.7: Operation regions of gas filled detectors [24]

Ionization chambers for example, work in the proportional region. In this region, since the output signal which is proportional to the particle energy dissipated in the detector is not very large, only strongly ionizing particles such as protons and heavy ions are detected.
Depending on the detector, the charge produced by the radiation may also be

transformed into a pulse in which case particles are counted individually and can be discriminated by applying electronic filters on the pulses' height associated to a certain radiation type. This is the case of *proportional gas filled detectors* which allow the discrimination of α, β and γ radiation as well as the measurement of the particle's energy. Such detectors are used as portable survey monitors or as personnel contamination monitors.
A third type of gas filled radiation detectors are *Geiger-Müller counters*. These operate in the high voltage region and can be used for any kind of radiation. The generated signal is generally independent of the particle energy and its type and therefore such counters only provide information about the number of particles. By using a combination of different Geiger-Müller counters or by using different window types and thickness it is possible to filter incident radiation and filter α and β [24].

2.3.2 Scintillation detectors

Scintillation detectors detect radiation by induction of luminescence. They are made of materials which can be solids (such as Anthracene crystals or Sodium iodide crystals), liquids, or gases that produce sparks or scintillations of visible light when ionizing radiation passes through them. The detection of the generated light occurs by means of a photocathode which is a light-sensitive material that absorbs photons and emits photoelectrons. As the amount of light produced in the scintillator is very small, it must therefore be amplified before it can be recorded as a pulse or in any other way. The amplification of the scintillator's light is achieved with a photomultiplier tube which allows for amplifications or gain of 10^6 and outputs the amplified signal.

2.3.3 Semiconductor detectors

Semiconductor detectors are solid state devices which essentially operate as ionization chambers but it is filled with a solid semiconductor material instead of a gas. In semiconductor detectors, the electric field is established by a more complicated process with respect to gas filled detectors, a process that depends on the properties of n- and p- type semiconductors. The energy transfer from the

incident radiation to the semiconductor produces a freed electron and a hole (vacancy) moving to the anode and cathode respectively. The sensitive region of the counter is only a few millimeters and the speed of electrons and holes is such that the charge carriers can cross the sensitive region and be collected in times of the order of 10^{-7}s. As a result semiconductor detectors have a fast response time. In addition, since a smaller amount of energy is required to produce electron-hole pair in a semiconductor than an ion pair in a gas, semiconductor detectors exhibit less statistical fluctuations for any given radiation energy. Other advantages of semiconductor detectors are the high energy resolution, the linear response over a wide range of energies and the ability to operate in vacuum. On the other hand these detectors are very sensitive to heat and often require cooling.

2.3.4 The LHC Radiation Monitoring System - RadMon

The Radiation Monitoring System, RadMon, is designed to measure the radiation effects on the electronics in the LHC tunnel and its adjacent shielded areas in order to monitor the radiation levels, anticipate possible device degradation and identify instantaneous failures of the electronic equipments, correlated to their typical Mean Time Between Failure (MTBF) as caused by radiation [9]. For these purposes, the RadMon provides the measurement of the Total Ionizing Dose (TID) in Silicon dioxide by means of Radiation-sensing Field-Effect Transistors (RadFETs), of the Displacement Damage (DD) in Silicon by means of p-i-n diodes, and of the High Energy Hadrons (HEH) and thermal neutrons fluence by counting Single Events Upsets (SEU) in SRAM memory [9].
In particular, for what concerns the dose measurements they are based on Radiation-Sensing Field-Effect Transistors (RadFETs) which are p-channel MosFETs that are optimized for monitoring the TID on Electronic Devices. The idea is that the p-channel MosFET responds to the field produced when space-charge is trapped in the oxide region. An electrical measurement (shift of threshold voltage) then gives a relative value of dose in rad or Gy(Si).

As the other detectors presented in this section, a RadMon measures the radiation levels at its own position. Its sensor window has a dimension of $5 \cdot 10\, cm^2$, the RadMon can be therefore considered as a point sensor when related to the

length of the LHC. For this reason about 500 RadMons are used in the LHC tunnel zone (about 27 km) to assure a good coverage of all the areas where sensitive electronics are installed.

To conclude, it is worth to notice that conventional detectors including LHC's actual radiation monitoring system, are discrete sensors which can't provide a monitoring of radiation levels in every point along the accelerator. This is an important limitation as some key points where electronics is installed, remain uncovered. For this reason, the implementation of a distributed sensor providing a much more dense spatial information would be highly beneficial. In this respect a distributed optical fiber based radiation sensors could represent the ideal solution as will showed throughout this Thesis.

2.4 Radiation environment at CERN's accelerator complex

In this section an overview of CERN's accelerator complex is given together with the radiation environment one can expect in the Large Hadron Collider (LHC) tunnels. CERN's accelerator complex is a succession of machines that accelerate particles to increasingly higher energies. Each of the machine boosts the energy of a beam of particles, before injecting the beam into the next machine in the sequence. In the LHC, the largest and final accelerator in the chain, particle beams have been accelerated up to the record energy of 4 TeV during its RUN1 (2009-2013) and up to a new record energy of almost 7 TeV during RUN2 which started this year (2015) after the numerous upgrades and renovation works carried out during the Long Shutdown (LS1). Most of the other accelerators in the chain have their own experimental halls where beams are used for experiments at lower energies [29]. For example, from the Positron Synchrotron (PS), a 24 GeV/c proton beam is extracted and sent to the so-called "Cern High energy AcceleRator Mixed field facility" (CHARM) located in the East Hall. The CHARM facility, used for irradiation tests presented in this work, will be further described in Chapter 7. Figure 2.8 shows a schematic map of CERN accelerator complex.

The source of protons which will end up in the LHC, is a bottle of hydrogen

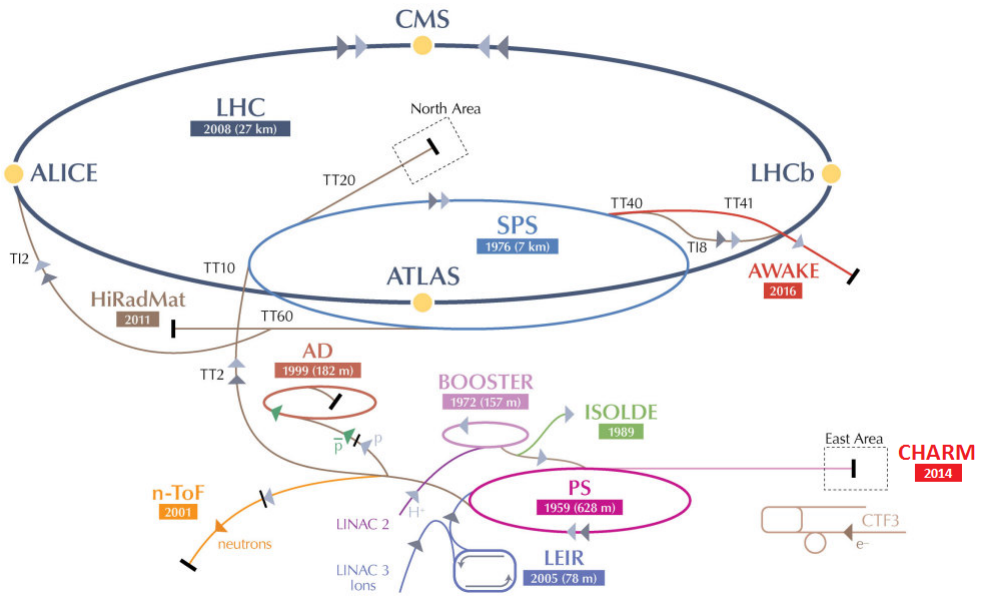

Figure 2.8: CERN Accelerator Complex [29]

gas. An electric field is used to strip hydrogen atoms of their electrons to yield protons. The first acceleration of the protons to the energy of 50 MeV takes place in Linac 2 after which the beam is injected into the Proton Synchrotron Booster (PSB), which accelerates the protons to 1.4 GeV. After the PSB, the protons are injected into the the Proton Synchrotron (PS), which pushes the beam up to 25 GeV. Protons are then sent to the Super Proton Synchrotron (SPS) where they are accelerated to 450 GeV. The protons are finally transferred to two beam pipes of the LHC where the beams circulates in clockwise and anticlockwise directions respectively. After 20 minutes the protons reach their maximum energy of 4 TeV (RUN1) and 7 TeV (RUN2) and after some minutes, the two beams are brought into collision inside the four main detectors: ALICE, ATLAS, CMS and LHCb where the total energy at the collision point will be finally equal to 14 TeV (during RUN2) and where 13 TeV collisions have already been achieved in June 2015[29]. The main radiation sources found at accelerators are: direct losses in collimators and absorber like objects, particle debris from beam collisions in the four main experiments and interaction of the beam with the residual gas inside the beam pipe. The variety of source terms result in a unique radiation field of mixed particle types and energies, as shown in Fig. 2.9, for a typical LHC tunnel area. Inside the accelerator tunnel protons and pions contribute to the largest fraction

of the high energy hadron fluence [9].

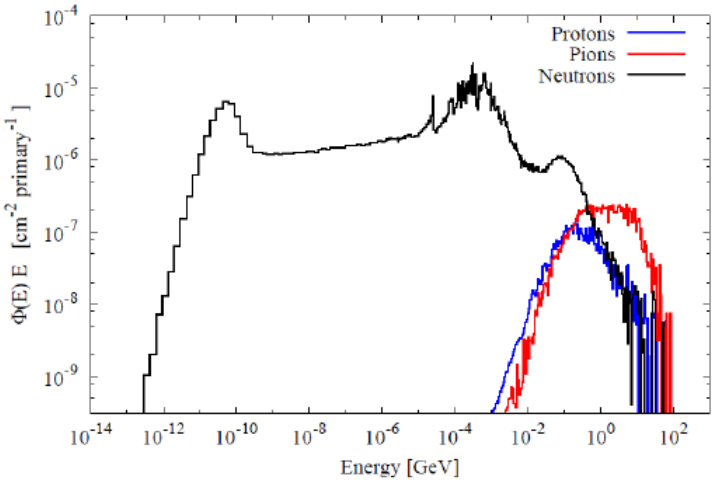

Figure 2.9: Particle energy spectra representative for tunnel areas in the LHC [9]

2.5 Monte Carlo simulation package: FLUKA

FLUKA is a Monte Carlo code able to simulate transport and interaction of electromagnetic and hadronic particles in any target material over a wide energy range. It is a multi-purpose, multi-particle code that can be applied in many different fields spanning from proton and electron accelerator shielding to target design, calorimetry, activation, dosimetry, detector design, Accelerator Driven Systems, cosmic rays, neutrino physics, radiotherapy and more.
The interaction and propagation in matter of about 60 different particles can be simulated by FLUKA with high accuracy, including photons and electrons from 1 keV to thousands of TeV, neutrinos, muons of any energy, hadrons of energies up to 20 TeV (up to 10 PeV by linking FLUKA with the DPMJET code) and all the corresponding antiparticles, neutrons down to thermal energies and heavy ions. The program can also transport polarised photons and optical photons. As shown in Fig. 2.10, FLUKA can handle very complex geometries, using an improved version of the well-known Combinatorial Geometry (CG) package [30].

In Chapter 8 of this thesis, experimental results of distributed optical fiber radiation measurements carried out in the CHARM facility will be compared with FLUKA simulations.

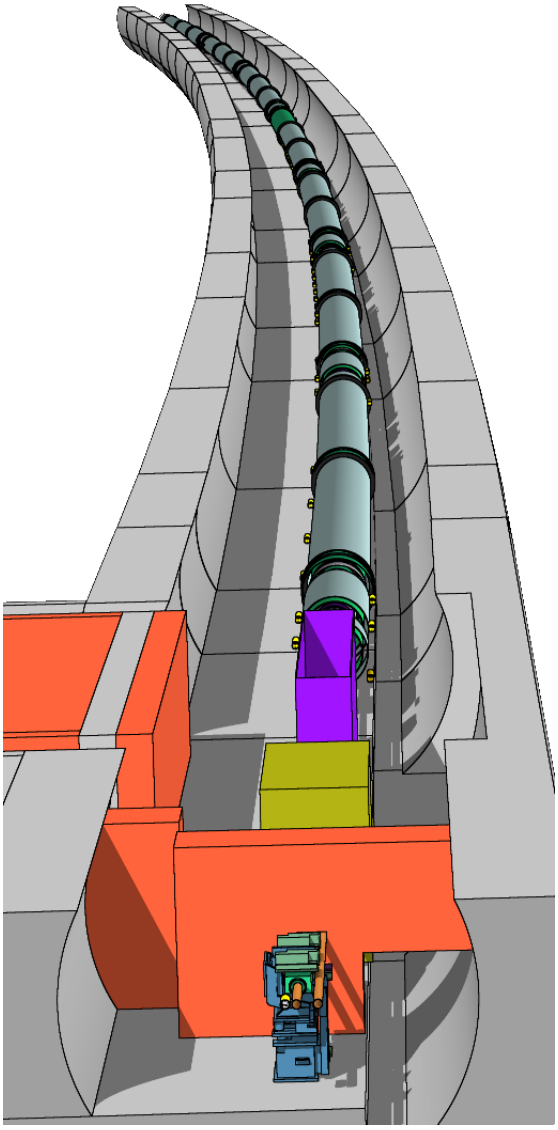

Figure 2.10: FLUKA's geometry editor: 3D topview of LHC IR7 Dispersion Suppressor

3 Radiation effects on Silica-based optical fibers

Thanks to its low absorption and scattering in the near-infrared portion of the spectrum, its mechanical strength and possibility of effective fusion splicing, silica (SiO_2) is the preferred material for the manufacture of optical fibers for telecom applications. In order to allow total internal reflection of light inside the fibre, silica must be doped with other elements to obtain a higher refractive index in the core region with respect to the in the cladding. Depending on the composition of the fiber, its response to radiation can be drastically different and can therefore be used in different harsh environments with different targeted application.
The purpose of this chapter is to describe the characteristics of silica-based fibres and how the fiber's structure and composition but also the influence of the characteristics of the radiative environment and the ones of the targeted application can affect the response of the fiber to radiation.

3.1 Silica based glasses properties

In order to understand the radiation effects on silica-based fibres it is necessary to study the changes that occur in the structure of pure and doped amorphous silica ($a - SiO_2$) at different scales. The ($a - SiO_2$) building unit is the SiO_4 tetrahedron, like in the quartz crystalline structure. The microscopic structure of ideal $a - SiO_2$ is commonly described through the Continuous Random Network (CRN) theory, in which the units have a central silicon (Si) atom which is bonded to four oxygen (O) atoms, with each O atom being a bridge between two Si atoms, forming O-Si-O angles (α) that are statistically distributed between 120° and 180°

as shown in Fig. 3.1[31].

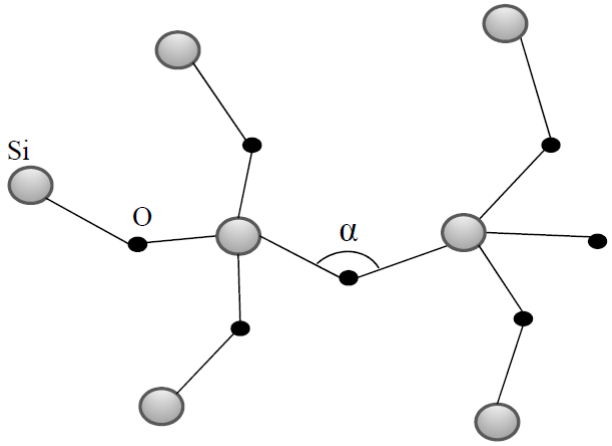

Figure 3.1: Structure of amorphous silica, showing the silicon (Si) atoms (in grey) and the binding oxygen (O) atoms (in back)

The amorphous quality of $a-SiO_2$ is given by the randomness of the structure, due to the variations in the angle, the lack of periodicity, deviation from the network topology and ring statistics [14]. The similarity between the structural units is responsible for a crystalline-like short range order, which results in a wide energy-gap between the valence and conduction bands, giving to amorphous silica properties such as transparency in the visible band and electrical insulation, which makes it eligible for many applications [32]. In bulk and optical fibers however, the nature of glass is more complex due to the presence of intrinsic or extrinsic point defects that are induced during the glass elaboration or under specific treatments [33]. Fig. 3.2 shows a comparison between the ideal pure-silica glass structure and defective one.

Defect structures are related to under- or over-coordinated atoms, substitutional or interstitial impurities such as Cl or H as depicted in Fig. 3.2(b), or bonds between similar atoms. These defects are associated with absorption bands within the silica bandgap that decrease the glass or fiber transparency. They can either be created during the manufacturing process, by conversion of pre-existing centers under irradiation or directly from "perfect" sites by radiations.
Optical fibers present a wide range of radiation sensitivities depending on the dopants used to design their refractive-index profiles. Among the different existing dopants, the most used are Germanium (Ge), Phosphorus (P) and Nitrogen

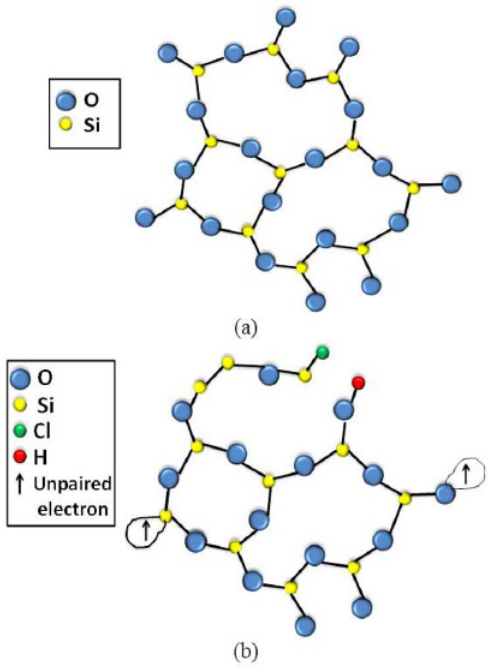

Figure 3.2: Comparison between (a) ideal pure-silica glass structure and (b) defective pure-silica glass structure [14]

(N) which increase the glass refractive index, and Fluorine (F) or Boron (B) which decrease it.

3.2 Radiation effects at the microscopic and macroscopic levels

3.2.1 Radiation-damage processes

A the microscopic scale, in glass, there are two main radiation-matter interactions that result in defects: direct atomic displacements and radiolytic processes. Direct atomic displacements (also known as knock-on) already introduced in Chapter 2 of this Thesis, can occur in silica when incoming particles interact with the material's atoms transferring enough energy to the glass matrix and cause displacements or distortions. The amount of this energy is called displacement energy T_d, and for oxygen and silica it has been found to be about $T_d^O \approx 10eV$ and $T_d^{Si} \approx 18eV$ respec-

tively [34][35]. It is worth briefly remembering that among the types of particles that cause knock-on displacements there are: fast neutrons, thermal neutrons, energetic ions and energetic electrons (≥ 70 keV for O and ≥ 200 keV for Si).
On the other hand, in ionization processes and associated radiolytic processes, electrons from the valence band ca be transferred to the conduction band with a certain kinetic energy, which depends on the energy transferred by the incoming particle. As a consequence a hole is generated in the valence band. The created electron-hole pairs can recombine either radiatively (luminescence) or non-radiatively in which case the energy is dissipated through the creation of phonons or kinetic energy that generates point defects. Mobile charges can also be trapped on pre-existing or radiation-induced sites [14]. Radiolityc processes are predominant in the case of electron and gamma irradiation [32]. Fig. 3.3 summarizes the different radiation damage processes in glass.

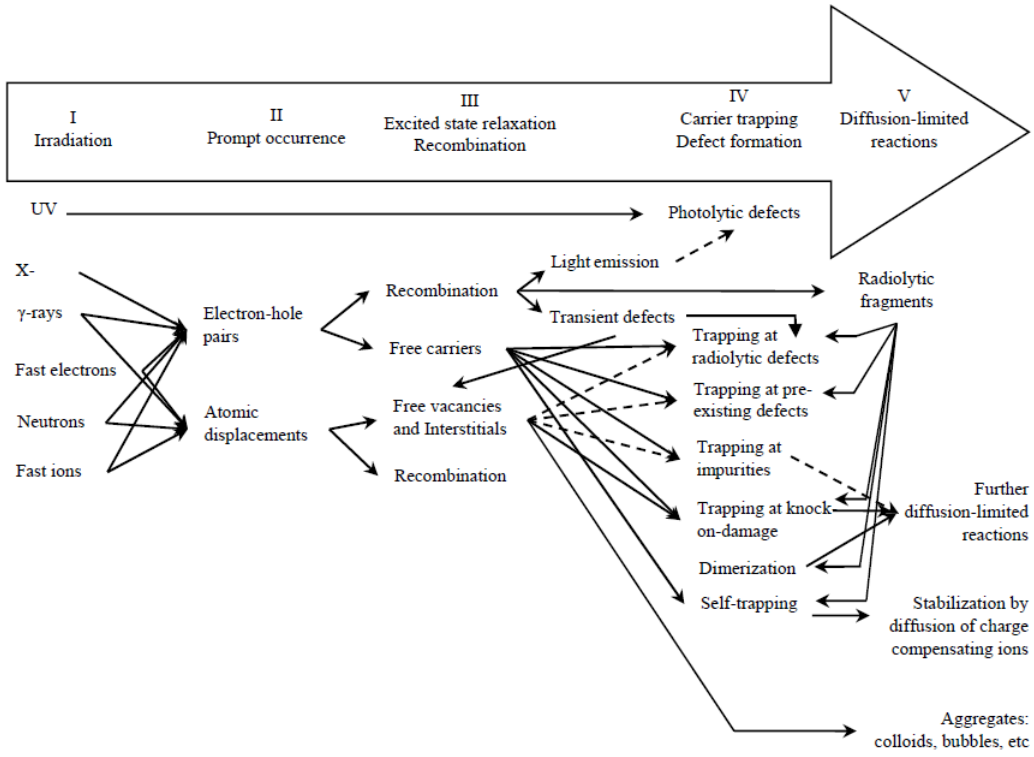

Figure 3.3: Diagram of the most relevant radiation-damage effects in glass material [27]

3.2.2 Radiation induced macroscopic changes

Ionizing radiation degrades all the properties of an optical fiber. In silica-based glasses, three macroscopic effects can be observed under irradiation: Radiation Induced Attenuation (RIA), Radiation Induced Emission (RIE) and change in the refractive index. In the following, all three effects will be briefly summarized.

Radiation Induced Attenuation (RIA)

RIA corresponds to an increase in the glass linear attenuation through an increase of the linear absorption due to radiation-induced defects. It is a wavelength- and time-dependent effect [14]. In particular, the absorption due to radiation-induced point defects is higher in the UV and part of the visible spectrum for pure silica optical fibers, with tails that extend to the infrared. Fig. 3.4 shows the radiation-induced spectra for pure silica and doped silica fibers. For pure silica fibers it can be observed that the RIA decreases for longer wavelengths, except for the band at 0.63 μm in high hydroxyl groups (OH) silica fibres. The tendency of the RIA curve for different Ge-doped fibres varies according to the type of co-dopant. For the Ge(BTL), from the Bell Telephone Laboratories, the decrease with respect to wavelength is monotonic, while the one co-doped with Boron (B) presents an increase at longer wavelengths.
P-doped fibres present an higher RIA with respect to fiber doped with other dopants being therefore the most sensitive to radiation. An induced band at around 1.6 μm can be observed and its intensity depends on the P concentration in the core of the fibre.
Fig. 3.4 indicates that the selection of the dopant allows to tune the sensitivity to radiation and that for a given dopant the wavelength may allow to fine tune this sensitivity. More details about the influence of the composition on a fiber's response and about other RIA dependencies will follow later in this Chapter.

Radiation Induced Emission (RIE)

RIE corresponds to light emission within the samples under irradiation. The luminescence can be due to pre-existing or radiation-induced colour centres originated by interaction of the incoming particles with the material, known as radiation

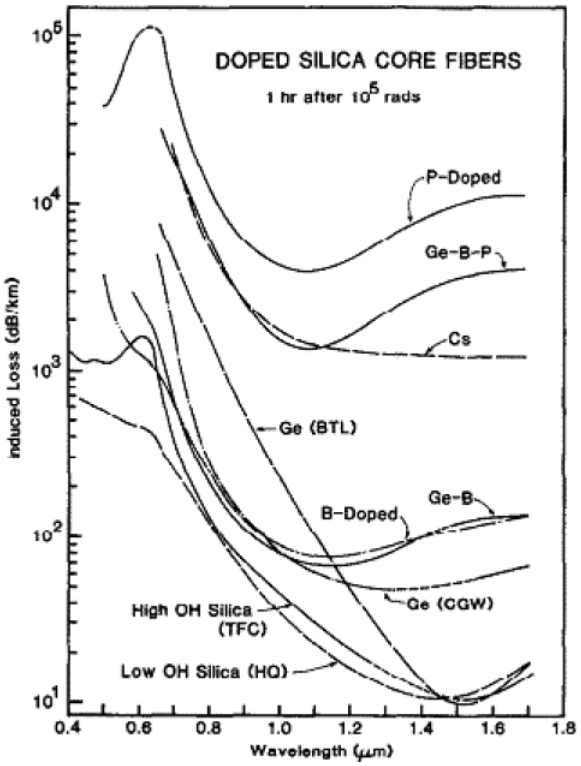

Figure 3.4: Radiation-induced attenuation spectra of pure silica and doped silica core fibres measured one hour after an irradiation of 10^5 rad [36]

induced luminescence (RIL), or by Cerenkov emission [14]. Cerenkov light is generated when the incoming particles penetrate transparent materials with velocities higher than the speed of light in the medium, and its intensity is proportional to the radiation dose rate. In optical fibres a fraction of this light is transmitted in the direction of the fibre axis, allowing to monitor radiation [37].

Refractive Index change (RIC)

A change in the refractive index can arise from density changes or from the RIA. The Lorentz-Lorenz formula describes the RIC relation to a density change while the relationship to the induced absorption effect is shown with the Kramers-Krönig relations [14].
Compaction or swelling lead to glass density modifications and depend on the silica type. This was first observed for bulk silica irradiated with fast neutrons [38]. Neutron irradiation actually transforms both silica amorphous and crystal phases

into a new common topological structure referred to as the metamict phase [35]. The changes in refractive index affect the optical properties of the fibers creating additional guiding losses when a fiber is exposed to very high doses [14].

It is worth underlining that in the radiation environment which we target, we will be concerned by radiation levels of a few tens of Gy up to 100 kGy (annual) which are corresponding to a fluence of about $10^{10} - 10^{14}\ cm^{-2}$ of 1 MeV equivalent neutrons. We will be thus mostly dominated by the TID effects and as a consequence, among the three macroscopic effects above-described, RIA will be the main limiting factor for optical fiber to be used in our radiative environments. The influences of different parameters on the RIA will be discussed in the next sections.

3.3 Influence of the fiber structure and composition on its radiation response

3.3.1 Point defects in optical fibers

Point defects, also known as colour centres, are local distortions in the physical structure of the glass caused by the rupture of bonds and presence of impurity atoms, among other factors [32]. The presence of these defects in optical fibers, cause new energy levels to emerge inside the band gap of the dielectric material, causing an increase in the absorption of the light propagating and degrading the fibre. Point defects and the characteristics that make the fiber prone to their appearance, are originated during the manufacturing process. Steps such as rapid cooling from the melting temperature of the preform, deposition, drawing techniques, and impurities in the environment during the process might introduce defects [32]. In addition, the exposure of the fiber to different conditions after fabrication, like ionizing radiation from sources like high energy hadrons, and electrons can produce point defects [39].
Point defects can be commonly classified as intrinsic, when they are due to variations in the disposition of oxygen and silicon atoms in the silica matrix, and extrinsic, when they are due to the presence of impurities, such as H, Ge, P and

Cl [32][39]. Another possible classification is based on the electronic configuration of the defects: the ones with unpaired electrons are defined as paramagnetic defects, and the rest as diamagnetic defects.

Intrinsic point defects

If a deviation in the structure described by the CNR model is located in a region which dimensions can be compared to the interatomic distance, it is considered to be an intrinsic point defect. Such defects can also be classified as Oxygen deficient centres (ODC) and Oxygen associated hole centres. Examples of ODCs are the neutral oxygen vacancy: $O \equiv Si - Si \equiv O$, the tricoordinated silicon: $O \equiv Si\bullet$, also called E' centre, and the twofold coordinated silicon: $O = Si \bullet\bullet$, while among the Oxygen associated hole centres we find the neutral peroxy bridge $O \equiv Si - O - O - Si \equiv O$ and the non-bridging oxygen hole centre (NBOHC): $O \equiv Si - O\bullet$. To be noted that in the utilized representation O indicated the Oxygen atoms linked to the Silicon atoms. The symbols, −,= and ≡ indicate if the atoms have one, two or three bonds between them respectively. Finally, the symbols • and •• represent one and two non-bonded electrons. Fig. 3.5 illustrates the structure of these defects. Among the ODCs the most studied are the E' centres. The formation of this type of defect is influenced by the presence of hydroxyl radicals (OH) in the glass and by the irradiation energy. For the Oxygen associated hole centres the most studied are the NBOHC, which for bulk silica are usually created by exposure to radiation (gamma, UV) [40].

Extrinsic point defects

During the manufacturing process of optical fibers, impurities are introduced in the silica matrix, either intentionally in the form of dopants, or unintentionally due to the difficulty of avoiding their presence during fabrication. As mentioned earlier, dopants are widely used to modify the index profile of optical fibres in the core and cladding. Among the most used dopants, germanium and phosphorus have been widely studied in relation to the formation of extrinsic point defects. The fiber co-doping with other dopants like nitrogen (N) or aluminum (Al) however, has also been studied to understand the response to radiation of such fibers [41].

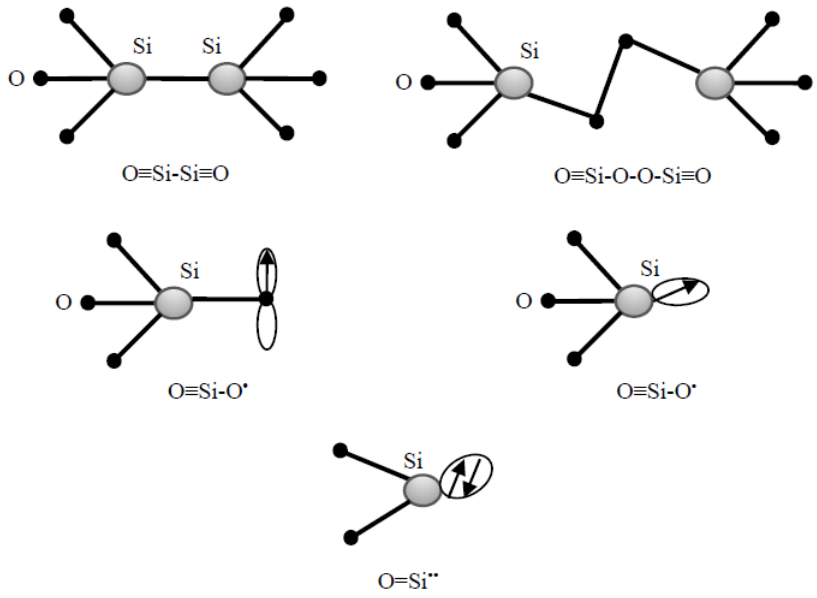

Figure 3.5: Representation of different point defects. The arrows indicate the electron spins and the ellipsoids the orbit [40]

3.3.2 Pure-Silica Core fibers (PSC)

Quite often, SM and MM Pure Silica Core fibers are designed having a fluorine doped cladding. Such fibers are characterized by low RIA levels from the UV to the IR part of the spectrum even at doses exceeding 1 MGy. The low induced attenuation in such fibers, often implies RIE, mainly Cerenkov and can be easily observed [42]. Fig. 3.6 shows the absorption bands associated with different Si-related point defect structures. These bands need to be taken into account to understand the behavior of fibers under irradiation. Most of the studied point defects absorb in the UV and visible part of the spectrum. Up to now, only one possible absorption band related to the Self-Trapped Holes (STHs) has been pointed out in the IR (not shown in Fig. 3.6) [43].

The concentrations of these different point defects depend on various parameters such as the glass stoichiometry or the hydroxyl groups (OH) and Cl impurities contents, their amounts being correlated. In particular, the amounts of Cl impurity strongly depend on the deposition technique used to elaborate the preforms. PSC are generally classified as follows:

- high-OH/low-Cl fibers called "wet" fibers,

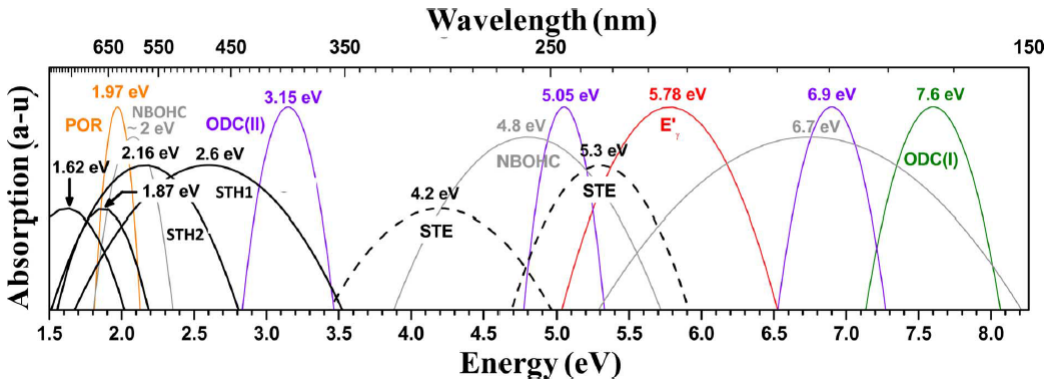

Figure 3.6: Absorption bands associated with different Si-related point defect structures[14]

- low-OH/Cl fibers called "dry" fibers,
- low-OH/low-Cl fibers,

with the last type being less common commercially. In high radiation environments where the doses are greater than 1 MGy, decreasing the Cl concentration is an efficient way to reduce the RIA in the UV and visible part of the spectrum [14]. The so-called "dry" fibers therefore exhibit higher RIA levels with respect to the "wet" and low-OH/low-Cl ones.

3.3.3 Germanium doped (Ge-doped)

Given most of the COTS Telecom optical fiber are germanosilicate ones, there has been a strong interest in studying their response to radiation for a multitude of applications ranging from radiation-tolerant telecommunication links [44][45] to space applications [46]. For most applications operating in the near-IR and IR ($> 1\mu m$), Ge-doped fibers can be used because the RIA levels remain acceptable. It must however be noted that very high radiation-induced losses have been observed in the UV and that the RIA in the visible domain is significantly higher than in PSC fibers.

Ge and Si are isoelectronic elements having therefore the same number of electrons. As a consequence, Ge-related point defects have a similar structure as those related to Si, but replacing Si with Ge atoms. In Ge-doped fibres, Ge-related defects are dominant over Si-related defects because they are generated in a more efficient

way. Fig. 3.7 shows the different absorption bands for different Ge-related point defects.

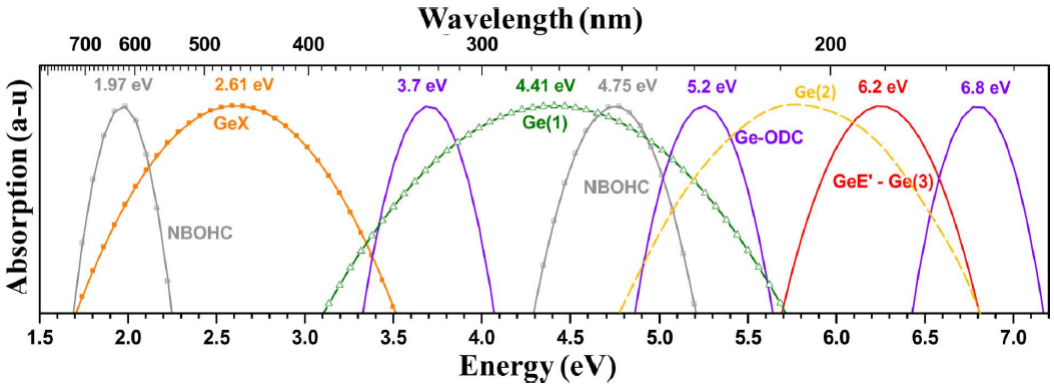

Figure 3.7: Absorption bands associated with different Ge-related point defect structures[14]

In Ge-doped fibers, the RIA has been found to monotonously increase with dose (D) before reaching a saturation level. Such dose dependency can be modeled by a power law $RIA = C \cdot D^f$ with an exponent $f < 1$ and where C corresponds to the defect growth.

3.3.4 Phosphorus doped (P-doped)

Phosphorus is widely used as co-dopant in silica fibers in the form of P_2O_5, allowing to improve the refractive index profile of the fiber [47] and the internal glass structure [48]. Phosphorus is also used as co-dopant with rare earths, such as Yb^{3+} and Er^{3+}, in optical fiber amplifiers to optimize signal amplification in the 1550 nm window, and as main dopant to optimize Raman fiber lasers [14].
The presence of phosphorus induces the generation of several structures of point defects under irradiation. These defects have absorption bands in the visible and infrared part of the spectrum [49], as show in Fig. 3.8. Most of these centers are stable at room temperature, which explains the high radiation sensitivities of phosphosilicate glasses to continuous radiations. The stability and optical properties of these defects lead to a linear dose dependence of the RIA at several wavelengths and at low to moderate dose as well as an independence of these induced losses to dose rate or temperature [16].

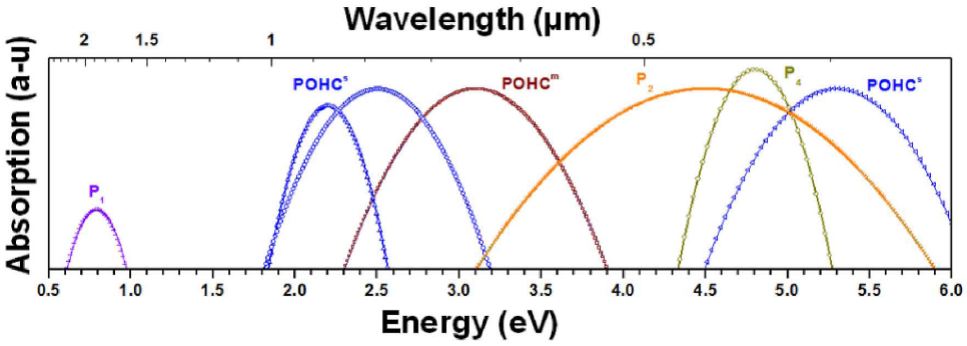

Figure 3.8: Absorption bands associated with different P-related point defect structures[14]

These very interesting and quite unique properties of P-doped fibers make them possible candidates for the development of radiation detectors or dosimeters for a large variety of applications [18][50]. It is in fact based on the above-mentioned reasons that the fibers selected for the experiments and measurements presented in this Thesis are all P-co-doped.

3.3.5 Aluminum doped (Al-doped)

Radiation-induced absorption in Al-doped fibers has also been investigated. In [51], two Al-doped fibres from two different manufacturers have demonstrated similar results showing a high gamma-radiation sensitivity up to a dose of 10 kGy after which the strong saturation took place. Beyond the dose of about 40 kGy further irradiation almost did not alter the attenuation. For dosimetry application up to 10 kGy those fibers could be considered as potential candidates [51].

3.3.6 SMF vs MMF

Nowadays, in many fibers it is often the core to be doped, whereas the cladding is made of pure silica. In the case of MMF most of the propagating power is concentrated mainly in the core, therefore the cladding does not influence RIA measurements significantly. In particular, it is to be expected that an increase in the dopant concentration, for example phosphorus, would lead to a respective increase in the observed RIA. On the other hand, especially in NIR, the situation is different in SMF where a significant fraction of the propagating power is extended

into the cladding. As consequence the radiation sensitivity consequently the RIA are usually significantly less in comparison to those of the core. In the third telecommunication window the in-cladding fraction of the power can be up to 50 %. The measured RIA in SMF fibres in NIR is therefore a summed effect of two different glasses of the core and of the cladding. In the case of optical fiber radiation sensing, it is therefore advisable to select MM as sensing fiber.

3.4 Radiative environment characteristics influence on the fiber's radiation response

3.4.1 Dose dependence of the RIA

RIA levels generally increase with the TID. For continuous exposures, the growth kinetics of the RIA with dose depends on the relative contribution of the generation rate and bleaching rate for the defects absorbing at a specific wavelength of interest. This results in various laws for the RIA vs dose curves ranging from linear dose dependence for fibers presenting limited bleaching as P-doped fibers, to sub-linear growth for Ge-doped fibers or more complex behaviors for pure-silica core or F-doped fibers whose response is related to room temperature unstable defects [14]. Studies of the dose dependencies in COTS SMF and MMF can be found in [52] for the near-IR part of the spectrum and in [53] for COTS and prototype MMF and for the visible part of the spectrum. The competition between the generation and the bleaching of defects is also strongly dose rate dependent and both dose and dose rate effects are related [14].
For pulsed irradiations of few ns of duration , the bleaching rate during the ns pulse is limited and a linear dose dependence of the RIA is observed [54] for fibers containing phosphorus or germanium. However, the dose dependence is not linear for PSC fibers, nor for fluorine-doped fibers [14].

3.4.2 Dose rate dependence of the RIA

Due to time constraints, the radiation response of optical fibers is very often evaluated with accelerated testing at higher dose rates with respect to the target application one. The dose rate dependence of RIA has been evaluated to

ensure the validity of these tests [55]. For most fibers, the RIA increases with the dose rate. This is explained by the competition between the generation of point defects and their bleaching at the temperature of the experiments. When the dose rate increases, the defects are more rapidly generated and fewer defects are bleached during irradiation [14]. For pure-silica core optical fibers and germanosilicate fibers, the above-mentioned dose rate dependence of RIA has been observed [56][57]. Fluorine-doped SMF installed at the LHC have also shown a dose rate dependence when tested [58].
Finally, it is worth to comment on the relationship between dose rate dependence and annealing in a fiber. In particular, the faster the annealing, the stronger the dose rate dependence. This can be explained by a competition between colour centre population and depopulation: the lower the dose rate, the longer the time to reach a certain dose, the more colour centres anneal already during irradiation. Saturation is reached when the colour centre production rate becomes equal to the colour centre annealing rate. Since the annealing rate is proportional to the number of already existing colour centres, in other words to the induced loss, the saturation loss value has to increase with increasing dose rate. The induced loss of fibers with negligible or very slow annealing is almost independent on dose rate. Such fibers care the most suitable for dosimetry [59].

3.4.3 Temperature dependence of the RIA

In general, radiation induced changes strongly depend on the operating temperature which may impact on the stability of the optically active defects and often even a few degrees of difference may lead to observable variations in the RIA [60]. While in first approximation one could consider that an increase in temperature implies an increase in the bleaching rate of point defects, the actual resulting effect on the RIA at a given wavelength is more complex. In particular, it is known that a defect structure can convert into a different one counterbalancing the first effect.
It has been observed that increasing the temperature of irradiation can rather have no influence (P-doped fibers), decrease (Ge-doped fibers or PSC fibers at 350 nm) or strongly increase (PSC fibers in the UV) the RIA levels at certain wavelengths. For fixed conditions of irradiation, the temperature influence can evolve with the

time of irradiation.[61]. In particular, it has been observed that for temperature ranging between 5°C and 50°C, the RIA is independent from temperature for P-doped fibers in the UV and visible spectra [16]. To be noted that it has been observed that at 865 nm, for temperature above 75°C, the increase of induced loss with the dose isn't linear anymore [62]. The temperature (in)dependence of P-doped fibers may be however different in the NIR spectral range where there is also a temperature dependence of P1 defects. For example, at 1550 nm Faustov et al. observed a 10% sensitivity increase when raising the temperature from 30°C to 80°C [51]. This unexpected inverse relationship between RIA and temperature confirms that the temperature dependence of P-doped fibers in the NIR should be more investigated.
Finally, Faustov et al. also observed a temperature dependence of Al-doped fibers at 1550 nm: a 25% decrease in the absorption level of the fiber under test for a variation of the temperature from 30°C to 80°C [51].

3.5 Application parameters influence on the fiber's radiation response

3.5.1 Wavelength influence

As detailed in Section 3.2.2, the RIA (and RIE as well) phenomenon is strongly dependent on the launched optical wavelength in the fiber 3.4. This is due to the various structures of point defects generated in the glass matrix that are associated with absorption bands centered at different wavelengths and with different full-widths at half maximum shown in 3.6,3.8, 3.7 [14].
The dependence of the RIA on the wavelength allows for further optimization according if the targeted application requires higher or lower sensitivity.

3.5.2 Launched power influence

Injecting a high-power signal into a fiber can result in the annealing of the previously existing point defects through a process known as photobleaching [63], which reduces the RIA. The behaviour of the bleaching and its extent depends strongly on the fiber's composition. It has been shown that in some fibres the

radiation induced loss can be reduced 2 to 3 times for lengths of 5 to 30 m, while for longer fibres the optical signal used for photobleaching gets attenuated, due to the intrinsic loss of the fibre, reducing the effect [64].
More in general it has been shown that the launched optical power should remain below 15 μW to avoid photobleaching [60][65]. This is particularly important for radiation sensing application where photobleaching should be avoided in order not to loose the information on the accumulated dose by decreasing the RIA. On the other hand, photobleaching could be used to regenerate an irradiated fiber in order to re-use it for further sensing although the technical implementation of such technique might be quite complex.

3.5.3 Fiber history and pre-treatments influence

The sensitivity of a fiber can be influenced by previous irradiation history. For example, when interested in improving the radiation hardness of a fiber, pre-irradiating a fiber could be a solution. In fact, precursor sites or then converted into optically-active defects, to then apply a thermal or hydrogen treatment to bleach them. During the second irradiation the number of precursor sites will be reduced as well as the RIA [14][66].
Differently, it has been observed that the sensitivity in most P-doped fibers can change after long term radiations, which would require a new calibration after a few months in dosimetry applications [18].

3.5.4 Radiation type dependence

It seems to be reasonable to assume that different types of ionizing radiation could induce the same attenuation in fibers provided that they deposit the same dose. The ionization density of protons, alpha particles and heavier ions is much higher than the one caused by gamma rays, X-rays, and electrons [59]. This can lead to charge carrier recombination and saturation effects in more dense ionization tracks and as a consequence, to lower induced losses, as discussed in more detail in [67]. This is at least valid as long as the concentration of defects within the fiber core that can act as precursor of light absorbing colour centers, is given by the fiber production process, for instance at the beginning of an irradiation.

As already introduced in Chapter 2 of this Thesis, X-rays and gamma rays above an energy of about 0.7 MeV, as well as highly energetic electrons, protons, alpha particles and heavier ions can loose a fraction of their energy by non ionizing collisions that cause structural damage within the fiber core, as for example a new defect that can act as precursors of colour centres. The structural damage caused by heavier ionizing particles can become orders of magnitude higher than that caused by the same dose of gamma rays or electrons. In principle, above a certain fluence value, it is therefore to be expected that heavier, more densely ionizing particles will finally lead to a higher induces losses than gamma rays or electrons of the same dose rate. In [67], it has been estimated that this will happen for a 14 MeV neutron fluence above $5 \cdot 10^{13}$ n/cm^2 which is in the order of 10^{14} n/cm^2 at 1 MeV. The radiation environment of our concern throughout this Thesis, considers radiation levels of a few tens of Gy up to 100 kGy (annual) which correspond to about 10^{10} – 10^{14} n/cm^2 of 1 MeV equivalent neutron fluence. We will be thus mostly dominated by the TID effects while the NIEL will be of minor concern for our application.

Reference [67], has also shown that fibers with higher induced loss during gamma irradiation will also show a higher induced loss during fast neutron irradiation with the same dose rate.

These considerations, validate gamma irradiation testing at ^{60}Co facilities which are cheaper and more easy to perform with respect to protons or fast neutrons irradiations. Therefore the following procedure could help to reduce the number of more expensive and more difficult irradiations with protons or fast neutrons: as a first step one selects with 60Co gamma irradiations the most radiation hard one out of a greater number of otherwise comparable fibres. For neutron and proton fluences $\leq 10^{13}$ cm^{-2} the induced loss caused by the gamma rays should be an upper limit also for neutron and proton irradiations. A fiber resulting resistant to gamma irradiation should therefore confidently be used as radiation resistant also in environments presenting for example protons or fast neutrons. Only for higher particle fluences, neutron and proton irradiations could become necessary [59].

3.6 Optical fiber's radiation response theoretical models

Nowadays, different empirical or semi-empirical models exist allowing to predict the growth and decay kinetics of RIA versus the dose or time after irradiation, provided a sufficient amount of data is given on the fiber. In the following subsection a brief overview of some of the most used models will be given.

3.6.1 Linear model

The simplest model is probably the linear one relating the RIA to the dose (D) in the following way:

$$RIA = c \cdot D \tag{3.1}$$

where c represents the sensitivity to dose of the fiber and is expressed in dB/km/Gy. If the relationship is inverted and the the dose is expressed as function of the the RIA as $D = \frac{1}{c} \cdot RIA$, $\frac{1}{c}$ represents the calibration factor which allows to calculate the dose from an RIA measurement.
This kind of model is suitable for the fitting of the linear part of P-co-doped fibers, usually up to a couple of kGy.

3.6.2 Power law model

From [18] the increase of fibre attenuation (A) with does (D) can be approximated by the following power-law model:

$$A = cD^f \tag{3.2}$$

where the constant c expresses the radiation sensitivity and the exponent f is nearly 1 for well-suited fibres (fibers with slow annealing of the induced attenuation). Such model is capable of predicting or fitting that radiation response (during irradiation only) for a wide range of pure silica, germanium and erbium-doped fibers with various degrees of accuracy [53].

3.6.3 Semi-empirical model

Another model which was successful for a selection of fibers is the following semi-empirical model involving three parameters, the stretched saturating exponential, with D_S the saturating dose, $0 < f < 1$, a fractal coefficient linked to a distribution of activation energies rather than a single activation energy [53]:

$$A = C'1 - exp(-D/D_S^f) \tag{3.3}$$

3.6.4 First order kinetic model

Finally, in [51] it is said that although the power law model may be indeed accurate in fitting the data in many examples, at the low dose limit, when the dose tends to zero, it predicts an infinite speed of the RIA increase. It is also stated that at high doses, when the saturation becomes more apparent, this model cannot be used either. For these reasons Faustov et al. prefer to use the following first-order kinetic model to describe the loss behaviour as a function of the dose and the wavelength:

$$\frac{\partial n}{\partial t} = a\dot{D} - \frac{n}{\tau} \tag{3.4}$$

where n is the defect concentration, $\dot{D}$ is the dose rate, a is the probability of defect generation and τ is the characteristic lifetime. The solution is a saturating exponential of the form [53]:

$$n = a\dot{D}\tau(1 - exp(-t_i/\tau)) \tag{3.5}$$

for an isothermal at constant dose-rate regime. The transformation to a dose-equivalent formulation may be obtained by considering $D_S = \dot{D}_\tau$ and $D = \dot{D}_{t_i}$. The characteristic lifetime is temperature dependent. More sophisticated models which take into account the radiation-assisted recombination of defect centers or the depletion of precursor sites in the glass network, may mitigate the dose-rate and/or temperature dependence [53].

If we assume the presence of several types of colour centres, we may write an

expression for the RIA consisting in the sum of saturating exponents [**?**]:

$$A(D,\lambda) = \sum_{i}^{k} a_i(\lambda)\left(1 - exp\left(-\frac{D}{D_i}\right)\right) \tag{3.6}$$

where k is the number of exponents used for the fitting, a_i is an empirical wavelength-dependent constant and $D_i = \dot{(}D)\tau_i$. These constants might be considered as the attenuation at the saturation and the saturation dose related to a corresponding point-defect characterised by the absorption band at that particular wavelength although no evidences of the physical origin are known until now [51].

4 Optical fiber distributed dosimeters based on RIA

This Chapter will introduce the main principles behind spontaneous light scattering in media as well as provide an overview of optical fiber sensor technology with a main focus on distributed optical fiber sensing and distributed radiation sensing.

4.1 Spontaneous light scattering

In the presence of spontaneous light scattering, the optical properties of the medium in which light propagates are unmodified by the presence of the incident light beam itself. This condition is verified when the intensity of the incident light is sufficiently low. Under such circumstances, the scattering is generated by the mechanical or thermal excitation of the medium with an intensity that is proportional to the intensity of the incident light. On the other hand, if the intensity of the incident light is sufficiently large to modify the optical properties of the material, the scattering process turns to be nonlinear. In such case, the scattering is generated by the material fluctuations by the incident light and the process is known as stimulated scattering [68].
When light propagates through matter several scattering processes can occur and they are generally classified into two types:
Elastic scattering: is a process in which photons are scattered maintaining their energy, so that they have the same frequency of the incident light.
Inelastic scattering: incident photons give or receive energy to or from the medium, leading to scattered photons shifted in frequency. By definition, the com-

ponents of the scattered light which are shifted to lower frequencies are known as Stokes components while those components which are shifted to higher frequencies are known as anti-Stokes components.

Scattering is originated from the interaction of light with the excitation of the medium. From quantum theoretical approach, scattering can be described as the interaction between the quanta of light, the photons, and the quanta of medium excitation which are phonons. While the quantum theory can adequately describe the interaction for low light intensity levels, when there is a strong excitation of the medium due to the high intensity of light, the semi-classical wave theory turns to be more appropriate to describe the scattering process. If we consider an inhomogeneous medium, the scattering process removes some photons of the incident light and produces scattered photons that might be shifted in direction, phase and frequency.

Fig. 4.1 shows the spectrum of scattered light (under normal light conditions) in which Raman, Brillouin, Rayleigh and the Rayleigh-wing features are visible.

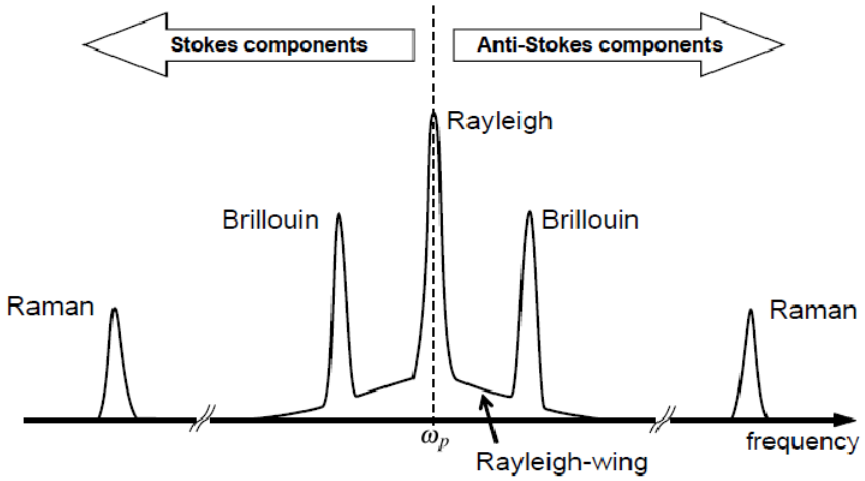

Figure 4.1: Spectral components resulting from light scattering in an inhomogeneous medium

In the following, a concise overview of each scattering processes is provided.

Rayleigh Scattering

Rayleigh scattering is the scattering of light from non-propagating density fluctuations. Formally, it can be described as scattering from entropy fluctuations. It is known as quasi-elastic scattering because it induces no frequency shift.

Rayleigh-wing Scattering

The scattering in the wing of the Rayleigh line is scattering from fluctuations in the orientation of anisotropic molecules. Since the molecular reorientation process is very rapid, this component is spectrally very broad.

Raman Scattering

Raman scattering results from the interaction of light with the vibrational modes of the molecules constituting the scattering medium. Raman scattering can equivalently be described as the scattering of light from optical phonons.

Brillouin Scattering

It is the scattering of light from sound waves that is, from propagating pressure (and thus density) waves. Brillouin scattering can also be considered to be the scattering of light from acoustic phonons.

4.1.1 Perturbed wave equation

From Maxwell's equations it is possible to derive the following perturbed wave equation which properly describes the propagation of light through a medium [69][70]:

$$\Delta^2\mathbf{E} - \frac{1}{c^2}\frac{\partial^2\mathbf{E}}{\partial t^2} = \mu_0\frac{\partial^2\mathbf{P}}{\partial t^2} \tag{4.1}$$

where $\mathbf{P}$ is the polarization field, $\mathbf{E}$ is the wave electric field, c is the speed of light in vacuum, and μ_0 is the magnetic permittivity in the vacuum. In a linear regime, the polarization $\mathbf{P}$ is proportional to the wave electric field $\mathbf{E}$ according to:

$$\mathbf{P} = \varepsilon_0\boldsymbol{\chi}\cdot\mathbf{E} \tag{4.2}$$

where χ is the dielectric susceptibility of the medium and ε_0 is the vacuum dielectric permittivity. In an isotropic and homogeneous medium, the tensor χ reduces to the scalar quantity χ, so that Eq. 4.1 becomes:

$$\Delta^2\mathbf{E} - \frac{n^2}{c^2}\frac{\partial^2\mathbf{E}}{\partial t^2} = 0 \tag{4.3}$$

where $n = \sqrt{\varepsilon/\varepsilon_0} = \sqrt{1+\chi}$ is the medium refractive index and ε is the dielectric constant of the medium. Eq. 4.3 is very similar to the wave equation 4.1 for propagation in vaccum. The only difference is that the speed of light in the medium is defined as c/n instead of c.
It is important to note that given that the variations in the dielectric susceptibility have been neglected, the light as described by Eq. 4.3 propagates without being affected by scattering. Real media however, are neither homogeneous nor isotropic, so that the spatial and temporal fluctuations of the dielectric susceptibility $\Delta\chi$ need to be taken into consideration as follows:

$$\mathbf{P} = \varepsilon_0\boldsymbol{\chi}\cdot\mathbf{E} + \varepsilon_0\boldsymbol{\Delta\chi}\cdot\mathbf{E} = \boldsymbol{P_0} + \boldsymbol{P_d} \tag{4.4}$$

where $P_0 = \varepsilon_0\boldsymbol{\chi}\cdot\mathbf{E}$ is the linear polarization and $P_d = \varepsilon_0\Delta\boldsymbol{\chi}\cdot\mathbf{E} = \Delta\varepsilon\cdot E$ is the induced polarization. To be noted that while P,P_0, P_d and E are vectors, $\boldsymbol{\Delta\chi}$ and $\boldsymbol{\Delta\varepsilon}$ are tensor quantities which are responsible for scattering processes. The perturbed wave equation therefore results in:

$$\Delta^2\mathbf{E} - \frac{n^2}{c^2}\frac{\partial^2\mathbf{E}}{\partial t^2} = \mu_0\frac{\partial^2\boldsymbol{P_d}}{\partial t^2} \tag{4.5}$$

Several scattering processes are defined by the right-hand side of Eq. 4.5. To have a better understanding of each scattering process, it is worth to analyze the elements $\Delta\varepsilon_{ij}$ of the tensor $\boldsymbol{\Delta\varepsilon}$. There are two contributions to this tensor, the scalar term $\Delta\varepsilon$ and the tensor component $\Delta\varepsilon_{ij}^{(t)}$, such that:

$$\Delta\varepsilon_{ij} = \Delta\varepsilon\delta_{ij} + \Delta\varepsilon_{ij}^{(t)} \tag{4.6}$$

Fluctuations in the thermodynamic quantities, such as pressure, entropy, density or temperature give rise to the scalar contribution $\Delta\varepsilon$. The scattering resulting from $\Delta\varepsilon$ is called "scalar light scattering" and is the origin of Rayleigh and

Brillouin scattering [70]. Rayleigh scattering is induced by entropy fluctuations while Brillouin scattering is induced by density variations associated with pressure waves propagating through the medium. The scattering coming from the tensorial contribution $\Delta\varepsilon_{ij}^{(t)}$ is called "tensor light scattering" [70]. The tensor is composed of two statistically independent tensor terms:

$$\Delta\varepsilon_{ij}^{(t)} = \Delta\varepsilon_{ij}^{(s)} + \Delta\varepsilon_{ij}^{(a)} \tag{4.7}$$

where $\Delta\varepsilon_{ij}^{(s)}$ is the symmetric part of $\Delta\varepsilon_{ij}^{(t)}$ and gives rise to the Rayleigh wing scattering which is due to the fast reorientation of the asymmetric molecules under the effect of an electric field. On the other hand, $\Delta\varepsilon_{ij}^{(a)}$ is the asymmetric part of $\Delta\varepsilon_{ij}^{(t)}$ and gives rise to the Raman scatering which is due to molecular vibrations in the medium.
More in general, a scattering resulting from the tensorial contribution $\Delta\varepsilon_{ij}^{(t)}$ is called "depolarized scattering" because the degree of polarization of the scattered light is typically smaller than the one of the incident light [70].

4.1.2 Rayleigh scattering

If we consider that the density ρ and the temperature T are independent thermodynamical variables, scalar changes in the dielectric constant $\Delta\varepsilon$ can be expressed by the following expression [70]:

$$\Delta\varepsilon = \left(\frac{\partial\varepsilon}{\partial\rho}\right)_T \Delta\rho + \left(\frac{\partial\varepsilon}{\partial T}\right)_\rho \Delta T \tag{4.8}$$

The contribution of temperature variations can be ignored in the spontaneous scattering regime, as it provides less than 2% of the total variations in the dielectric constant. In addition, temperature variations are extremely low in the spontaneous regime, since the low light intensity causes a negligible increase in temperature. Scalar light scattering is therefore mainly determined by density changes rather than temperature variations, such that Eq. 4.8 can be reduced to:

$$\Delta\varepsilon = \left(\frac{\partial\varepsilon}{\partial\rho}\right)_T \Delta\rho \tag{4.9}$$

On the other hand, density variations $\Delta\rho$ can also be separated into two independent thermodynamic contributions from the pressure p and the entropy s, as follows:

$$\Delta\rho = \left(\frac{\partial\rho}{\partial p}\right)_s \Delta p + \left(\frac{\partial\rho}{\partial s}\right)_p \Delta s \tag{4.10}$$

where the first term describes adiabatic density fluctuations that produce Brillouin scattering while, the second one describes isobaric density fluctuations which give rise to Rayleigh-center scattering. In order to full describe the Rayleigh scattering, the following diffusion equation for the entropy fluctuations has to be considered [70]:

$$\rho c_p \frac{\partial \Delta s}{\partial t} - k\nabla^2 \Delta s = 0 \tag{4.11}$$

where c_p is the specific heat at constant pressure and k is the thermal conductivity. A solution to the diffusion equation is provided by:

$$\Delta s = \Delta s_0 exp(-\delta t) exp(-\mathbf{q}\cdot\mathbf{r}) \tag{4.12}$$

where $\mathbf{q}$ is the scattered wavevector and δ is the damping rate of the entropy disturbance given by:

$$\delta = \frac{k}{\rho c_p}|\mathbf{q}|^2 \tag{4.13}$$

The resulting dielectric constant variation can be used in the perturbed wave equation 4.5 to obtain the Rayleigh scattering component, assuming a monochromatic incident wave and replacing the exprssion for entropy given by Eq. 4.12 into Eq. 4.9 and 4.10. As a consequence of Rayleigh scattering, it is possible to find out that the induced polarization term $\boldsymbol{P_d}$ of Eq. 4.5 has only a component at the frequency of the incident light, resulting in an elastic scattering process.

4.2 Optical fiber sensors

Starting from the first experiments using optical fibers for sensing applications more than twenty years ago up to recent times, optical fiber sensing has undergone a remarkable progress and innovation over the last two decades. The main idea behind the function principle of any fiber sensor is based on the use of an optical fiber to guide light to an interaction region where the light signal itself is

modulated in response to a change in the local environment [3]. In fact, an environmental effect can induce a change in the optical signal in terms of intensity, frequency, phase, polarization and/or spectral content. Once the light is modulated with the environmental information it is guided back through the fiber to the receiver where the measured variables are recovered. Nowadays, a great variety of optical fiber sensors (OFS) exist [1][2] and can be classified into two families: "intrinsic" and "extrinsic" sensors as follows [1]:

Intrinsic Sensors: in such sensors it is the fiber itself which represents the sensing element. The environmental effects and conditions directly impress the information onto the light propagating in the fiber and is then accordingly modulated.

Extrinsic Sensors: here the optical fiber is only used to couple and carry light to and from a region where the light beam is influenced by the measured variable. In such cases the modulation of the light occurs in some suitable external device which is generally connected to the fiber by fusion-splicing or mechanical connection.

A further interesting classification of optical fiber sensors showing their great variety is provided here [1][2]:

Discrete sensor: Discrete fiber optic sensors as shown measure a particular physical quantity at a particular location. Usually they are also called "point sensors" and correspond to way in which most sensors operate. For practical applications, the difficulty is to predict the critical points well in advance where the sensors must be located. Usually, point sensors allow interrogation speeds up to several kHz making possible dynamic strain, acceleration, acoustic waves, temperature and pressure measurements. Fiber Bragg Grating (FBG) are a very well known and widely used type of point sensor [71][72], often utilized for Structural Health Monitoring (SHM) applications.

Quasi-distributed sensor: In such case many sensors can be multiplexed in a single system allowing for a large number of sensors to profit from the same optical fiber link. The physical quantity can therefore be measured in pre-determined positions along a fiber network. FBGs for example can be inscribed along the same optical fiber offering the possibility to measure for example strain in a set of points along the structure to be monitored. Various multiplexing techniques

can be implemented to discriminate a sensor from the other. For example, time, frequency, wavelength, spatial and polarization multiplexing are all possible [4]. Among these, wavelength division multiplexing (WDM) is certainly one of the most attractive ones as it uses optical power pulses very efficiently. In addition, it can be easily added to other multiplexing systems, allowing to use several sensors in a single fiber line.

Distributed sensor: Distributed sensing offers unique and very powerful sensing capabilities which are not possible using conventional sensors. In particular, they allow the physical quantity one wishes to measure, to be determined at any point along an optical fiber with an appropriate sensitivity and spatial resolution [73][74][75]. Distributed sensors are capable to spatially discriminate thousands of detecting points along the whole sensing fiber, therefore a single distributed optical fiber sensor (DOFS) can replace thousands of discrete sensors. Their operating principle has been widely employed for temperature and strain sensing using scattering effectts in the fiber such as Raman or Brillouin [76].

4.3 Distributed fiber optics sensing

Distributed optical fiber sensors (DOFS) offer a unique mechanism that allows to measure key physical quantities such as strain and temperature at any point along the fiber optic cable with great advantages over conventional electrical sensors in terms of flexibility, reliability and performance. DOFSs are particular effective to be used in applications where the monitoring of a single physical quantity is required at a large number of points, for example for large or very long structures. Another key feature of DOFSs is that they allow for simultaneous measurements of both the spatial and temporal behaviour of a physical quantity. This brings a new level of understanding especially useful for controlling the behaviour of large infra-structures. DOFS allow one to measure spatial distributions with a spatial resolution of 0.1-1 m over a distance of several kilometres or tens of kilometres. Among other well known important benefits of DOFS we may name lightweight, immunity to electromagnetic interference (EMI), no electrical power requirement at the sensing point and their mechanical flexibility allowing them to easily be embedded in a great variety of structures. DOFS are considered as a perfect

solution for several applications where conventional sensors such as foil strain gauges, thermocouple and vibrating wires have proven ineffective and difficult to be used in several practical conditions. Possible applications of a DOFS include [4]:

- Temperature measurements for fire alarm systems (for example in automotive or railway tunnels), electric power systems and harsh environments.
- Stress monitoring of large structures and vehicles such as bridges, dams, buildings, aircrafts, submarines or ships among other.
- Leakage detection in pipelines
- Embedded sensors in composite materials to form smart structures
- Ionizing radiation sensing at nuclear power plants or high energy physics accelerators

The most common DOFS are based on Rayleigh, Raman and Brillouin scattering. By monitoring the variation of Rayleigh back scattering signal intensity, one can measure the spatial variations in the fiber scattering coefficient providing local temporal information along the optical fiber, thus analysing the backscattered trace one can verify the integrity of the fiber. A Raman DOFS which will be treated in detail in Chapter 7 has the ability to sense the ambient temperature along a fiber, while Brillouin scattering-based DOFSs are sensitive to both temperature and strain.
The exciting feature that DOFS systems offer which is the ability to determine the value of physical quantity continuously as function of the distance along an optical fiber can be performed using different techniques such as optical time domain reflectometry (OTDR) [77][78][79] or optical frequemcy domain reflectometry (OFDR) [80][81][82]. Between these two techniques the most commonly used is OTDR which can be combined with different scattering phenomena. In addition, frequency-domain techniques generally have a higher complexity, higher costs and a smaller system bandwidth [76]. For these reason, this Thesis work will focus on OTDR-based systems.

4.3.1 Optical Time Domain Reflectometry (OTDR)

We will now investigate the working principle of OTDR on which many DOFS rely. The technique basically consists in injecting a short and high-peak power optical pulse into an optical fiber and measuring the backscattered Rayleigh power as a function of time [78][79]. If the group velocity of the optical pulse in the fiber is known it is straightforward to convert the time scale into the fiber-length scale z. The spatial information can therefore be obtained from the pulse round-trip time between the fiber input at $z = 0$ and a given position z along the fiber. This way in a conventional OTDR, temporal variations of the Rayleigh backscattered power level allow to measure local losses throughout the fiber. An OTDR device provides the detail about the local loss information throughout the fiber and this information can also be used precisely to calculate the attenuation coefficient. Due to the nonzero losses the power associated to the launched pulses is gradually attenuated along the fiber and consequently the backscattered power is also attenuated. While light propagates into the fiber, optical pulses encounter Fresnel reflections and Rayleigh scattering locations resulting in a fraction of the signal travelling back in the opposite direction which is linearly proportional to the optical power pulse at that location.

One of the main advantages of the OTDR technique is that it only requires the access to one single end of the fiber, in fact, both transmitter and receiver are placed at the same position, in $z = 0$. OTDR is often defined as an optical pulse-echo technique [83] which can be considered as a one-dimensional radar [76]. Fig. 4.2 shows the typical block diagram for an OTDR system.

A laser diode is driven by an electrical pulse generator that produces a train of short optical pulses. A photodiode is used to detect the backscattered optical power from the fiber through a directional coupler. The detected waveform of the optical signal is amplified and digitized through an ADC and analyzed by a digital-signal processing (DSP) unit. The timing of the DSP is synchronized with the source optical pulses so that the propagation delay of each backscattered pulse can be precisely calculated.

The losses in an optical fiber may be caused by absorption, scattering, bending and connecting. Most of these effects can be nonuniform along the fiber, especially if different fiber spools are connected together. Therefore, the fiber attenuation

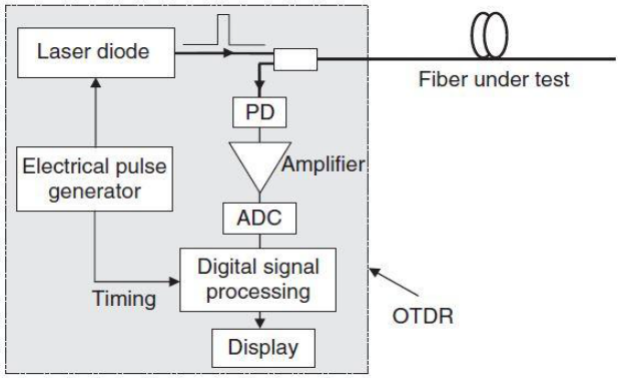

Figure 4.2: Block diagram of a typical OTDR system (PD: Photo-detector, ADC: Anolog-to-digital converter) [79]

coefficient is a function of the location along the fiber. In particular, the power level of the optical pulse propagating through the optical fiber typically exhibits an exponential decreasing evolution with the distance. The power distribution along the fiber can be expressed as:

$$P(z) = P(0)exp\left(-\int_0^z [\alpha_0(\xi) + \alpha_{RS}(\xi)]d\xi\right) \tag{4.14}$$

where P(0) is the input optical power $\alpha_{RS}(\xi)$ is the attenuation coefficient due to Rayleigh scattering and $\alpha_0(\xi)$ the attenuation coefficient caused by effects other than scattering along the fiber. Fig. 4.3 reports an illustration of the propagation features of both the optical pulse and the corresponding Rayleigh backscattered light.

If we consider an optical pulse that is launched into the fiber at t_0 with a pulse duration τ_p, the locations of the pulse leading edge and the trailing edge along the fiber at a given time t are $z_{le} = v_g(t - t_0)$ and $z_{tr} = v_g(t - t_0 - t_p)$ respectively, where v_g is the group velocity of the optical pulse. According to Eq. 4.14, the Rayleigh scattered power dP_{RS} from an infinitesimal small fiber region Δz at a position z along the fiber is given by [79]:

$$dP_{RS}(z) = P(z)\alpha_{RS}(z)dz \tag{4.15}$$

Considering that only a small fraction of this scattered power is coupled and propagated back into the fiber, the Rayleigh power which reaches the fiber input

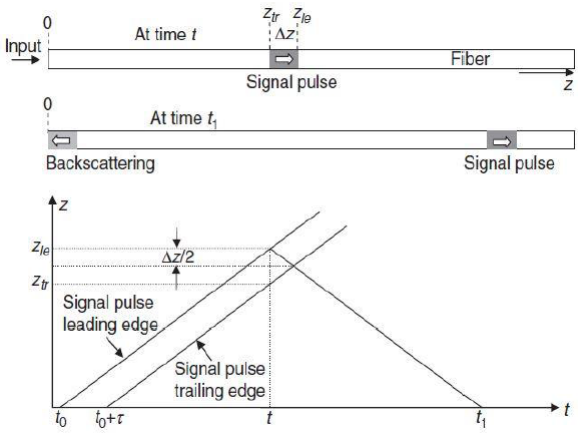

Figure 4.3: Propagation of pulse and its respective backscattering along an optical fiber in conventional OTDR technique) [79]

at $z = 0$ and is generated at a position z, can be express as [79]:

$$dP_{RS}(z) = P(0)S\alpha_{RS}(z)dz\ exp\left(-2\int_0^z \alpha(\xi)d\xi\right) \tag{4.16}$$

where $\alpha(\xi) = \alpha_0(\xi) + \alpha_{RS}(\xi)$ is the total fiber attenuation coefficient and S is the fraction of the light that is captured by the fiber and the backpropagated to the OTDR's receiver. The backscattering capture coefficient S is given by [77]:

$$S = \left(\frac{NA}{n_1}\right)^2 \frac{1}{m} \tag{4.17}$$

where $NA = \sqrt{n_1^2 - n_2^2}$ is the numerical aperture of the fiber, n_1 and n_2 are the refrective index of the fiber's core and cladding region and m is a parameter depending on the refractive index profile, usually equal to ~ 4.55 for single-modefibers [77], giving rise to a typical $S \simeq 0.13\%$ [79]. As shown in Fig. 4.3, the backscattered light that reaches the fiber input at a given time t_1 is originated from a short fiber section of length $W/2 = (z_{le} - z_{tr})$ where $W = v_g \cdot \tau_p$ is the extension of the fiber used by the optical pulse. The optical power of the Rayleigh component reaching the fiber's input as a function of the distance can therefore be given by [79]:

$$P_{RBS}(z) = \frac{v_g \cdot \tau_p}{2} P(0)S\alpha_{RS}(z)\ exp\left(-2\int_0^z \alpha(\xi)d\xi\right) \tag{4.18}$$

Given a pulse duration τ_p, the spatial localization of a point scattering center

cannot be better than:

$$\Delta z = \frac{\tau_p v_g}{2} \tag{4.19}$$

where Δz represents the spatial resolution of the OTDR. The factor 0.5 arises from the fact that the testing pulse and the backscattered signal travel in opposite directions, reducing the interaction length to half of the pulse duration W along the fiber as depicted in Fig. 4.3. This said, if we consider a typical refractive index of an optical fiber of 1.5 [69], a spatial resolution of 1 m for example will be obtained with a pulse duration of 10 ns.

For constant fiber parameters (S, α_{RS}, v_g), the backscattered power can be increased by increasing the energy of the sent pulse. This can be done either by increasing the peak power $P(0)$ or the pulse duration τ_p or the combination of both. It is however important to note that maximum peak pulse power is limited by the onset of nonlinear effects in the fiber and the possible saturation of the receiver caused by Fresnel reflections. On the other hand, an increase in the pulse duration will degrade the spatial resolution of the measurements. There is therefore a trade-off between the dynamic range and the spatial resolution resulting in a fundamental limit of the conventional OTDR technique.

The dynamic range of an OTDR in fact is related to the ability of the system to detect low and high optical power levels and is mainly related to the SNR of the measurements. One of the most important factors affecting the SNR is the noise of the optical receiver. This is especially the case when one wished to obtain high spatial resolution and/or long measurement distances. Shorter pulses imply higher spatial resolutions but carry less energy and require a broader receiver bandwidth which introduced additional noise which decreases the dynamic range.

In conclusion, it is very challenging to perform long distance measurements which require a high dynamic range with short testing pulses which would offer a high spatial resolution. To reduce the detrimental impact of noise, a "signal averaging" method [78] is often used. In such cases, the measurements are repeated N times and then averaged. If the system is dominated by noise with mean value equal to zero, the noise is automatically reduced by a factor equal to $\sqrt{N}$ implying that the electrical SNR of the measurements will also be enhanced by a factor $\sqrt{N}$. Of course, this implies an increment in the measurement time by a factor N [79].

4.3.2 Performance Parameters of DOFS

A general guideline for the use of optical fiber sensor is proposed in [3] where some terminology related to the sensing performance of DOFS is also included. A brief summary of this terminology is presented here as it useful for a better understanding of the next Chapters of this work.

- **Measurement dynamic range**: it is the ratio between the backscatter signal at the OFS front panel connector and the noise floor to be measured with the required accuracy. It is often expressed in dB.
- **Sensing range/distance**: it is the maximum fiber length over which the physical quantity can be measured within the stated performance (spatial and physical quantity resolution).
- **Sensitivity**: it is the variation of a measured variable at the detector, such as optical power or frequency, produced by unit change of the physical quantity. It is for example expressed in $\%/^{\circ}C$, $MHz/\mu\varepsilon$, etc.
- **Spatial resolution**: it is the smallest length of fiber over which any sensible change in the spatial variation of the physical quantity to be measured can be detected. It is determined by both the optical pulse width and the receiver bandwidth of the system. Often, two different definitions for the spatial resolution are proposed: 1) the "measuring spatial resolution" which is the minimum distance over which the system is able to indicate the value of the measured physical quantity within the specified uncertainty, 2) the "detection spatial resolution" which corresponds to the minimum distance that generates results which are within 10% of the measured physical quantity transition amplitude.
- **Measured physical quantity resolution or Precision**: this represents the smallest change in the physical quantity to be measured which can be detected by the DOFS. It is expressed by the estimated standard deviation of a specified series of measurements and is provided as a function of the distance for a particular spatial resolution and acquisition time.

- **Accuracy**: it qualitatively expresses the closeness of the measured value to the true value of the physical quantity. It represents the difference between the measured result andthe true value and is affected by both offset (bias) and precision. To be noted the difference between precision and accuracy: the smaller the dispersion of the measured values, the better the precision. Precise measurement results are not necessarily accurate due to possible bias from the real value.

- **Measurement/acquisition time**: it is the time required by the system to obtain results within the specified sensing performance.

- **Cross-sensitivity**: corresponds to an unwanted change of the measured variable due to the influence of physical factors other than the physical quantity one seeks to measure.

- **Repeatability**: it is the closeness of the agreement between the results of successive measurements of the same physical quantity carried out under the same conditions.

As for other measurement systems, there is always a trade-off between the above listed parameters For a given application one needs to find out the best possible compromise to optimize the measurements. For example, in the case of radiation sensing which is the topic of the Thesis dissertation, the highest possible SNR is needed to cope with the strong losses induced by ionizing radiation. At the same time a high spatial resolution is also needed to be able to detect very localized events. Fortunately, in many real cases where the dose rate are not very high (tens of μGy/s, corresponding to a few tens of kGy per year), the acquisition time is not a limitation. Measurements can be performed only a few times per day allowing for a significant amount of averaging to be done, hence a corresponding SNR enhancement.

4.3.3 Optical Pulse Coding Techniques for OTDR

As discussed in the previous sections, there exists a fundamental trade-off between spatial resolution and SNR limiting the resolution with which one can measure a physical quantity, the maximum sensing distance as well as the localization of

events. As mentioned earlier, an improvement in the SNR of OTDR measurement can be achieved by averaging a large number N of traces. An SNR improvement of a factor $\sqrt{N}$ can be thus obtained. This procedure however leads to longer acquisition times in a factor N. While this limitation is generally not critical for radiation sensors, it is in many applications where faster measurements are required. In such cases, in order to reduce the measurement time and still achieve high dynamic ranges it is possible to improve the noise characteristics of the receiver or increase the energy of the input pulses. The receiver improvement can be achieved by using low-noise avalanche photodiodes (APD) instead of standard PIN photodiodes but often this improvement is not enough to fully overcome the above-mentioned trade-off. For what concerns the energy of the pulses, as already mentioned in the previous sections this improvement is limited by the onset of nonlinear effects in the fiber in case of too high energy pulses. Of course the pulse width can be increased resulting however in a lower spatial resolution.
For such cases or simply when one needs higher SNR which could allow one to extend the measurement distance, improve the spatial resolution or enhance the resolution of the measured physical quantity, an additional approach can be implemented and will be briefly described below. Such an approach is based on spread-spectrum techniques [84][85] similar to those used in radar systems, allowing for higher dynamic ranges with a significant reduction in the measurement time without sacrificing the spatial resolution. The idea of the approach is based on "optical pulse coding" techniques which consist in spreading the signal in the time domain increasing therefore the average power and energy of the probe signal as well as the respective backscattered signal [84][85]. This can be achieved by launching into the fiber pulse sequences with some particular properties which allow one to obtain the impulse response of the fiber using a dedicated decoding process. Measurement with a higher dynamic range and SNR can then be achieved with a spatial resolution determined by the duration of each pulse contained in the sequences [84][85].
One important difference between radar systems and OTDR devices is that radars allow the use of bipolar coding techniques, meaning sequences containing -1's and 1's levels, while only unipolar codes containing 0's and 1's are suitable for OTDR systems. As a consequence, the amount of pulse coding schemes which can be effectively used in OTDR systems is limited. Among the various types of coding

schemes, two of them have shown real benefits to OTDR measurements systems: Simplex codes [85][86] and complementary-correlation Golay codes [84][87]. Details about Golay codes will be provided in Chapter 7 when we will discuss the Raman-based DOFS while a brief introduction to Simplex codes will follow here.

Simplex codes corresponds to a coding technique in which pulse sequences are derived from the Hadamard matrix [85][88], which is a bipolar matrix with particular orthogonal properties. Such a matrix has been widely used in spectroscopy [88][89], providing an efficient method to improve the SNR of the measurements. Due to its bipolar elements however, it is not possible to use Hadamard matrix directly in OTDR applications based on direct detection. In order to obtain suitable pulse sequences, Simplex codes require an Hadamard transform [88], which allows for the calculation of an S-matrix (Simplex-matrix) containing unipolar elements and orthogonal rows. Each row of the S-matrix defines a Simplex codeword [85]. The S-matrix can be constructed using methods involving maximal length shift-register sequences, quadratic residues and twin primes. It has been demonstrated that the optimum S-matrix, which minimizes the standard deviation of the decoded signal, can be derived from the Hadamard matrix by deleting the first row and first column, and then replacing 1's by 0's and -1's by 1's [89]. Thus, simplex coding can be easily implemented in OTDR applications by turning the laser ON and OFF, according to the sequences of 1's and 0's defined by the S-matrix [90]. More details about the working principle of Simplex codes for OTDR systems can be found in [91], but is worth to mention that the SNR enhancement or "coding gain" provided by Simplex coding for a code of length L can be expressed by:

$$G_{Simplex} = \frac{SNR_{Simplex}}{SNR_{Pulsed}} = \frac{L+1}{2\sqrt{L}} \tag{4.20}$$

An interesting demonstration of the improvement performance of a Raman-based DTS system has been demonstrated in [92] where the implementation of a 255 bit long code provided a 19.5 km increase in the interrogation range with respect to conventional OTDR (at comparable noise level) as depicted in 4.4 and in 4.5.

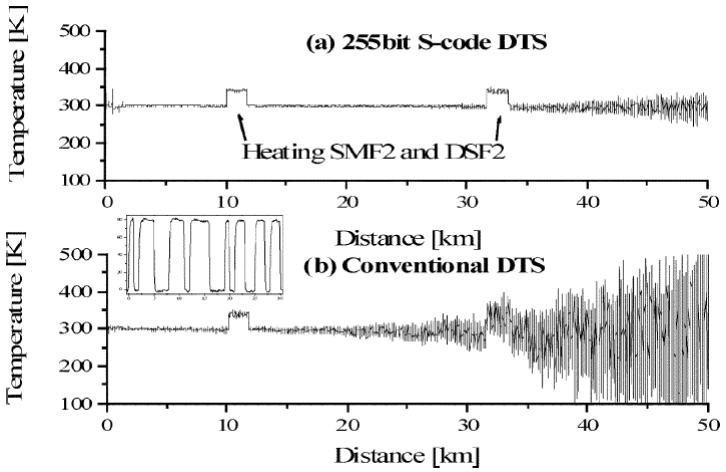

Figure 4.4: Measured temperature with (a) 255 bit coded and (b) conventional DTS Inset: LD output (first 30 bits of 255 code pattern)[92]

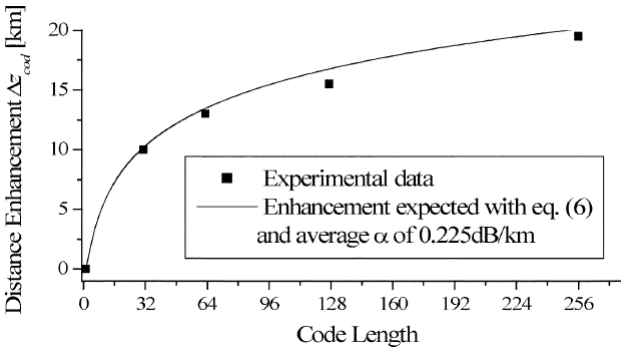

Figure 4.5: Increase in measurement range as a function of code length [92]

4.4 Distributed optical fiber radiation sensor (DOFRS)

As detailed in Chapter 2 of this Thesis, optical fibers suffer from high induced attenuation when exposed to ionizing radiation. This effect can be used for measuring the radiation intensity in terms of accumulated dose. Already in 1978 Evans et al. presented a fibre-optic radiation dosimeter that utilises the darkening induced in silicate glasses by ionizing radiation [10]. Later, in [93], it has been outlined that the increase of attenuation could be used for spatially resolving dosimetry by the means of the OTDR technique. The feasibility of such distributed fibre optic dosimeter systems was then confirmed in [94] where Rare Earth doped single mode fibers were used. One of the most interesting in-field demonstration has been provided by Henschel et al. in [18] where distributed optical fiber-based radiation sensing has been demonstrated and tested for the Tera Electron Volt Energy Superconducting Linear Accelerator (TESLA) Test Facility at DESY Hamburg using OTDR and Ge-doped multimode graded index fibres co-doped with phosphorus. The promising results presented in [18] included the ability to measure doses down to a few Gy with spatial resolution of a few meters. However, little has then be done to pursue with the realization of the presented techniques and further research is needed to verify the effectiveness of an OTDR-based distributed optical fiber radiation sensing (DOFRS) system at high energy physics and experiments. In particular, a DOFRS system needs to be characterized and tested to work in a complex mixed-field environment such as the one present in the LHC, where it will also need to be able to correctly monitor radiation levels with doses ranging over a wider span, from a few tens of Gy up to 100 kGy per year. In addition, the spatial resolution should be as high as possible in order to be able to take into account strong very localized losses.

In the following subsections, the methodology, requirements and possible limitation of the targeted DOFRS to be used at high energy physics accelerator and experiments facilities, will be provided.

4.4.1 Methodology and requirements for a DORFS at high energy physics accelerator and experiments facilities

By definition, an OTDR-based DOFRS presents very similar characteristics in terms of performances and limitations to an OTDR system presented in Section 4.3.1. Fig. 4.6 schematically shows the functioning principle of an OTDR-based DOFRS which follows a series of steps to reach the estimation of the dose profile. The first step consists in acquiring conventional OTDR traces once the interrogation (pulse width, wavelength) and acquisition (measurement time) parameters have been set. From the acquired traces which provide the backscatter light as function of the distance, a differentiation stage with respect to a spatial step is performed. The step is chosen to be equal or greater than the sampling resolution, typically a 5-10 cm for a launched optical power pulse of 10 ns and a fiber length of about 100 m. Once the differentiation is performed the RIA profile as function of the distance is obtained. It is then necessary to relate the measured RIA to the actual dose accumulated in the fiber. We have seen in Chapter 3 that various models exist to fit a fiber's response to radiation. Often, in the case of phosphorus-doped fibers, which are suitable candidates for dosimetry, a linear fit in sufficient at least up to a couple of kGy. In such case, by inverting the relationship $RIA = c \cdot D$ one can easily obtain the dose as $D = 1/c \cdot RIA$ where $1/c$ is the calibration factor (related to the sensitivity).
It is worth noting that, before the differentiation step, the smoothing of the initial OTDR trace is recommended in case of noisy traces. This process can be performed through some filtering method, as Savitzky-Golay algorithms do and have demonstrated good results in conserving the shape of the trace while improving the SNR by reducing the noise [18].

To be considered a valid monitoring system of radiation levels in the LHC and similar radiation environments, a DOFRS must fulfil certain performance requirements which are summarize as follows:

- Total Ionizing Dose: from a few tens of Gy up to 100 kGy
- Dose resolution: 10% of the TID.
- Dose rate: from a few μGy/s up to a few Gy/s

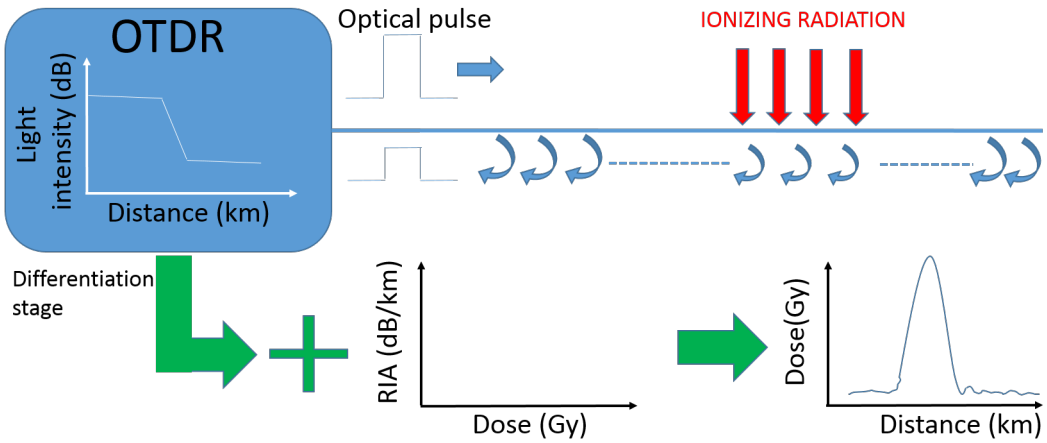

Figure 4.6: DOFRS system schematic block diagram

- Spatial resolution: ≤ 1 m
- Temperature: 15°C-35°C, hot spots: $200°C$

To achieve these, some requirements also exist on the sensing fiber:

- Ideally a linear increase of the attenuation with dose or simply modelled response
- Independence of the measured dose on the dose rate
- Negligible annealing
- Weak dependence on the radiation type and energy
- Independence on the environmental parameters, such as temperature

As explained in Chapter 3, the most suitable candidate to become the sensing fiber of an DOFRS are P-co-doped fibers which is why we will consider these all along the thesis as a base solution knowing that for high doses we will require another type.
Overall these high requirements make the realization of a DOFRS very challenging and will require optimization both on the selection of the sensing fiber as well as the interrogation/OTDR unit. In the next subsection the limitations related to the measurements and acquisition parameters will be presented.

Influence of launch and acquisition parameters on the DOFRS performance

The quality and accuracy of the obtained dose profile depend of course on the interrogation and acquisition parameters of the OTDR. In particular, the higher the dynamic range the better the SNR of the trace will be and will therefore allow a better detection of smaller dose quantities and to obtain a higher dose resolution. As mentioned earlier, the SNR also depends on the pulse width: the longer the pulse width the more energy will be sent in the fiber. On the other hand a longer duration pulse implies a smaller spatial resolution which is unwanted if one wishes to detect very localized losses. In fact, it is to be noted that if a loss occurs over a small length Δl which is smaller the the spatial resolution Δz, the loss magnitude will be anyway averaged over Δz resulting in an underestimation. The higher the magnitude of the induced loss and smaller the region over which the loss occurred, the higher this underestimation. In other words, a more important underestimation can be expected in areas with strong dose gradients over small fiber lengths.

The acquisition duration of the measurement also strongly impacts on the results, remembering that longer acquisition times allow for more averaging which leads to an SNR enhancement.

In Chapter 6 results from distributed optical fiber radiation sensing under mixed particle irradiation will be presented for different OTDR measurement and acquisition settings.

Finally, the possible temperature dependence of the RIA in the sensing fiber needs to be taken into account. If such a dependence is present and not negligible, a compensation method should be considered to avoid erroneous dose estimations. A possible method to overcome this problem would be to have a distributed optical fiber temperature sensing system, only sensitive to temperature, working in parallel to the radiation sensing system and allowing to decouple the temperature from the dose contribution in the DOFRS measurement.

5 ^{60}Co characterization of selected P-doped fibers

Based on the theory presented in Chapter 3 of this thesis, we have understood that P-codoped fibers are among the most promising candidates for optical fiber radiation sensing. For this reason, we have selected a SM and three different MM commercially available fibers and fully characterized them to understand their response when irradiated. Such characterizations, detailed in this Chapter, represent the first important step for the feasibility study of a distributed optical fiber radiation sensing system and have been carried out at the ^{60}Co facility of the Fraunhofer-Institut für Naturwissenschaftlich- Technische Trendanalysen INT in Euskirchen (Germany).

5.1 Experimental setup

The experimental setup which we used for our measurements is a setup used at Fraunhofer INT [60] to carry out the irradiation tests on the fibers and is depicted in Fig. 1 [65].

5.1.1 The ^{60}Co source

The irradiation system used at Fraunhofer INT to carry out the irradiation tests on the fibers is the Gammamat TK1000 ^{60}Co by *Isotopentechnik Dr.Sauerwein Gmbh* depicted in Fig. 5.2 where it is possible to appreciate the shielding container in which the small radioactive pellet of 7 mm x 10 mm is stored.

The pellet can be moved into the steel tube within less than half a second. This position is well defined and located in the center of the upright standing

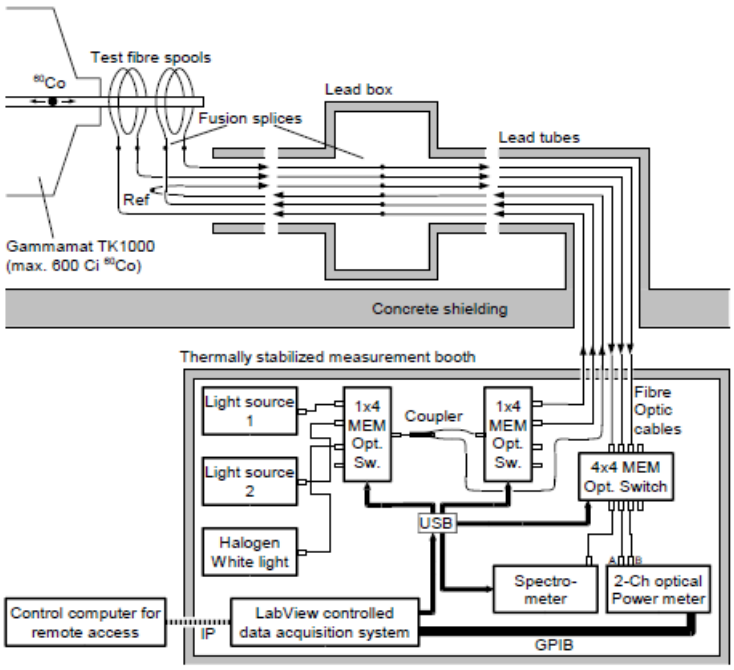

Figure 5.1: Experimental setup for irradiation tests on optical fibers using the Gammamat TK1000 ^{60}Co source at Fraunhofer INT [60]

sample spools as shown in Fig. 5.2. When the radiation source is in ejected position, it is surrounded by more than 0.5 m^3 of open space except for the guiding steel tube. It is therefore not directly enclosed in shielding material which could moderate the energy spectrum of the primary radiation and generate high levels of backscattering which could then cause inhomogeneous energy deposition and would make the dosimetry calculations more complex.
The dose rates which were achievable at the moment we performed the irradiation tests range from 0.5 mGy/s up to 1.7 Gy/s and could be set by placing the fiber samples at different distances from the radiation source in its ejected position.

5.1.2 Optical fiber sample preparation

As can be seen in Fig. 5.2, the fiber samples are wound up on aluminium reels of different diameters (between 4 cm and 30 cm) shown in Fig. 5.3 and allowing to select the dose rate to which the fiber was exposed to. The preparation of the sample is carried out with a dedicated spooling system allowing to achieve a homogeneous and stress-free sample spool such to minimize possible microbending

Figure 5.2: The Gammamat TK1000 ^{60}Co irradiation system with reels mounted on it

losses. The spool radius is measured both before and after the fiber sample has been wound up with a standard uncertainty of 0.5 mm.

To keep the impact of noise and possible drifts below a few percent, the expected total RIA is kept above 1 dB by selecting an appropriate sample length. At the same time to obtain homogeneous light power distribution in the fiber the expected RIA should be kept below 5 dB otherwise some unavoidable photobleaching effects could change significantly along the fiber [95]. In fact, if a fiber exhibits strong photobleaching and total RIA at the end of irradiation is high, the measured losses would increase along the fiber with decreasing light power leading to overestimation of the losses compared to those that would have been obtained at constant light power in a shorter sample (with smaller total induced loss)[96]. For

our characterizations, the sample length ranged from 8 cm up to 100 m. Taking also into account the spooling process, the combined standard uncertainty of the fiber sample length is evaluated not to exceed 2% or 2 cm, whichever the greater. Once the samples have been prepared from the pristine fiber and have been wound up on the reels, they are positioned in the irradiation area where they are spliced to radiation hard lead fibers which are known to have a very low radiation sensitivity. In this way, even if a few centimeters of the lead fibers are irradiated, the impact on the measured signal is negligible.

Figure 5.3: Different size aluminium reels for fiber sample spooling

5.1.3 Measurement equipment and irradiation conditions

The measurement equipment is located in a shielded booth which is thermally stabilized at $23°C \pm 0.1°C$. There, as well as in the irradiation hall, the temperature, humidity and ambient light are constantly monitored. Two fibers samples can be irradiated simultaneously given that two aluminum reels can be mounted at the same time.

From the optical point of view, both discrete light sources at 830 nm, 1312 nm and 1570 nm as well as a white light source are available for the characterization of MMF and SMF respectively. All the sources are connected to a first 1x4 MEM optical switch which allows to alternatively select the light source to be sent in the sample. At the output of the switch a mode-insensitive achromatic coupler

splits the light into two paths: the first, leading to a second 1x4 MEM optical switch which allows to select to which sample the light will be sent to (through radiation hard lead fibers permanently installed) and the second path into a fiber directly reaching the irradiation source back and forth and which serves to carry and monitor the reference signal. The signal coming back from the sample, always through radiation hard lead fibers, is then sent to a 4x4 MEM optical switch which distributes the signal among a high precision two channel optical power meter and a calibrated spectrometer.

A single sample can always be tested with two wavelengths at the same time, 830nm and 1312 nm for the MM fibers and 1312 nm an 1570 nm for the SM fibers. The output light power is monitored for some hours in order to check the optical stability of the complete system including light sources, the samples and the detectors, before the irradiation start. Usually, the absolute variation of the light power in the channels, mostly due to drifts of the light source, is about 0.01 dB. This can be compensated by subtracting the signal of the reference channel from the measurement signal resulting in a stability below 0.005 dB over several hours. Once the setup's stability is verified the ^{60}Co source is pushed out of the shielding container and starts irradiating the samples. The light power is then recorded as a function of time both for the samples under test as well as for a reference fiber. By subtracting the initial power before the start of irradiation it is possible to calculate the attenuation. The resulting RIA is then divided by the optical fiber sample length so that the results may be given in dB per unit length. To minimize the effects of photobleaching, the launched light power is maintained relatively low, between $7\mu W$ and $15\mu W$.

All the instrumentation is remotely controlled by a dedicated software situated outside the booth. It is worth noticing that at the beginning and at the end of irradiation, the data is collected with higher frequency and lower averaging times than during the rest of the irradiation to ensure following the faster processes with a proper time resolution immediately after the ^{60}Co source has been ejected and moved back.

5.2 Discrete and spectral measurements results

5.2.1 Multimode fibers (MMF) radiation response

For the study of the multimode fibers, two different commercially available candidates have been considered: a MM GI 50 $\mu m/125\mu m$ from j-fiber and a MM GI 50 $\mu m/125\mu m$ from OFS. In both cases the exact composition of the fiber is unknown as this information is not provided by manufacturers but the fibers are been said to be "radiation sensitive" meaning that they contain phosphorous in addition to germanium. The radiation response of these fibers is assessed by measuring the RIA as function of the absorbed dose at different dose rates.

MMF j-fiber

The irradiation of the MMF from j-fiber has been carried out at different dose rates ranging from around 0.5 mGy/s up to around 1.7 Gy/s and reaching about 60 kGy of total dose. The measured RIA has been plotted as function of the total accumulated dose in the fiber as shown in Fig. 5.4 and Fig. 5.5. It is to be noted that if not otherwise specified, the dose unit Gray (Gy) means Gy(SiO_2) throughout the whole thesis.

The general response to dose is linear in double logarithmic scale up to a couple of kGy after which it starts to saturate. In particular, based on the first derivative of each curve, the linear range has been calculated for different tolerance margins. Table 5.1 shows the maximum dose values reached in the linear range for the two optical wavelength used in the measurements. The lower limit of the linear range generally starts at around 150 Gy. It is also to be noted that the curves corresponding to the irradiations at 46.7 mGy/s and 153 mGy/s were particularly noisy at the beginning of irradiation, most probably due to the low statistics.

It is important to note that only for the irradiations at dose rates of 46.7 mGy/s, 153 mGy/s and 0.52 Gy/s it was possible to reach saturation. It is therefore difficult to state to which extend the linear range depends on the dose rate. The sensitivity of the fiber was found to be between 3 and 3.5 mdB/m/Gy over the whole range of dose rates at 830 nm and around 1 mdB/m/Gy over the whole range of dose rates at 1312 nm.

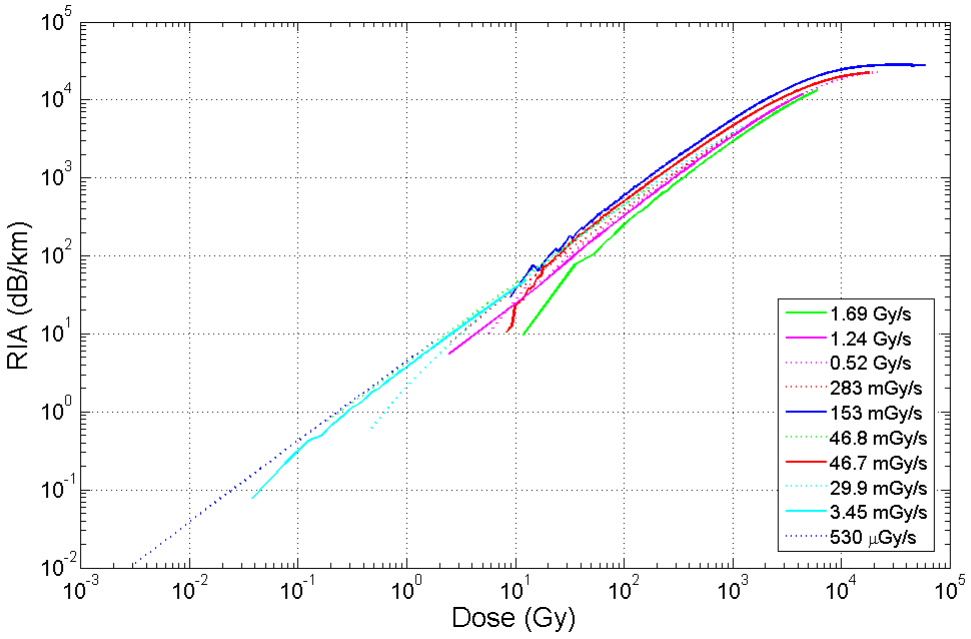

Figure 5.4: RIA as function of absorbed dose for different dose rates at 830 nm

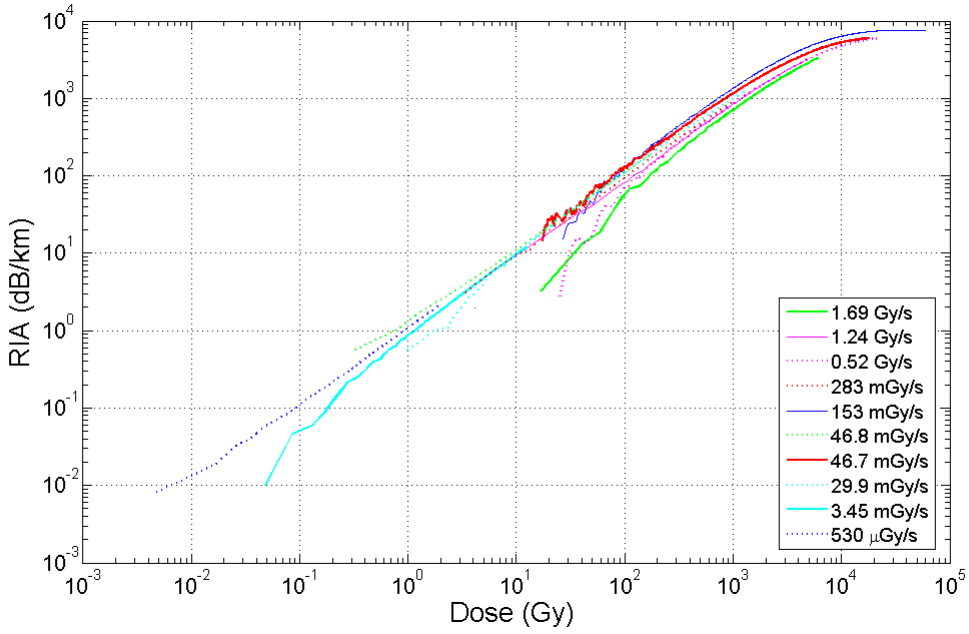

Figure 5.5: RIA as function of absorbed dose for different dose rates at 1312 nm

Table 5.1: MMF j-fiber, maximum absorbed dose in the linear range for different tolerance values

Tolerance	λ_1 = 830 nm	λ_2 = 1312 nm
5%	2185 Gy	1650 Gy
10%	2510 Gy	2000 Gy
20%	3180 Gy	2785 Gy

From Fig. 5.4 and 5.5 it is also possible to observe a correlation between the dose rate and the measured RIA. At 1 kGy for example, the maximum difference in RIA occurs between the measurements carried out at 153 mGy/s and 1.69 Gy/s and results in almost a factor 2. As the relationship between the RIA and dose rate doesn't show a clear pattern, the reason for this correlation may be in the measurement conditions. It might also depend on the particular composition of the fiber which is kept confidential by the manufacturer. Using the absolute value of the RIA to determine the dose is therefore unreliable as the uncertainty on the dose for a given RIA would be in the order of 30% – 40%. However, for radiation monitoring in high energy physics applications, determining the variation of the RIA would be sufficient and this can be reliably achieved if the slopes of the curves at different dose rates are comparable within certain limits, which for our purpose is about 20%. Therefore, the derivative of the linear part has been computed for each curve resulting in a maximum variation of the slope of around 15% both for the 830 nm and 1312 nm measurements which is indeed acceptable. As mentioned previously, only in three cases were we able to reach saturation. The study of the non-linear part in double logarithmic scale before saturation is therefore less meaningful. However, the non-linear part of the curves which did saturate have been compared by interpolating one to the other and calculating the root mean square estimator finding an %RMSE ranging from 5%–25%. It is therefore possible to use the non-linear part of the curves for estimating the RIA in the context of radiation monitoring but it has to be kept in mind that the uncertainty will be relatively high.

Finally, the characterization of the fiber has been completed by sending a white light into it and taking spectral measurements with a spectrometer. The result, after a little more than 1 kGy of irradiation at 283 mGy/s is shown in Fig. 5.6

As could be expected from theory, it is possible to observe a strong decrease of

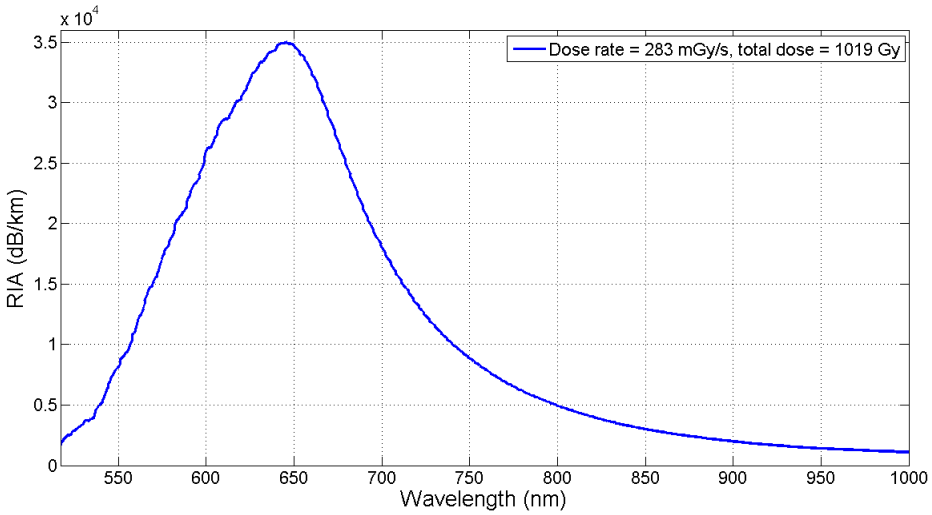

Figure 5.6: Spectral response at 1.02 kGy

the radiation sensitivity for the infrared wavelengths (700 nm - 1000 nm) leading to the typical RIA minimum of P-codoped fiber which is around $1\mu m - 1.1\mu m$ but is not visible on this spectrum due to the limited wavelength range of the spectrometer. The strong increase in radiation sensitivity for decreasing wavelength starting from 700 nm going down in the visible range is also P-codoped typical but the peak at around 650 nm with the sensitivity steeply dropping for shorter wavelengths is probably due to the specific composition of this fiber. The observed peak could be due to the tail of one of the POHC[5] defect absorption bands which is situated at 570 nm (2.2 eV, FWHM=0.25 eV).

MMF OFS

The irradiation tests on the multimode fiber from OFS have been carried out with dose rates ranging from 0.5 mGy/s up to 1.1 Gy/s and reaching a maximum of 55 kGy of total dose. The results in terms of RIA as function of the total accumulated dose are reported in Fig. 5.7 and Fig. 5.8 for the two different interrogation wavelengths respectively.
This multimode fiber from OFS shows a linear trend in double logarithmic scale up to a about 1.2-1.3 kGy both at 830 nm and 1312 nm, after which the RIA dependence on the dose becomes non linear and finally saturates at about 20 kGy.

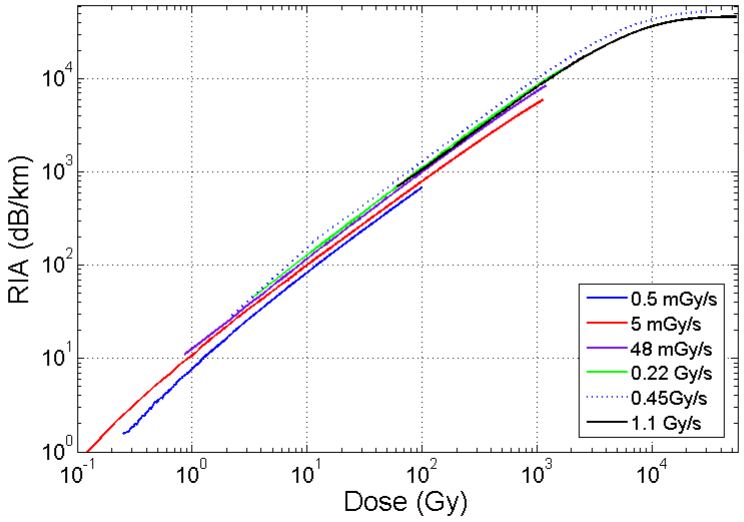

Figure 5.7: RIA as function of absorbed dose for different dose rates at 830 nm

The linear range start at about 150 Gy and its maximum is shown in Table 5.2 for different tolerance margins.

Table 5.2: MMF OFS, maximum absorbed dose in the linear range for different tolerance values

Tolerance	λ_1 = 830 nm	λ_2 = 1312 nm
5%	1330 Gy	1235 Gy
10%	1786 Gy	1770 Gy
20%	2838 Gy	2975 Gy

Saturation of the MM OFS has been reached only for the two highest applied dose rates, 0.45 Gy/s and 1.1 Gy/s, hence, as for the MM j-fiber, it is difficult to assess to which extend the linear range depends on the dose rate.

As can be seen from Fig. 5.7 and Fig. 5.8, the RIA measured in the MMF OFS shows a dose rate dependence. In particular, at 1 kGy the RIA variation due to dose rates reaches almost a factor 2 for 830 m testing while for the longer wavelength of 1312 nm it is slightly less. Unfortunately, the slope of linear part of the curves corresponding to different dose rates do differ up to almost a factor 2 at 830 nm and up to 30% at 1312 nm as can be seen in Fig. 5.9 where the

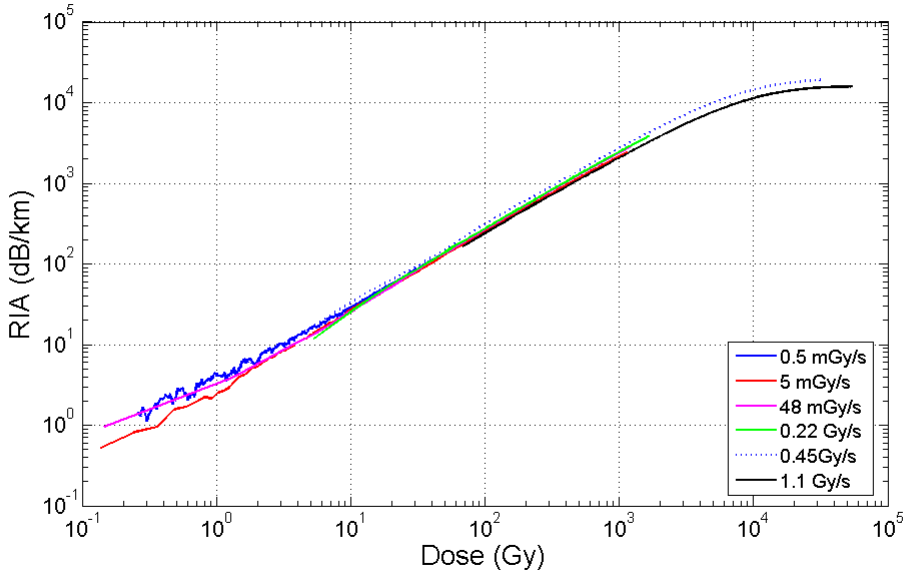

Figure 5.8: RIA as function of absorbed dose for different dose rates at 1312 nm

characterization has been reported in linear scale for a doses up to 1 kGy.

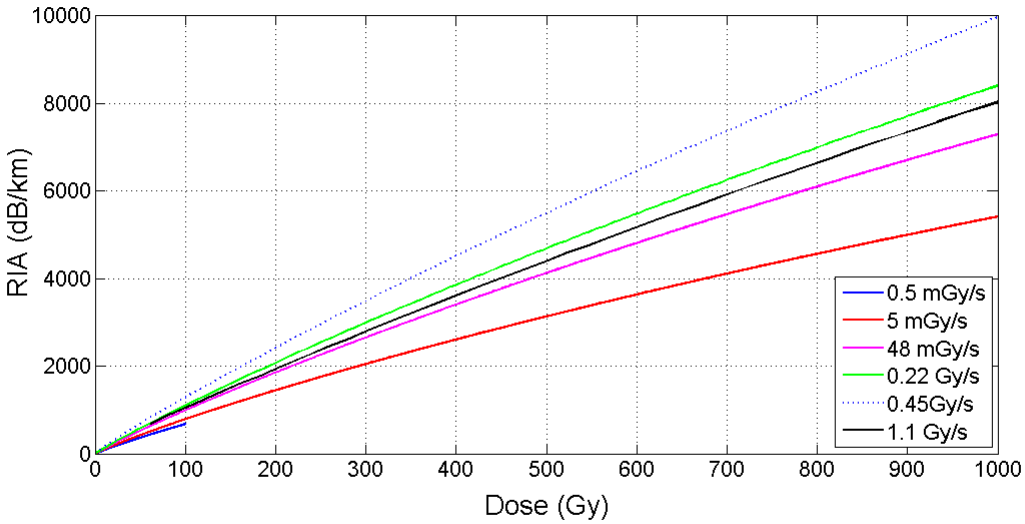

Figure 5.9: RIA as function of absorbed dose up to 1 kGy, linear scale, 830 nm

The sensitivity of the fiber therefore ranges between 5 and almost 9.5 mdB/m/Gy

at 830 nm and between 1.98 and about 2.7 mdB/m/Gy for the 1312 nm wavelength. For this reason, measuring the variation of the RIA isn't be reliable and the OFS fiber can't be considered suitable for radiation sensing.

Finally, spectral measurements have been carried out and the result in terms of the RIA as function of the wavelength after an irradiation of 300 Gy are shown in Fig 5.10. The result is in agreement which was has been reported in literature [97]. In particular, the minimum of the RIA at 1.1 μm due to the absence of any phosphorous or germanium point defect at the corresponding energy of about 1.13 eV can be observed. On the other hand the typical band at near infrared wavelengths with a peak at about 1650 nm consequence of the P1 defect (0.79 eV) is also visible.

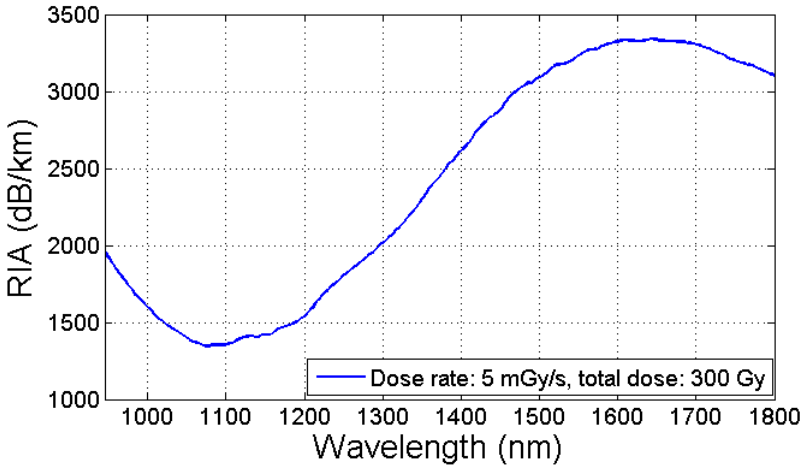

Figure 5.10: Spectral response at 300 Gy

5.2.2 Single mode fibers (SMF) radiation response

SMF Draka

Similarly to the MMF tested in the previous section, a single mode fiber from Draka has been fully characterized in terms of it's RIA as function of the dose for the optical wavelength of 1312 nm and 1570 nm. The result of the irradiations at different dose rates ranging from around 0.5 mGy/s up to about 1.1 Gy/s and reaching up to 55 kGy is shown in Fig. 5.11 and Fig. 5.12.

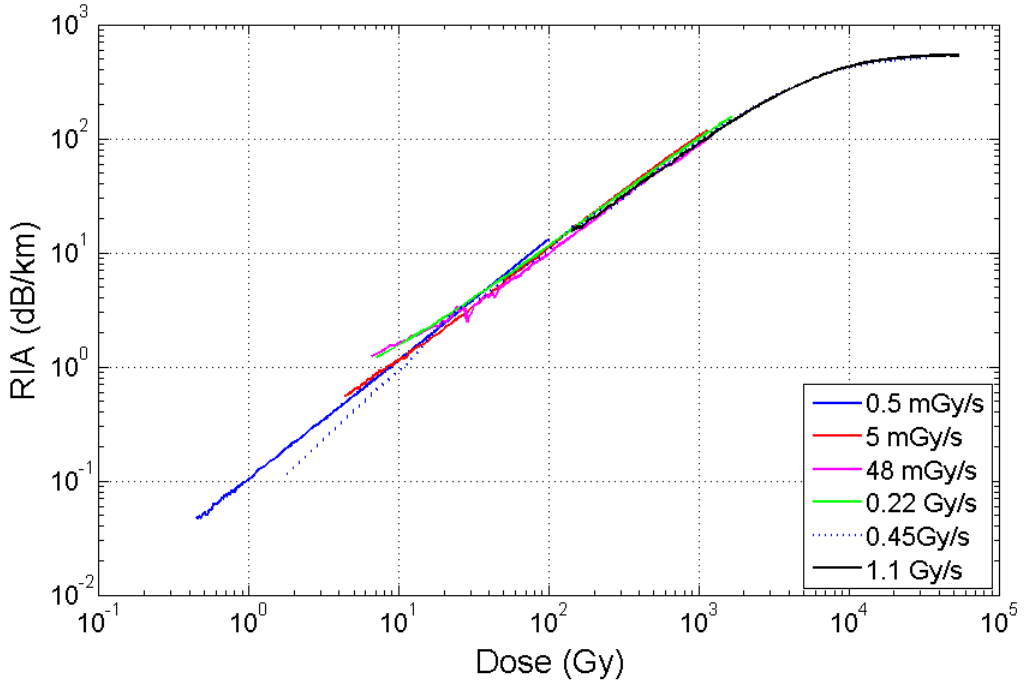

Figure 5.11: RIA as function of total absorbed dose for different dose rates at 1312 nm

The initial fluctuations appreciable on certain curves are due to low statistics and therefore a low signal to noise ration (SNR). As shown in Fig. 5.11 and Fig. 5.12, the response of the fiber's attenuation as function of the accumulated dose is linear up to 1-2 kGy then becomes non-linear and finally saturates around 20 kGy. In particular, at 1312 nm the linear range starts at several Gy and reaches around 1.8 kGy with a 5% tolerance margin while at 1570 nm the linear range spans from a few Gy up to almost 1 kGy with 5% tolerance margin. The maximum dose values reachable in the linear range for different tolerance margins are shown in Table 5.3.

The dose rate dependence observable in Fig. 5.11 and 5.12 is less important than the one observe in the case of the two tested MMF. In fact, at 1 kGy nm only a 20% and 25% variations of the RIA due to the dose rate is observed for 1312 nm and 1570 nm respectively. The linear part of the curves all have the same slope within 10% for the 1312 nm testing and within 15% for the 1570 nm.

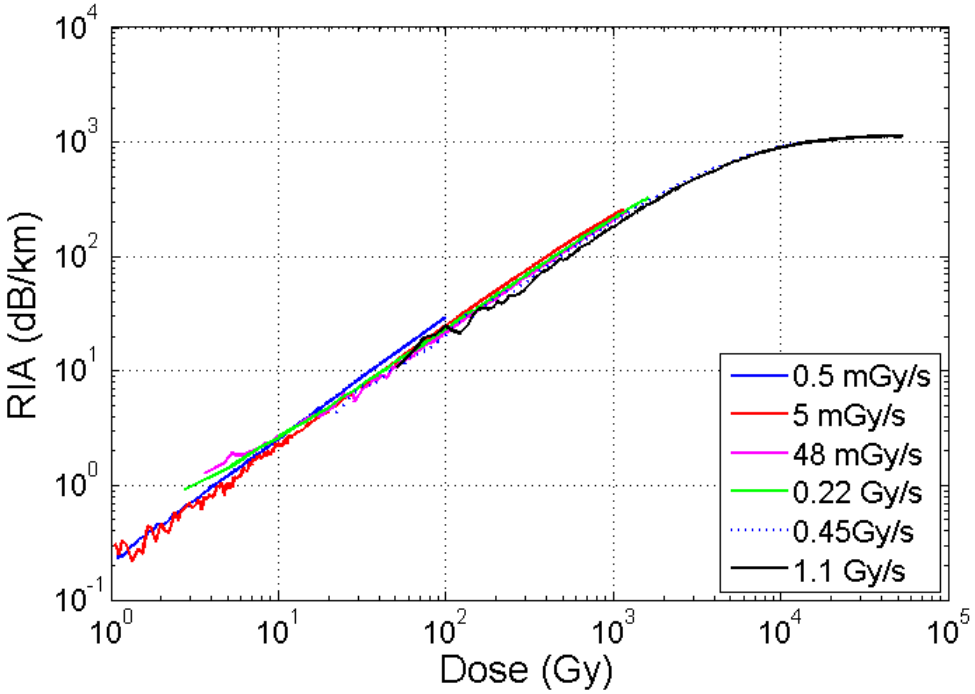

Figure 5.12: RIA as function of total absorbed dose for different dose rates at 1570 nm

Table 5.3: SMF Draka, Maximum total absorbed dose in the linear range for different tolerance values

Tolerance	λ_1 = 1312 nm	λ_2 = 1570 nm
5%	1819 Gy	993 Gy
10%	2275 Gy	1353 Gy
20%	2693 Gy	2167 Gy

Both these values are acceptable for radiation sensing at an accelerator such as the ones present at CERN.

The sensitivity of the fiber is of about 100 $\mu dB/m/Gy$ at 1312 nm and 200 $\mu dB/m/Gy$ at 1570 nm making it less sensitive than both of the multimode fibers characterized and discussed in the previous subsection.

At last, Fig. 5.13 shows an acquired spectrum for an irradiation of 1 kGy at a dose rate of 46.7 mGy/s.

It is worth noticing that while SMF from Draka exhibits a spectral minimum around 1.1 μm typical of P-doped fibers, it doesn't show a maximum around

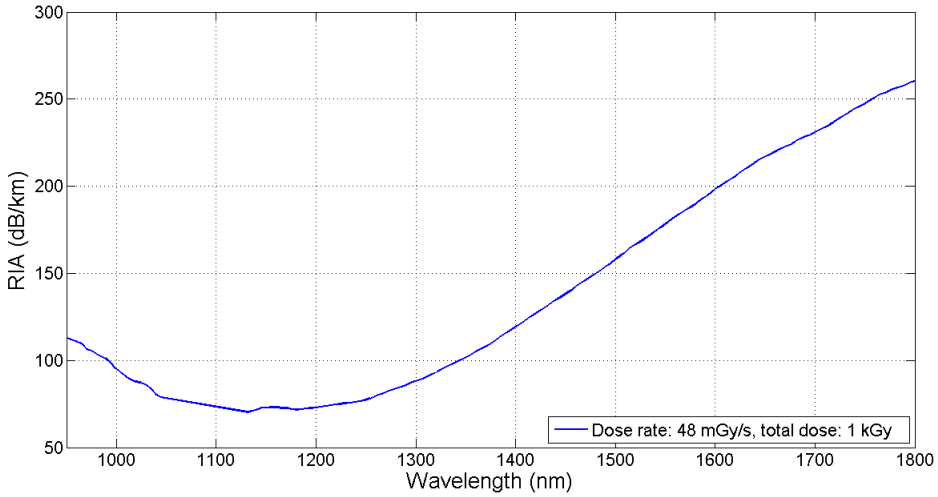

Figure 5.13: Spectral response of the Draka at 1 kGy

1.65 μm which is probably the consequence of the specific composition of the fiber.

SMF X

A second single mode optical fiber has been considered for our application and has been kindly provided by Alexey Faustov from the Belgian Nuclear Research Center (SCK-CEN) in Mol (Belgium) who already characterized the fiber [51]. The fiber, which we will name "fiber X" as the manufacturer doesn't want to be named, has a known phosphorous concentration of 6.5 mol.%. Fiber X has been irradiated for 390000 s at a dose rate of 153 mGy/s up to almost 60 kGy trying to recreate similar test conditions as Faustov had, to make the best possible comparison between the results. Fig. 5.14 and 5.15 show the radiation response of fiber X in terms of RIA as function of the total accumulated dose both at 1312 nm and 1570 nm optical wavelengths in double logarithmic and linear scales respectively.

As can be seen in Fig. 5.14, the linear range of the RIA in double logarithmic scale extends from a few tens of Gy up to around 850 Gy with a 5% tolerance margin on the linearity both at 1312 nm and 1570 nm. Interestingly, fiber X didn't

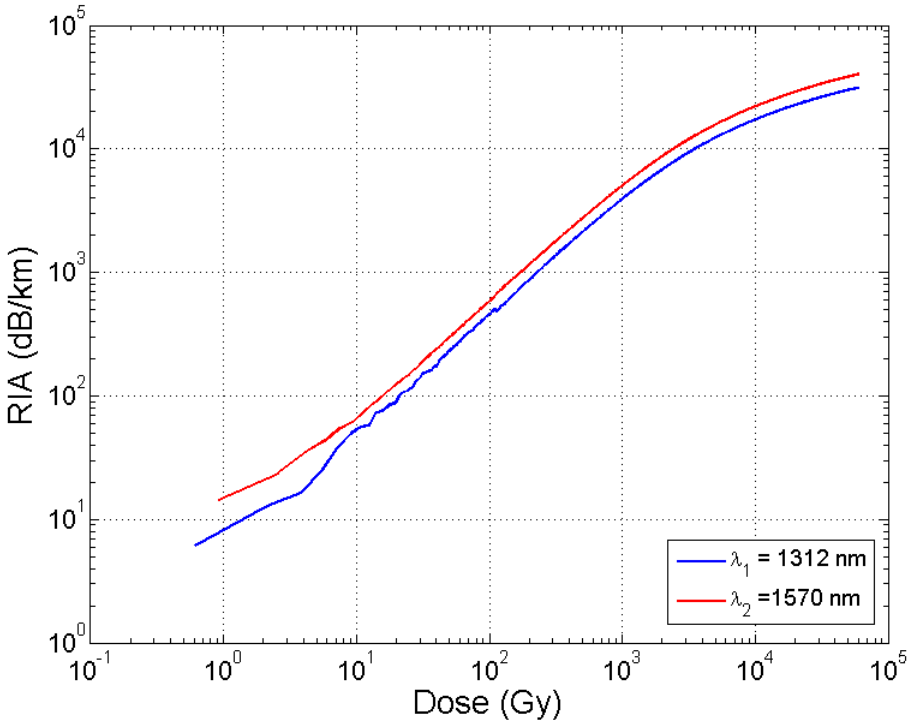

Figure 5.14: Fiber X, double logarithmic: RIA as function of total absorbed dose at 1312 nm and 1570 nm, dose rate: 153 mGy/s

reach saturation at 60 kGy allowing it to be a valid candidate for the monitoring of high doses. In addition, the sensitivity of fiber X is of about 4 mdB/m/Gy at 1312 nm and about 5 mdB/m/Gy at 1570 nm making it more sensitive than the tested SMF from Draka by a factor 40 and 25 respectively, allowing therefore for better sensing capabilities also at lower doses.
Fig. 5.16 shows a spectral acquisition after having accumulated 1 kGy.

The spectrum showed in Fig. 5.16 is in agreement with what has been reported in literature [97]. In particular, the minimum of the RIA at 1.1 μm due to the absence of any phosphorous or germanium point defect at the corresponding energy of about 1.13 eV can be observed. On the other hand the typical band at near-infrared wavelengths with a peak at about 1530 nm consequence of the P1 defect (0.79 eV) introduced in Chapter 3 is also visible.

Our results of the characterization of fiber X are now compared to those obtained by Faustov et al. shown in Fig. 5.17 where fiber X is identified by "F-Ph".

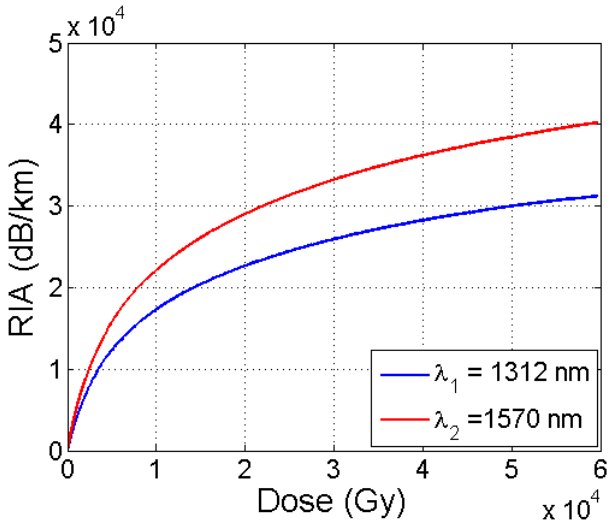

Figure 5.15: Fiber X, linear: RIA as function of total absorbed dose at 1312 nm and 1570 nm, dose rate: 153 mGy/s

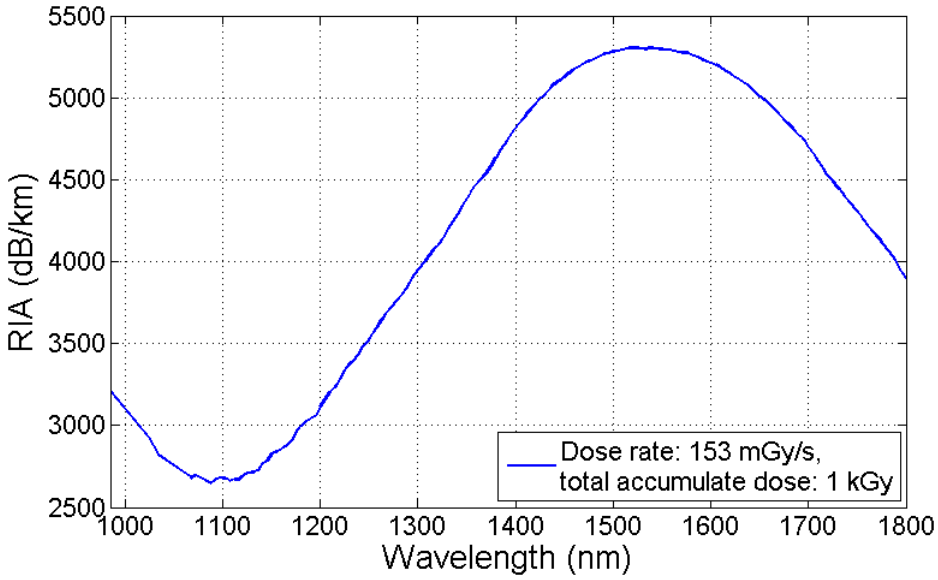

Figure 5.16: Spectral response for fiber X at 1 kGy

What can be observed is an offset in the RIA between the curve we obtained at 1570 nm and the one Faustov et al. obtained at 1550 nm.

For example, at 20 kGy Faustov obtained around 23000 dB/km while we obtained around 29000 dB/km. Around 60 kGy, Faustov measured around 32000 dB/km while we measured 40000 dB/km. It is worth noticing that the optical

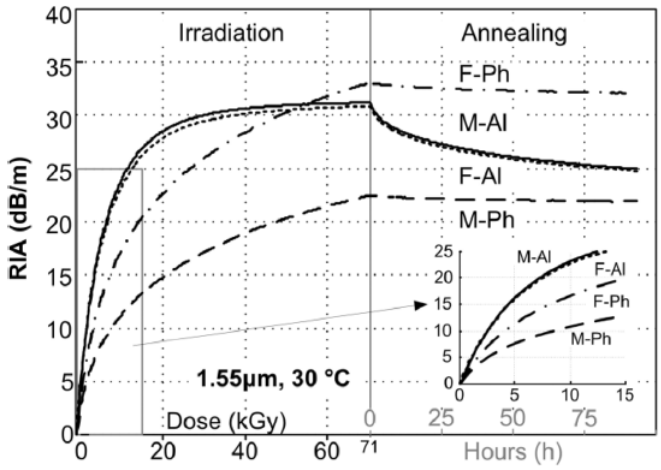

Figure 5.17: RIA as function of absorbed dose in the highly radiation sensitive Al and P codoped fibers at 1550 nm, 30°C

power launched in the fiber was around -19 dBm which is a very similar value to the power used by Faustov. As can be seen in Fig. 5.16, the difference in sensitivity between 1550 nm and 1570 nm is relatively small and in particular 1570 nm is not more sensitive than 1550 nm, given the peak of sensitivity around 1530 nm. In addition, Faustov observed that fiber X shows an increase in radiation sensitivity for increasing temperature, in particular, raising the temperature by 50°C (from 30°C to 80°C) resulted in more than 10% increase of its radiation sensitivity. We performed our measurements with 6°C less compared to Faustov et al but given the above mentioned inverse temperature dependence, the offset cannot be attributed to the temperature difference in the measurement conditions between SCK-CEN and Fraunhofer INT.
A further analysis is provided by the plots shown in Fig. 5.18 where the ratio between Faustov's measurement and ours is depicted and by Fig. 5.19 where the ratio of the spectral acquisitions is reported. For the ratio presented in Fig. 5.19, the spectrum after almost 60 kGy of accumulated dose shown in Fig. 5.20 has been considered, to be as close as possible to the 71 kGy reached by Faustov.

As can be seen from 5.18, the ratio is quite constant around a value of 0.78 above 15-20 kGy while it isn't at the very beginning of irradiation because of the low statistics. The trend of the two curves is therefore very similar meaning that any dose rate dependence between the measurements can be excluded. Fig. 5.19

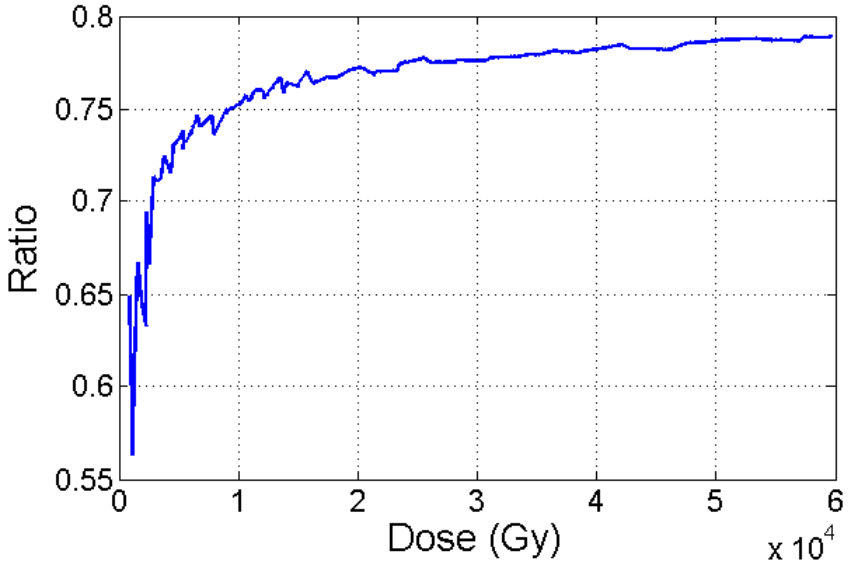

Figure 5.18: Ratio between the attenuation measurements carried out at SCK-CEN and those at Fraunhofer INT

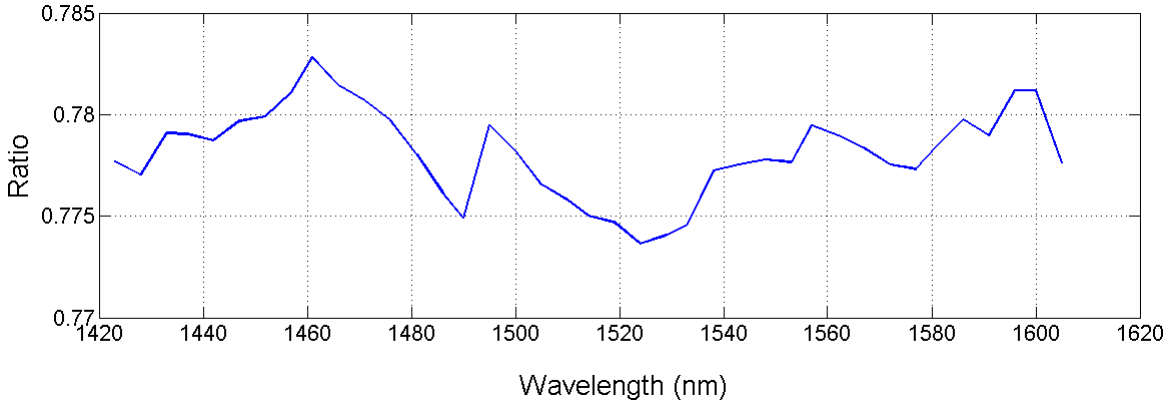

Figure 5.19: Ratio of the spectral measurements carried out at SCK-CEN and those at Fraunhofer INT

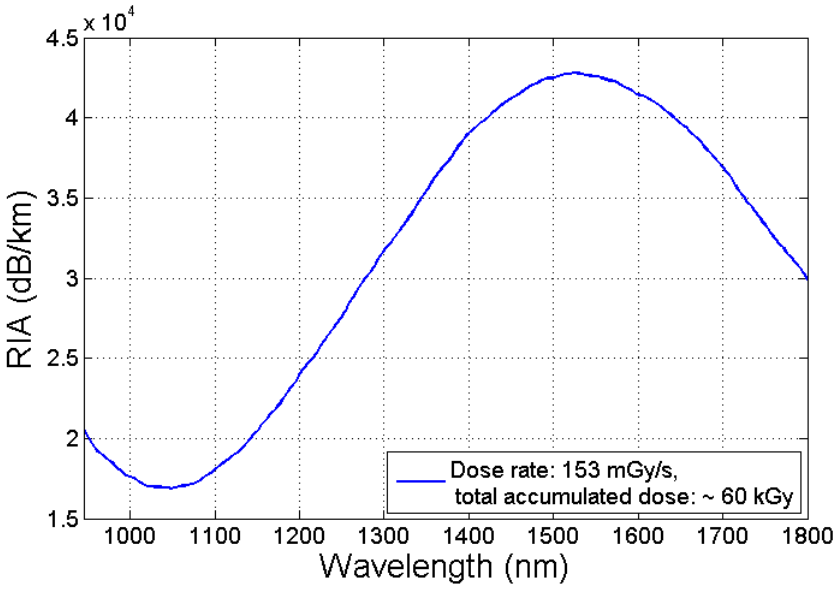

Figure 5.20: Spectral response at almost 60 kGy

depicting the ratio of the spectral measurements also shows a nice match resulting in a quite constant value of the ratio especially between 1430-1630 nm. This indicates that the offset we observe in the RIA shouldn't be attributed to the wavelength or any of the wavelength dependent effects such as having a too tight bending radius of the spools.
In conclusion, having excluded several possible explanations for the observed offset, the most plausible reason for this has to be attributed to a discrepancy in the irradiated sample length measurement between our two laboratories. In fact, as the RIA has been normalized over the sample length which was of only 0.1 m, even a small uncertainty on the length measurement may have considerably affected the RIA. In addition to this, 5%-10% uncertainty on the dosimetry has to be considered. With these considerations in mind, the characterization of fiber X carried out at Fraunhofer INT matches well the one done by Faustov et al. at SCK-CEN.

5.3 Distributed measurements

The goal of distributed optical fiber radiation measurement is to localize induced losses and to correlate them to the actual total dose accumulated in the fiber.

Such measurements are carried out by means of an OTDR allowing to measure the backscattered light intensity as function of the distance in a fiber and localize losses as previously explained in Chapter 4. The fiber used for these measurements is the multimode one from j-Fiber and the dose will be estimated based on the fiber's characterization presented in the previous section.

5.3.1 Experimental setup

The experimental setup for the distributed measurement mainly consists in the OTDR MTS6000 by JDSU to which a radiation hard multimode lead fiber of about 80 m is connected. A sample from the multimode J-fiber is then spliced at the end of the lead fiber and by means of three different spools, two shielded and one exposed to radiation, it is possible to wind up and place the fiber in such away that it is irradiated in different consecutive parts even though we only have a single source as shown in Fig. 5.21. Overall, four parts of the fiber are irradiated with respective lengths of about 40 cm, 72 cm, 128 cm and 240 cm as schematically shown in Fig. 5.22 where we imagine the fiber deployed instead of wounded on spool for the sake of clarity.

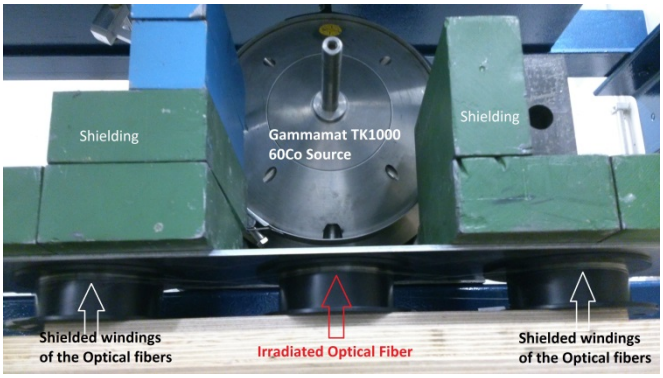

Figure 5.21: Experimental setup for the distributed measurements on a fiber under ^{60}Co irradiation

The OTDR measurements are carried out at two different wavelengths, λ_1 = 850 nm and λ_2 = 1300 nm, while the pulse width used to interrogate the fiber is the shortest available on the MTS600 and is equal to 3 ns, corresponding to a theoretical spatial resolution of 30 cm. The idea behind the use of multiple wavelength for the fiber's investigation is that if the wavelengths are sufficiently

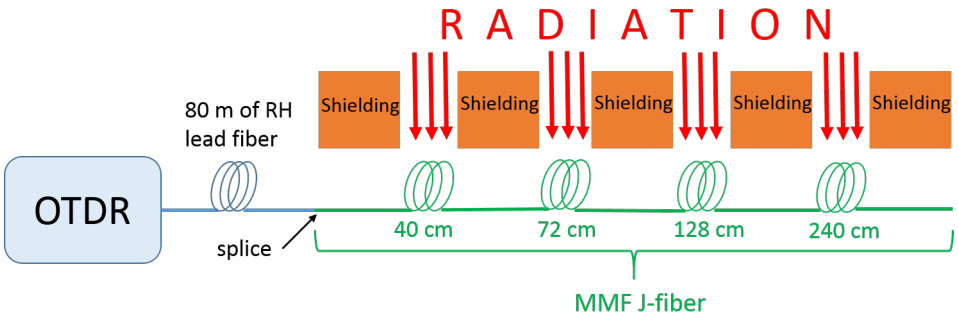

Figure 5.22: Schematic layout of the fiber's irradiation for distributed measurements

spectrally separated they will have different sensitivities with respect to dose when propagating in P-codoped fibers. If this is the case, like for λ_1 and λ_2, it is then possible to get rid of systematics and make the sensing system more robust by taking the ratio between the measurement at each wavelength. In addition, the choice of the wavelength is generally dictated by which OTDR transmitter modules are available on the market.

5.3.2 Results

The four parts of the fiber under test depicted in Fig. 5.22 have been irradiated at 23 mGy/s for 13800 s up to a little more than 300 Gy. The zoom of the OTDR traces of the region of interest for both λ_1 = 850 nm and λ_2 = 1300 nm are shown in Fig. 5.23 and Fig. 5.24. In both figures, the irradiated and shielded parts of the fiber are clearly visible. There is however a mismatch between the measured length of the irradiated parts and the prepared sample lengths which can be due to the limited spatial resolution for the first two parts (40 cm and 72 cm) as well as to the noise present in the traces which does not allow to accurately estimate these lengths. The uncertainty on the measured irradiate samples length which ranges from 5% up to 20% will unavoidably directly affect the RIA calculation and consequently the dose estimation.

By estimating the slopes of the steps corresponding to the irradiated parts of the fiber through linear fits, it is possible to calculated the RIA in those sections. We focus our attention on the two last irradiated sections as these hold a lower uncertainty on the length. For the measurement at 850 nm the RIA is found

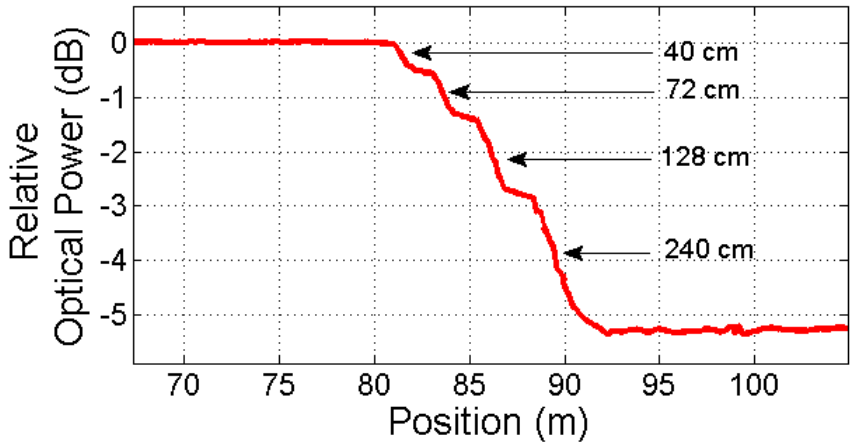

Figure 5.23: Zoom of OTDR trace at λ_1 = 850 for a total absorbed dose of about 300 Gy

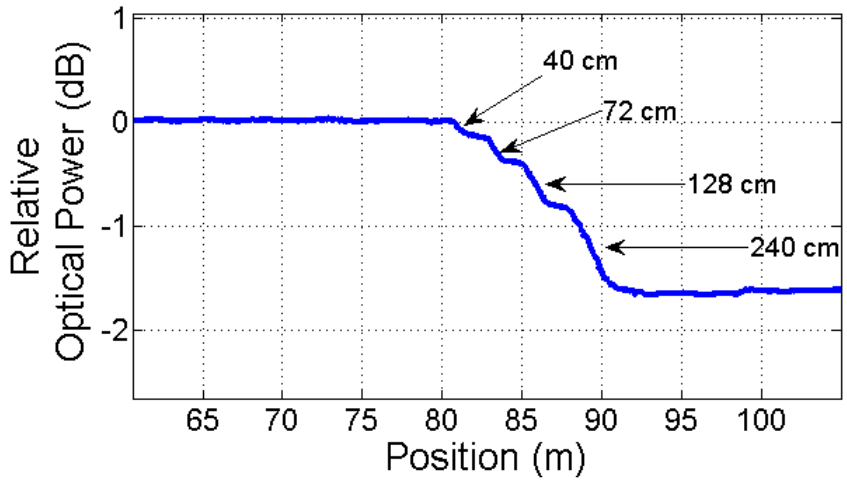

Figure 5.24: Zoom of OTDR trace at λ_2 = 1300 fora total absorbed dose of about 300 Gy

to range between 0.8 dB/m and 1 dB/m which based on the results from the characterization presented in the previous section, corresponds to a total absorbed dose of around 200 Gy. The expected RIA corresponding to the 300 Gy of exposure would be 1.3 dB/m resulting therefore in an uncertainty of about 33% in our measurement. At 1300 nm and based on the characterization curve showed in Fig. 5.5, the expected RIA would be 0.3 dB/m while we calculated a RIA around 0.25 dB/m and corresponding 270 Gy resulting in a 10% uncertainty.
Considering that the uncertainty on the dose rate estimation is of about 10%, the obtained results are promising for further investigations of distributed optical fiber radiation monitoring.

5.4 Limitations of commercially available P-codoped fibers

The characterizations presented in Section 5.2 provide a hint on the difficulty to find a suitable optical fiber candidate for radiation sensing in accelerator tunnels given its requirements detailed in Chapter 3. In fact, almost all the fibers under test saturated at around 20 kGy not allowing to correctly estimate doses above that value. In double logarithmic scale, most of the fibers presented a linear relation between the RIA and the deposited dose up to a couple of kGy which is quite restrictive although sufficient to monitor low dose areas such as some segments of the LHC where annual doses do not reach more than 200 Gy. The measurable dose variation range can also be extended by using the non-linear range of the fibers' response curve taking into account higher uncertainties. This could be achieved by using different fitting models as for example the first-order kinetic model. The dose rate dependence observed on all fibers was acceptable given that our main interest is to measure dose variations rather than absolute dose values. The measurement approach we have proposed to achieve this if the slopes of the linear part of the curve corresponding to different dose rates have the same magnitude within a 20% tolerance. This was the case for both the j-fiber MM and the Draka SMF but not for the OFS MM which showed strong variations in its sensitivity at different dose rates.
Among the tested fibers, the most promising one is fiber X which showed a high

sensitivity to dose allowing to measure low doses and didn't saturate yet at 60 kGy allowing for high dose measurement although not having a linear response at that point anymore. Unfortunately, fiber X has been developed by its manufacturer for research purposes and is not commercially available.
The main difficulty in choosing a commercially available P-codoped fiber comes from the fact that manufacturers do not disclaim the exact composition of the fiber preventing from making the right choice or a pre-selection in the first place.

5.4.1 Radiation sensitive optical fiber custom design

Given the difficulty to select a commercial optical fiber suitable for radiation sensing applications, it is advisable to look for an opportunity to customize the composition and the design of a fiber in collaboration with some manufacturer to obtain the desired and optical response for the specific application. This is kind of scientific collaboration has been established between Prof. Sylvain Girard and his group at the Laboratoire Hubert Curien of the UniversitÃ© Jean Monnet Saint-Etienne and the Photonics Division of the ixBlue company situated in Lannion (France). As a result of this collaboration several optical fibers potentially highly interesting for radiation sensing have been jointly developed. CERN and the University Jean Monnet Saint-Etienne are currently establishing a collaboration agreement which will facilitate the scientific exchange of the two parties, allowing for example to test in the near future the above mentioned fibers in some of the irradiation facilities present at CERN.
Following, the main characteristics of two different types of optical fibers jointly developed by Prof. Girard, his team and ixBlue Photonics Division, are briefly summarized.

Hole-Assisted optical fibers (HAOF)

With reference to [98], the first type of fiber which could be used for radiation sensing is the so-called Hole-Assisted optical fiber (HAOF). The idea in using such fibers is that a longitudinal gas-loading is easy to perform thanks to the fibers' dedicated holes located in the outer part of the cladding and shown in Fig. 5.25. As a consequence, gas (H_2 or D_2) diffuses from the holes into the silica matrix,

interacts with radiation induced point defects and passivates them, reducing the RIA levels all along the fiber length. HAOF may be realized with a great variety of core dopants as Ge, P or F among others. Fig.5.25 shows a scanning electron microscope picture of a Hole-Assisted Carbon Coating Ge core doped fiber (HACC-Ge). The fiber's core diameter is of 10 μm while the whole fiber's diameter is of 125 μm. In specific case of this HACC-Ge fiber, six holes of large size and four smaller holes are present in the outer part of the fiber cladding where no light propagates.

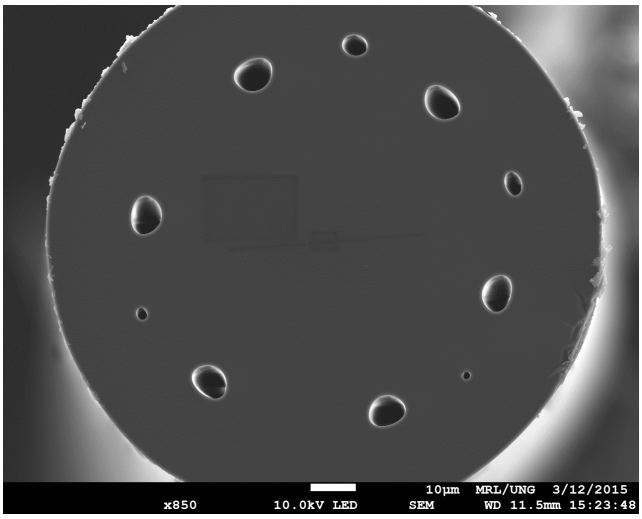

Figure 5.25: Scanning Electron Microscope picture of the HACC-Ge fiber [98]

It is worth knowing that the holes location and form should not have any effects on the fiber's optical properties. The main goal of the fiber is simply to allow the longitudinal gas diffusion from one fiber end along the whole fiber and then into the fiber core and cladding. Interestingly this method.
While the full description of the gas loading technique can be found in [98], it can be summarized by knowing that only one end of the fiber needs to be accessible for the loading and the successive regeneration of the fiber to occur. In fact, once the fiber end is put into a gas tank containing H_2 or D_2 under pressure (typically ¿100 bars), the gas starts to diffuse longitudinally along the whole fiber length through its wholes. The process is very fast and the efficiency of this kinetic is therefore almost independent from the fiber's length. In the case of an HAOF-Ge irradiated up to 10 MGy, it has been shown that after only a few hours of regeneration, a reduction of 50% in the RIA at 1550 nm could be obtained [98] acting only from

one of the two ends of the fiber.

For radiation sensing, HAOF-P-doped fibers could be particularly interesting. Fig.5.26 shows the spectral dependence of the RIA after an 1.2 kGy γ–ray irradiation of an HAOF-P-doped MMF.

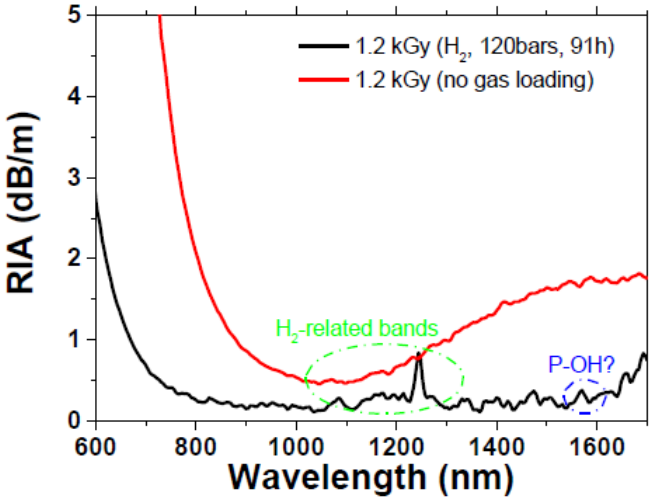

Figure 5.26: Scanning Electron Microscope picture of the HACC-Ge fiber [98]

The results shown in Fig. 5.26, provide a clear evidence of the H_2 laoding effect in eliminating both the RIA related to P1 centers and their absoprtion band around 1600 nm as well as the long tail of the RIA below 600 nm associated to POHC.

The presented treatment procedure is therefore highly interesting for radiation sensing applications given the possibility to regenerate an irradiated fiber link without the need of removing and replacing it, having in addition the option to access it only from one of its two output ends. The use of HAOF as sensing element, could ensure the long life of a HAOF-based radiation sensing system. For this reason, it is planned to test Hole-Assisted optical fibers in irradiation facilities at CERN.

Phosphorus-Cerium-co-doped fibers

The second type of fiber which could find some application in radiation sensing is a MM phosphorous (P) and cerium (Ce) codoped (PCe-codoped) core fiber

with a pure Si cladding. Fig. 5.27 shows the RIA spectrum of the PCe-codoped fiber compared to a P-doped fiber (named PD1) [99].

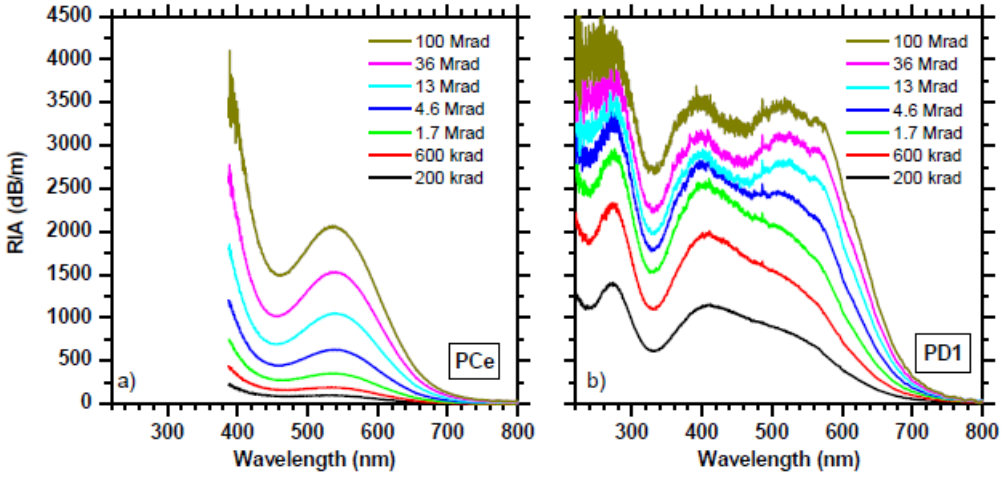

Figure 5.27: RIA spectra evolution of the PCe a) and the P-doped b) optical fibers irradiated at room temperature with a dose rate of 5 krad/s up to a a dose of 100 Mrad [99]

What can be observed is that the presence of the cerium co-dopant causes the pristine fiber to have a very high optical absorption in the UV domain. The Ce-codoping drastically impacts the response of the optical fiber in the investigated visible region. What is particularly interesting is that at all doses PCe shows a lower RIA with respect to undoped fiber. This is confirmed when looking at Fig. 5.28 where the RIA is reported as function of the dose for both fibers for a launched optical wavelength of 500nm.

As can be observed in Fig. 5.28 both fibers reveal to be very sensitive to radiation in the visible domain. However, at low doses the RIA in the PCe is much lower than in the PD1. It can also be observed that for doses higher than 10 kGy the PD1's response to dose start to slow down, almost reaching a saturation level, while the PCe's one doesn't show any sign of saturation up to the MGy. This result suggests a positive effect of Ce codoping to reduce the induced attenuation during irradiation of fibers doped with P in the visible spectral range.
The study concerning Ce-codoping carried out at the University of Saint-Etienne therefore suggests that a PCe- doped OF could also be a valuable candidate for radiation sensing applications. In fact, it has bee shown that in the visible light range, the PCe OF is sensitive enough to radiation as well as the PD1 under

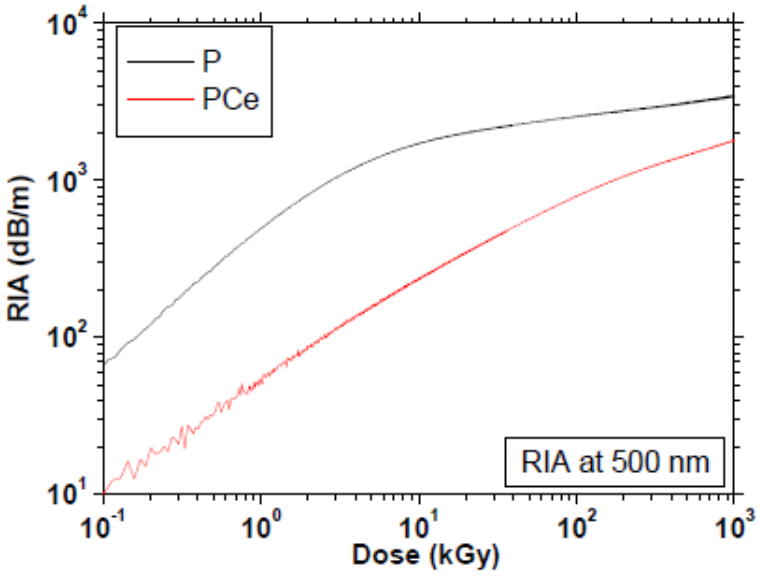

Figure 5.28: RIA as function of the dose for the PCe optical fiber and a P-codoped optical fiber both irradiated at room temperature with a dose rate of 50 Gy/s up to a a dose of 1 MGy, λ = 500nm (adapted from [100])

investigation but without the saturation tendency the PD1 showed. whereas a P-doped OF does. Further investigation, possibly in collaboration with CERN will determine the PCe optical fiber's behavior at IR wavelengths as well as any dose rate dependence.

6 Distributed OTDR based radiation sensing at CHARM

6.1 Cern High energy AcceleRator Mixed field facility (CHARM)

A new mixed field irradiation facility called CHARM has recently been constructed at CERN and is now in full operation. A 24 GeV/c proton beam extracted from the Proton Synchrotron (PS) is focused on a cylindrical aluminum or copper target generating a mixed radiation field composed of protons, neutrons, pions, photons, muons and other particles. This unique facility, schematically shown in Fig. 6.1 a)[101],provides a variety of particle energy spectra which can be representative of several radiation environments and allowing large acceleration factors up to around 10^9. It can be used to test electronics, optics and photonics equipment to be installed within particle accelerators, and also to test devices and systems to be used for space, atmospheric and ground level applications.
The choice of the target among two massive ones made of aluminum or copper and one with reduced effective density, allows to modulate the intensity of the radiation field with adjustments in the intensity over an order of magnitude. An additional way of modulating the radiation field is provided by four mobile shielding plates of 40 cm of width each, two made of concrete and two made of iron, which can be placed between the target and a set of predefined test positions where the components under test will be placed as shown in Fig.6.1 b)[101]. The desired shielding and target configuration can be remotely controlled according to the needs in terms of particle spectra and intensity [101].

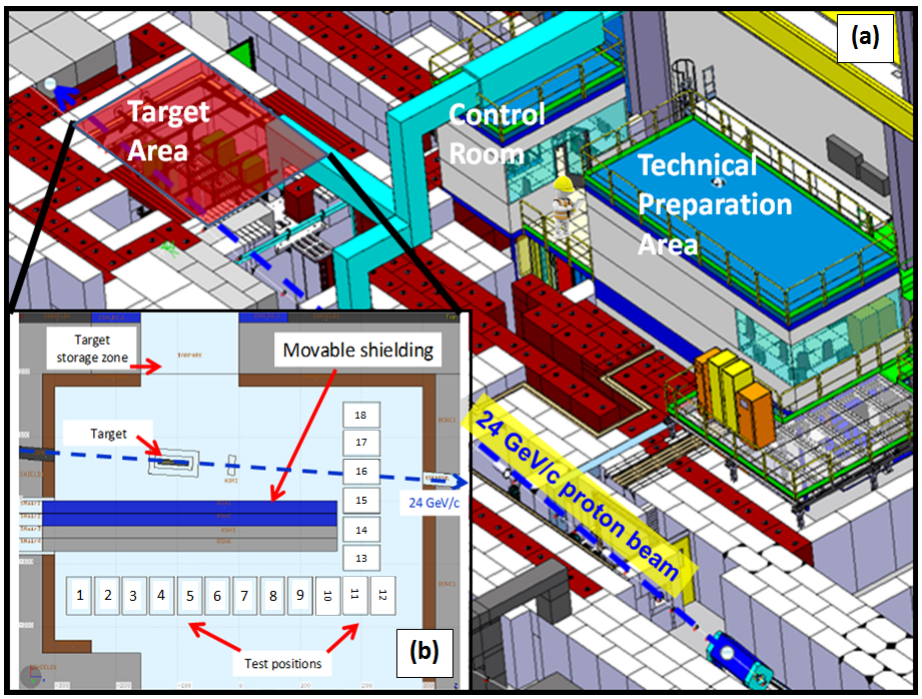

Figure 6.1: (a) 3D view of the facility, (b) FLUKA geometry for the target area: Racks 1 to 18 are the regions representing the test positions. The blue and grey plates are the iron and concrete movable shieldings [101]

6.1.1 The mixed-field radiation environment

As explained in the first Chapter of this thesis, the complex mixed particle field present within CERN's accelerators, is composed of charged and neutral hadrons, electrons, muons and photons ranging from GeVs down to thermal energies. The CHARM test facility is able to replicate such an environment and Monte-Carlo simulations have been performed using the FLUKA code in order to extract the particle energy spectra at different test locations [101] as well as to calculate the total ionizing dose in the whole facility . In particular, Fig. 6.2 and Fig. 6.3 from [101], show the HEH flux (cm^{-2}/h) (introduced in Chapter 1) available in different test locations within the CHARM facility for different target and shielding configurations respectively.

The HEH flux per hour reported in Fig. 6.2 illustrates how it is possible to reduce the intensity by using a different target almost without altering the energy spectra shape.

Table 6.1 compares the hardness factors (H0.1 and H0.01) for the accelerator and

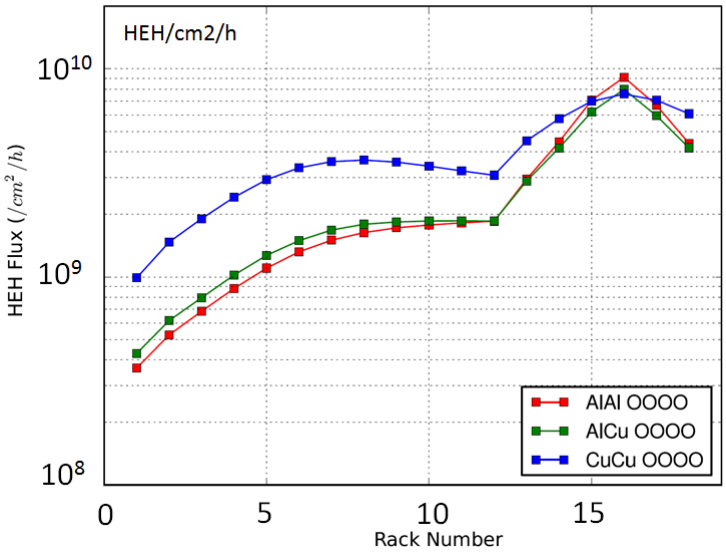

Figure 6.2: HEH flux (cm^{-2}/h) at different locations for the three different target configurations [101]

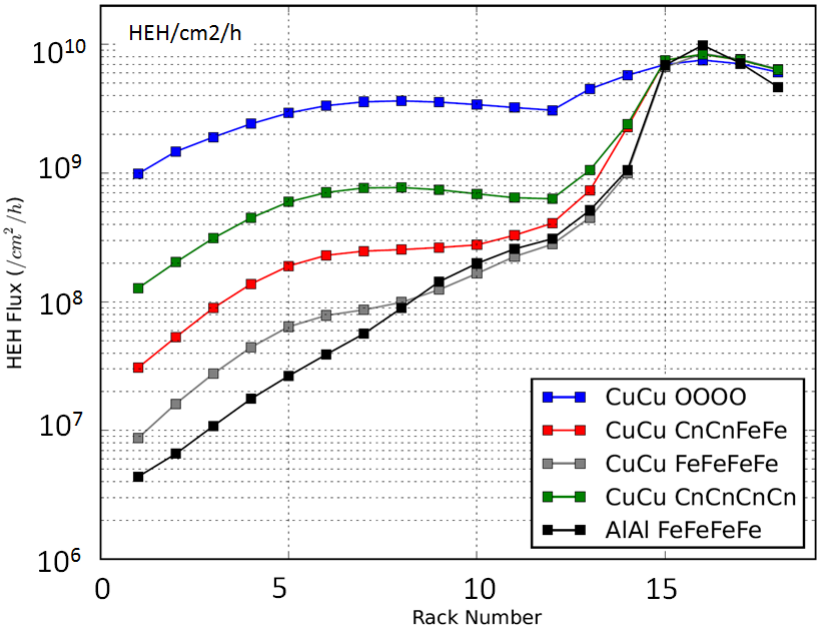

Figure 6.3: HEH flux (cm^{-2}/h) at different locations for the different shielding configurations [101]

test facility configurations in order to understand which could be the suitable CHARM location for the experimental reproduction of the spectra. H0.1 and H0.01 are respectively representing the HEH energy values for which the flux is corresponding to 10% and 1% of the total and the considered fluences are for energy values above the ones indicated.

Table 6.1: Comparison of the HEH hardness factor between the LHC and CHARM

Location in LHC/CHARM	H0.1 (MeV)	H0.01 (MeV)
UJ/(CuCu/CnCnFeFe/4)	180/(185)	360/(350)
RR/(CuCu/CnCnFeFe/14	690/(970)	2800/(2700)
Tunnel/(CuCu/CnCnFeFe/15	1700/(2400)	5700/(5200)

The LHC location UJ and RR stand for highly shielded and moderately shielded areas respectively. The location and configuration in CHARM are identified as (Target/shielding/position) in Table 6.1. The copper target in CHARM is labelled CuCu, while the shielding configuration CnCnFeFe means that two concrete shieldings and two iron shieldings are being used. As can be seen from Table 6.1, there is a good agreement between the LHC environment and the available test spectra.

Finally, given that the facility has been operated for 2 months at the end of 2014 and already for more than 4 months in 2015 it has been possible to carry out a detailed benchmarking campaign between the measurements performed with the RadMON system [9] and the FLUKA calculations. The results of the measurement of the total ionizing dose for a selection of test positions when the copper target was used and no shielding was placed inside, show a factor 2 between the RadMON system and the FLUKA measurements. Given this result has been confirmed by the benchmark with other detectors such as Beam Loss Monitors (BLM), short circuited RadFETs or RPL dosimeters present in the facility, it seems that FLUKA overestimates the dose by a factor 2 [101]. This might be at least partially due to the fact that FLUKA scores dose in air while the detectors measure dose in silicon or silica. The calculation of a conversion factor between air and silicon or silica in a complex mixed particle field such as the one present at CHARM isn't trivial and requires a thorough study which is currently being done. To estimate the accuracy of the distributed optical fiber measurements presented

in the next section, we will therefore consider an underestimation by factor 2 with respect to FLUKA as being a good result.

6.2 Experimental setup

For the distributed radiation sensing measurements at CHARM, three optical fibers already characterized at Fraunhofer INT and presented in Chapter 5 have been used. In particular, the MMF j-fiber and the Draka SMF which we found to be suitable for radiation sensing have been installed following a 130 m long path throughout the facility as depicted in Fig. 6.4. In addition, for completeness the MMF OFS which we found to be not suitable for radiation sensing because of the strong dose rate dependence, has also been installed along the same path to verify its unsuitability for estimating the dose profile. To allow an external company to blow the fiber along the chosen path, the fibers have first been inserted together in one same cable. The blowing of the cable occurs then into a tube which has been pre-installed in the facility and is visible running at two different heights in Fig. 6.5. In particular, the fiber path runs at 2.80 m above the ground back and forth except around the shielding where in one direction it runs at 0.95 m above the ground which is about the same height of the target. This allows to reach the highest possible dose rate when passing close to the target and also ensure a great variety of dose rates.

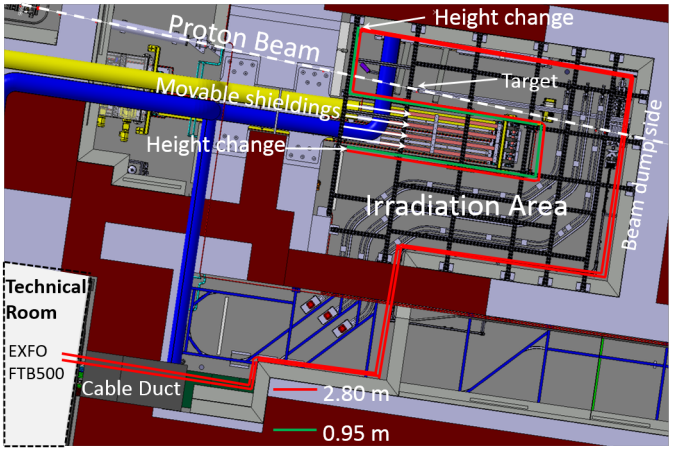

Figure 6.4: Fiber layout for distributed radiation sensing at CHARM

For a better understanding of the fibers' deployment, Fig. 6.5 shows a photo-

graph of the point where the fiber path along the tube (in black) changes height near the shieldings.

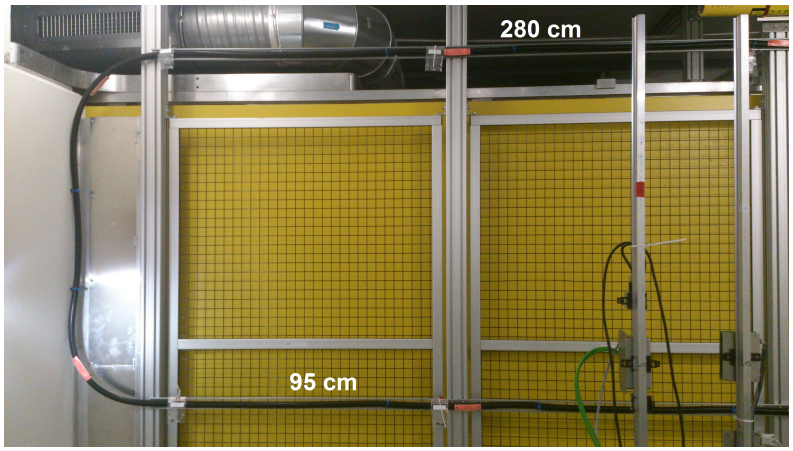

Figure 6.5: Fiber layout for distributed radiation sensing at CHARM

It is worth noting that it is possible to interrogate the fibers from both sides (both directions) given that the fiber itself runs over a loop in the facility and both ends of the fiber reach the technical room where the OTDR is located. This way, if the dynamic range of the OTDR is not sufficient to obtain a good SNR after some major losses occur, for example when the fiber passes near the target, by combining the traces in both directions it is still possible to retrieve a full trace allowing then to compute the dose profile along the whole path.
The OTDR chosen for the distributed measurements was the EXFO FTB 500 able to operate at 850 nm and 1300 nm on MMF by using the multimode module FTB-7200D offering respectively 27 dB and 26 dB of dynamic range and at 1310 nm and 1550 nm on SMF by using the singlemode module FTB-7500E offering respectively 45 dB and 43 dB of dynamic range. It is worth knowing that the dynamic range declared in the specifications refer to $20\mu s$ pulse width, meaning that for pulses of shorter duration it will be smaller. The EXFO modules FTB-7200D and FTB-7500E allow to send pulses with duration ranging from 5 ns up to 20 μs. As detailed in Chapter 4, this corresponds to spatial resolutions ranging from 50 cm up to 2000 m. The acquisition time over which the OTDR can perform averages to improve the SNR, ranges between 30 s and 180 s on the two FTB modules. In many of the real case scenarios, when the annual doses are below 20 kGy (around 55 Gy/day), a single measurement per day would be

sufficient to monitor these slow variations of the dose. In such cases, acquisition times in the order of several hours would be ideal to ensure the highest possible SNR. In the case of annual doses of about 100 kGy (3 mGy/s), the measurements could be carried out more frequently but still over 3-4 hours. The dose resolution which can be obtained with the fiber radiation sensing system will be discussed later, but it can already be said that the measurement time should be sufficiently long to allow for a dose variation equal or bigger than the dose resolution.

6.3 Distributed radiation measurements results

6.3.1 Pulse duration: 5 ns

The first results presented concern irradiations carried out when the proton beam was impinging on the Aluminum target over a maximum duration of 35 hours. In this case none of the movable shieldings was inserted in the facility. The measurements have been carried at the two available wavelengths described in the previous section both for MM fiber and for the SM fiber. The pulse duration was set to the minimum of 5 ns, while the acquisition time was 180 s. The distance between the samples or sampling resolution is about 4 cm for a total number of about 3250 data samples.

j-fiber MMF

Fig. 6.6 reports the time evolution of the OTDR trace for the multimode fiber from j-fiber. Traces, before the start of irradiation at t_0, after 2 hours, after 19 hours and 35 hours of irradiation are reported. The degradation of the fiber is clearly visible, in particular an important loss can be observed at around 72 m where the fiber passes close to the target.

As can be also observed in Fig. 6.6, the traces are affected by some noise which is of course more dominant after each of the losses given that the signal's intensity decreases and leads to a lower SNR. To improve the SNR, longer duration pulses should be preferred as detailed in Chapter 4, more about this will be discussed when the acquisition with 10 ns pulse duration will be presented. Another way to improve the SNR is to smooth the data to produce slow changes in value so that

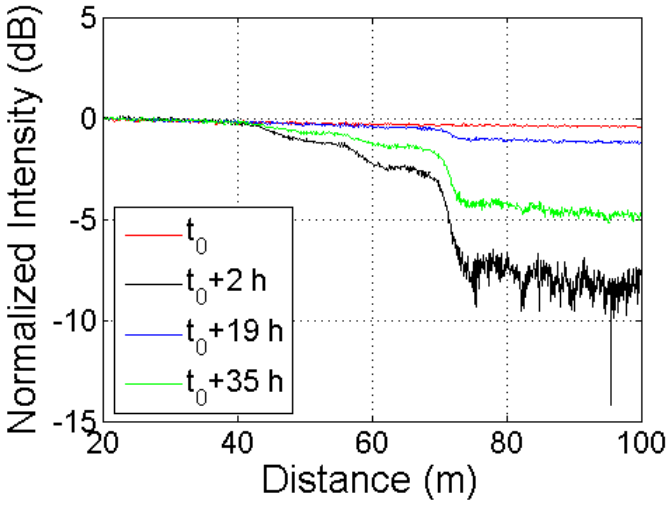

Figure 6.6: j-fiber, OTDR traces at different moments in time

it is easier to appreciate trends in the data. We have chosen to smooth the data by applying a Savitzky-Golay filter to the OTDR traces. Such weighted moving average filter attempts to fit a polynomial of a specified order over a specified number of data samples in a least-squares sense. It often tracks the signal better than more conventional moving averages which tend to clip the extreme values of a given data set. Fig. 6.7 shows the result of Savitzky-Golay filtering applied to the j-fiber's OTDR trace after 35 hours of irradiation. In this case, it has been found that the best filtering occurred for a polynomial degree was 5 over 101 samples windows.

As can be observed, especially in the insert of Fig. 6.7, the filtered trace smoothes well the original data without major information losses. It is however to be noted that once the dynamic range of the OTDR is not sufficient anymore, as is the case at around 75 after the major loss, the trace becomes too noisy and the filtering is not sufficient to retrieve the real trend of the trace. For this reason, the ability to interrogate the fiber from both of its ends is very useful in such cases. Fig. 6.8 and Fig. 6.9 show the OTDR trace at the end of irradiation in one direction of interrogation (called direction 1) and the other (direction 2) respectively. The major loss events have been correlated and labelled with reference to the fiber layout presented in Fig. 6.4. In particular, the fiber situated at 95 cm from the ground passes close to the target at about 72 m along direction 1 and at about 58 m along direction 2. It is interesting to see how along direction 1 it is

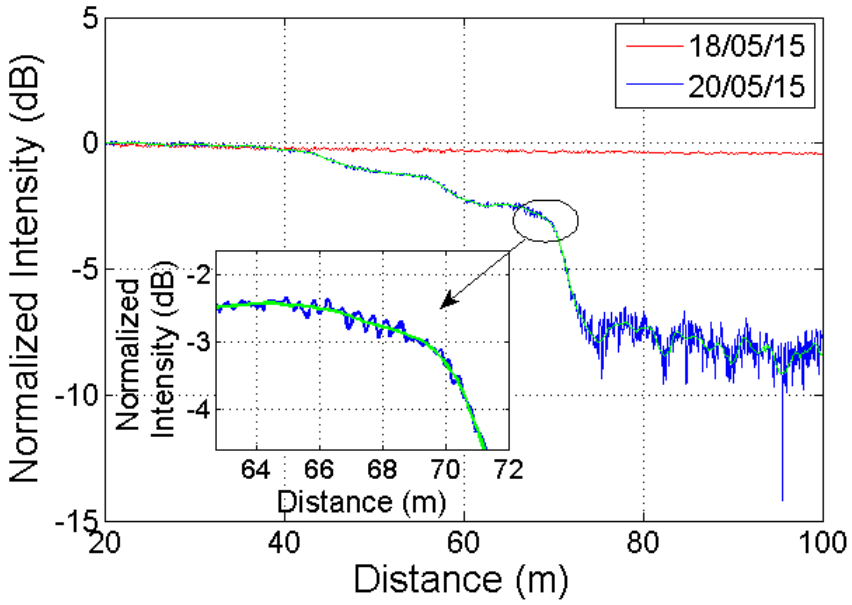

Figure 6.7: Savitzky-Golay filtering effect on j-fiber's OTDR trace

possible to appreciate the loss induced when the fiber situated at 2.80 m from the ground passes along the target (at about 58 m) while it isn't the case along direction 2 because the fiber first passes the target at a height of 95 cm suffering from a higher induced loss after which the SNR is not high enough to detect further events. Finally, it should be noted that the first 20-30 meters of the fiber are not reported in the figures as affected by strong reflection from the connectors and were of no use because of the dead zone of the receiver. These segments however were almost not affected by radiation as they represent the path from the rack in the technical room to reach the irradiation area through the cable duct as shown in Fig. 6.4.

Once the trace has been acquired in both directions, it is possible to differentiate it with respect to the spatial resolution to obtain the attenuation profile as function of the distance. In particular, a moving differentiation with respect to the spatial resolution and with a moving step equal to the sampling resolution is performed. The radiation induced attenuation profile in then obtained by subtracting the attenuation profile before the start of irradiation which is however negligible with respect to the attenuation induced by the irradiation. Once the RIA is obtained as function of the distance and remembering the relationship between the RIA and the dose valid in the linear range, $RIA = C * D$ (where C is the calibration

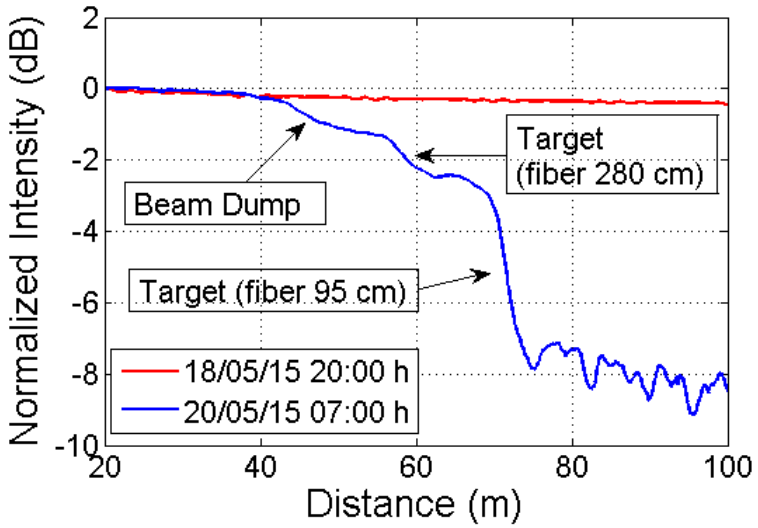

Figure 6.8: j-fiber OTDR trace, direction 1

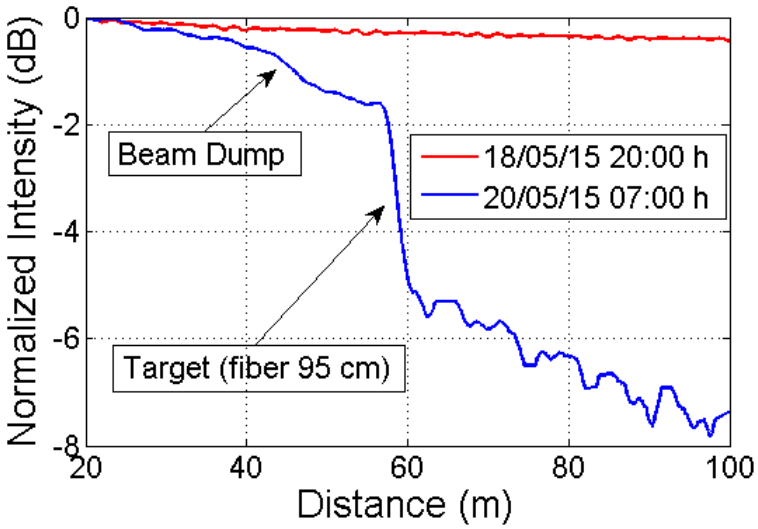

Figure 6.9: j-fiber OTDR trace, direction 2

factor and D the dose), it is sufficient to divide the RIA by the calibration factor found in Chapter 5 to obtain the dose profile as function of the distance. Fig. 6.10 and Fig. 6.11 show the dose profile along the fiber's path.

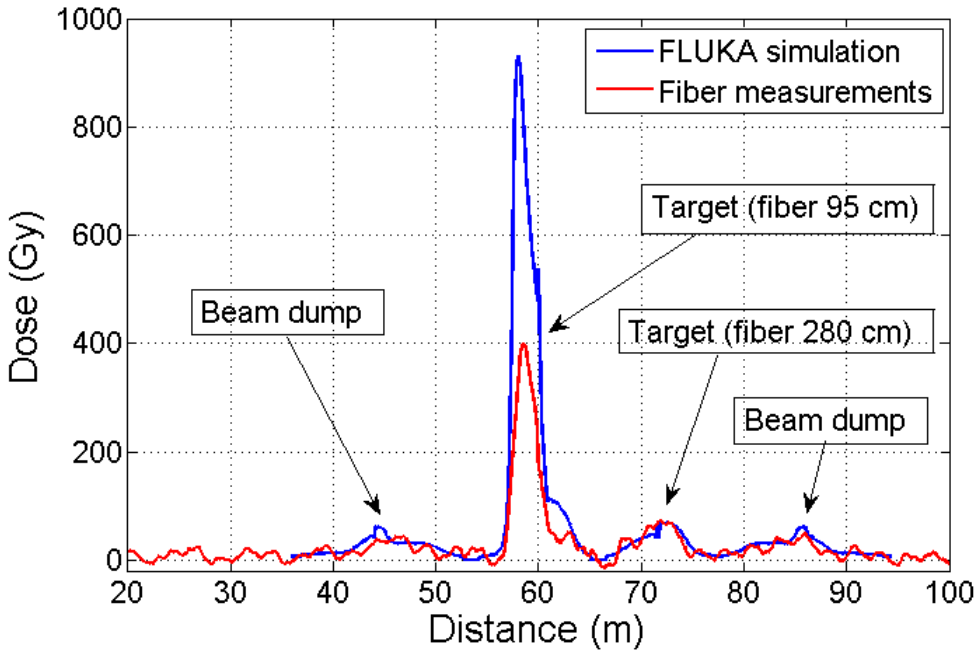

Figure 6.10: j-fiber, dose profile as function of the distance after 35 hours of irradiation, λ_1 = 850 nm

As can be seen from Fig. 6.10 and 6.11, the distributed measurement with the MMF j-fiber allows the detection of the main dose peak along the path estimating its magnitude at about 400 Gy. This peak corresponds to when the fiber passes the target at 0.95 m above the ground. Compared to the simulated FLUKA profile, the measured dose peak has been estimated around a factor 2.3 less at both wavelengths. This discrepancy is at least partially due to the fact that the FLUKA calculations scored the dose in air and not silica. The result is however relatively well in agreement with other detectors present in the CHARM facility, among which Beam Loss Monitors (BLM), RadFETs or RPL dosimeters, which all estimate the dose levels as being a factor 2 below the FLUKA results. The fiber's results is therefore promising taking into consideration that part of the observed discrepancy could also be due to the short pulse width of 5 ns used. This implies a lower Signal to Noise Ratio (SNR) which could impair the correctness of the measurements. In addition, the influence of the spatial resolution should

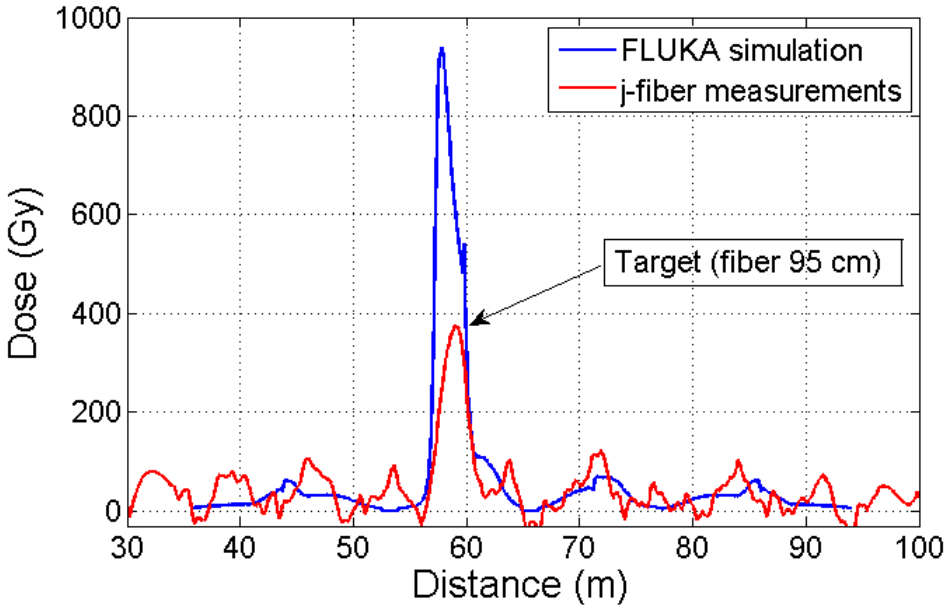

Figure 6.11: j-fiber, dose profile as function of the distance after 35 hours of irradiation, λ_2 = 1300 nm

also be taken into consideration given that the OTDR averages over 50 cm while other detectors are punctual and FLUKA calculates the dose profile averaged in 5 cm long segments.

At 850 nm, the second highest dose peak is also well localized at 72 m and corresponds to the second passing near the target at the higher height (2.80 m). The dose estimation seems to match FLUKA, this appearing match however, is due to the fact that the used calibration factor to obtain the dose profile from the RIA has been optimally chosen for the maximum dose rate found close to the target at 95 cm above the ground. As a consequence, this smaller dose peak is overestimated by the fiber's measurement. Other two dose peaks, at around 44 m and 87 m, are localized and represent the fibers' passing close to the beam dump wall where radiation levels are higher, but it is difficult to estimate their magnitude due to dynamic range limitations of the used parameters and measurement instrument which need to be further optimized.

As can be seen from Fig. 6.11, at 1300 nm it is not possible to appreciate the smaller dose peaks which are observable at 850 nm. This is due to the fact that the fiber's response at 1300 nm is less sensitive to radiation, the induced attenuation will therefore be smaller and more difficult to measure if the SNR is not high

enough. The dose peaks are lost in the noise as can be seen in Fig. 6.11.
A small uncertainty is also introduced as the calibration factors have been calculated for the wavelengths of 830 nm and 1312 nm while the OTDR wavelengths used for the distributed measurements were of 850 nm and 1300 nm. The difference in sensitivity is however so small that this uncertainty can be neglected.

Finally, a direct comparison with a set of RadFETs positioned along the fiber close to the target at 95 cm above the ground has been carried out. In particular, four RadFETs have been installed as close as possible to the fiber to ensure that the two different measurement systems would be affected by very similar radiation levels.

The results of the comparison is shown in Fig. 6.12 where the dose profile estimated with the j-fiber at λ = 850 nm and the RadFET measurements are both reported.

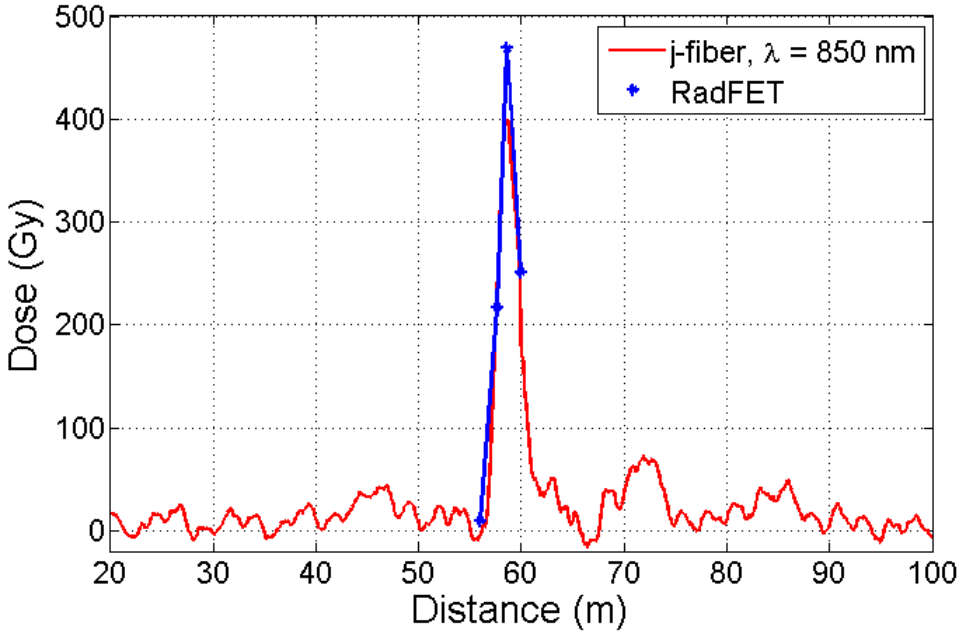

Figure 6.12: Dose profile estimated with the j-fiber at λ = 850 nm compared to RadFETs measurements

As can be seen from Fig. 6.12, there is a good match between the fiber's and the RadFETs' measurement. A maximum difference of about 15%-17% can be

appreciated at the peak location where the fiber has estimated the dose value as being about 400 Gy while the RadFET found about 470 Gy. This discrepancy is most probably due to the fact that the OTDR averages the dose value over 50 cm resulting in a lower dose with respect the the RadFET's measurement which is punctual. This difference is therefore stronger at the top of the peak where the dose gradient is the stronger. It has also to be considered that while the RadFET's measurement itself is very accurate, the uncertainty in the positioning of the RadFET and on it's orientation with respect to the incoming particles might propagate on the final dose value.

OFS MMF

A similar analysis as the one presented for the j-fiber MMF has been carried out for the measurements performed with the OFS MMF. The obtained dose profiles are shown in Fig. 6.13 Fig. 6.14. It can be observed that at 850 nm the major peak is also estimated to be about 400 Gy in agreement with the j-fiber's estimation. This match is possible although the OFS is not suitable for dosimetry because the applied calibration factor has been chosen to be optimum for the dose rate present at the location where the fiber passes close to the target at 95 cm above the ground. On the other hand, as shown in Fig. 6.14, only about 300 Gy have been estimated at 1300 nm. The reason for this discrepancy could be partially related to a particular composition of the fiber due to which at 1300 nm the combination of more points defects absorption bands results in specific dynamics not fully understood.

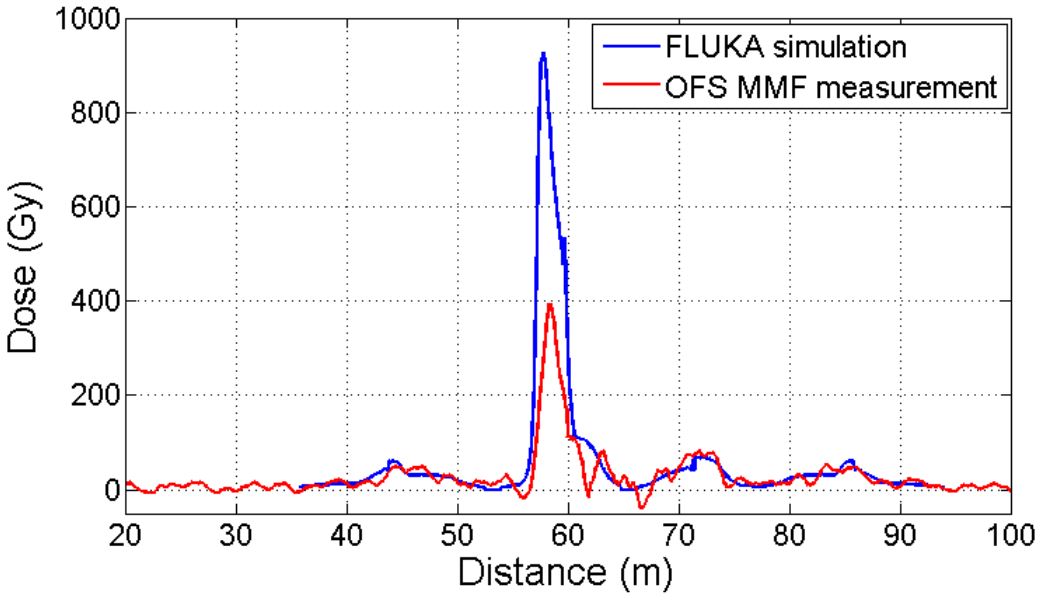

Figure 6.13: OFS MMF, dose profile as function of the distance after 35 hours of irradiation, λ_1 = 850 nm

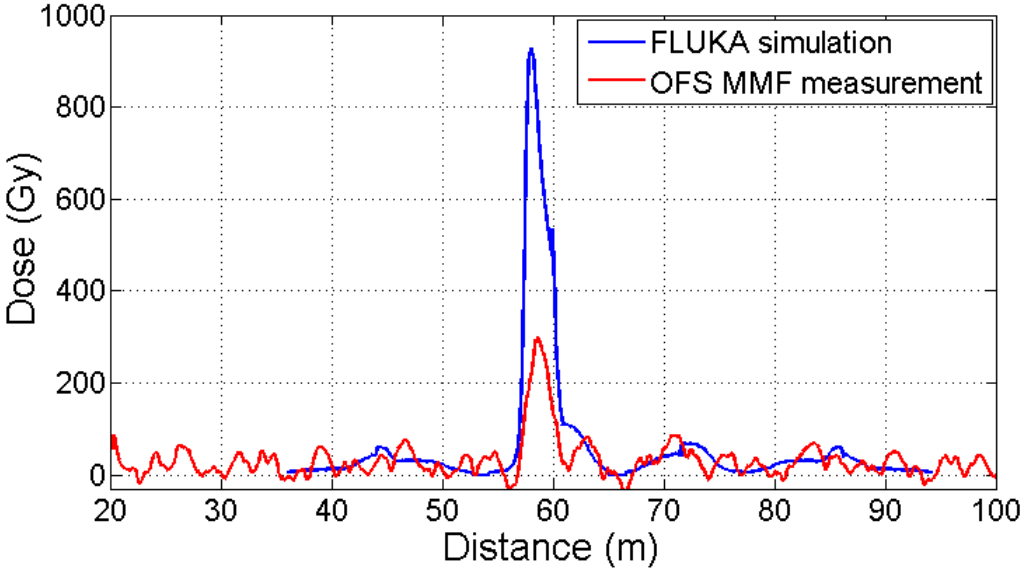

Figure 6.14: OFS MMF, dose profile as function of the distance after 35 hours of irradiation, λ_2 = 1300 nm

Draka SMF

Distributed measurements have also been carried out with the Draka SMF. It is important to remind that this fiber is considerably less sensitive to radiation with respect to the j-fiber MMF. In particular, at 1550 nm the Draka SMF has a sensitivity of about 200 μdB/m/Gy while at 830 nm the j-fiber has a sensitivity of about 3.5 mdB/m/Gy meaning there is about a factor 17 between the sensitivities of both fibers. The dose profile estimated from the distributed measurements on the Draka SMF at 1550 nm are shown in Fig. 6.15.

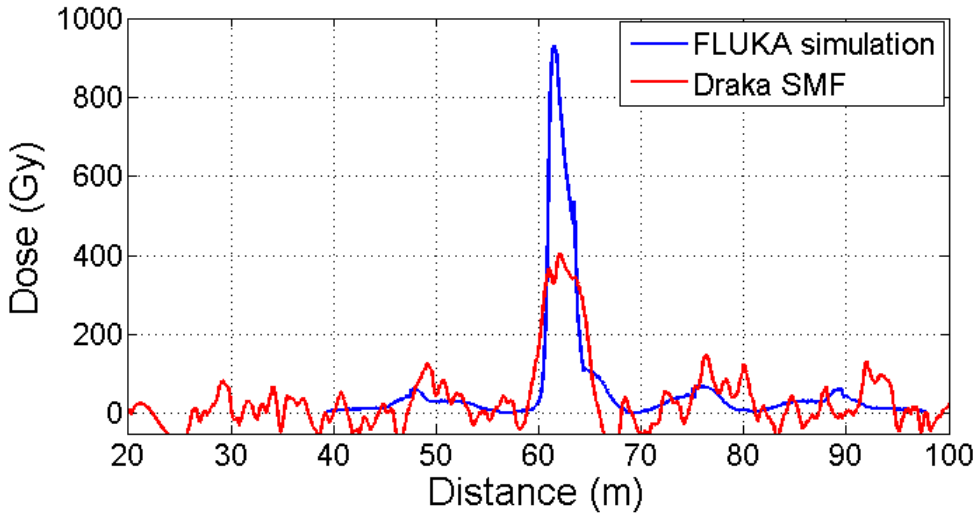

Figure 6.15: Draka SMF, dose profile as function of the distance after 35 hours of irradiation, λ = 1550 nm

As can be observed, the highest dose peak corresponding to where the fiber passes by the target at 95 cm above the ground, it correctly detected and its magnitude estimated to be 407 Gy consistently with the estimation of 400 Gy carried out with the j-fiber MMF, resulting in less than 2% difference between the measurements with the two different fibers. It is however important to observe that due to the low sensitivity of the Draka SMF and as a consequence, a degraded SNR, the peak's shape is slightly distorted if compared with the corresponding one in the j-fiber's profile. An even lower SNR doesn't allow for the detection of any other peaks. For this same reason, the distributed measurements carried out

at 1310 nm were of no use since the Draka SMF's sensitivity was a further factor 2 lower at that wavelength with a consequent lower SNR not allowing a clean trace.

6.3.2 Pulse duration: 10 ns

For the second distributed measurement campaign, the irradiation was carried out when the proton beam was impinging on a lower density Aluminum target for a maximum duration of almost 20 hours. In this case as well none of the movable shieldings was inserted in the facility. Given the lower density of the target and the duration of the irradiation, the reached radiation levels were not as high as in the case presented in the previous subsection. For this reason, only the results for the j-fiber MMF will be presented as it is a suitable fiber for dosimetry and sensitive enough to estimate these dose levels. The pulse duration was set to 10 ns, while the acquisition time was only 30 s this case. The distance between the samples or sampling resolution is about 8 cm for a total number of about 1625 data samples. The OTDR trace at the end of irradiation for the 850 nm wavelength is shown in Fig. 6.16. As can be observed, thanks to the longer pulse width, the SNR is higher with respect to the 5 ns measurements presented earlier, allowing for cleaner traces. As a result, even along direction 2, it is possible to detect smaller dose peaks after having already experienced major losses due to passing close to the target at 95 cm above the ground. Of course a longer acquisition time would have improved the SNR even further.

The results of the distributed measurements at 850 nm and 1300 nm are shown in Fig. 6.17 and Fig. 6.18. The figures show both the simulated FLUKA scored/averaged over 5 cm and a second one averaged over 1m for a more direct comparison with the fiber's result. However, as can be seen, in the presence of the low density target the dose gradients are not so strong and the two FLUKA traces are relatively close. Consistently with the results previously discussed, in this case as well the fiber's estimation of the maximum dose peak is about a factor 2 lower with respect to FLUKA. In particular, at 850 nm the fiber's estimation is 52% of FLUKA's simulated value while the ratio is of about 55% at 1300 nm. As can be also observed, thanks to the improved SNR, it is possible to better appreciate smaller dose peaks. In particular, the peaks visible at 43 m and 85 m corresponding to the two passages of the fiber close to the beam dump wall, have

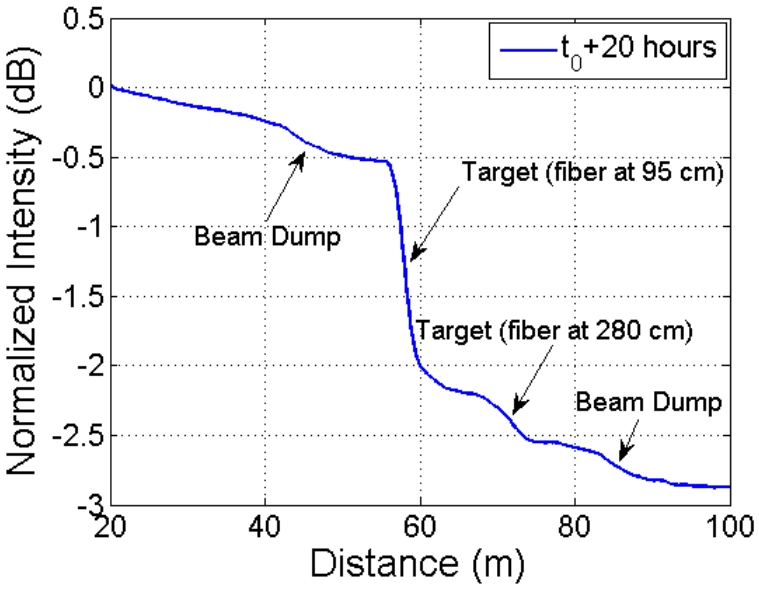

Figure 6.16: j-fiber MMF, OTDR trace after about 20 hours of irradiation, λ = 850 nm

been estimated at 9 Gy and 8.5 Gy while FLUKA simulated 19.7 Gy and 17 Gy respectively. The fiber's measurements are therefore mostly consistent in various points along the path and allow to estimate a dose variation as low as about 10 Gy which very promising and respectful of the targeted dose resolution.

To conclude on the distributed measurements, it is worth underlining how the appropriate choice of the pulse width is determinant to obtain a sufficiently good SNR to detect well even smaller dose peaks. In our case, we have shown that 10 ns duration pulse provide very good results allowing for a relatively high dose resolution of about 10-15 Gy. A further improvement can be provided by increasing the acquisition time, a systematic study of how the acquisition time affects the results for the given pulse width of 10 ns should be carried out. This is certainly challenging from an organizational point of view as the irradiation runs at CHARM generally last for about 3 days; it is difficult to schedule many measurements with different interrogation parameters on several fibers in such a short time. Given the deterioration of the fiber after 3 days and the limited SNR of the instrument, one needs to wait for a new set of fiber to be blown again and for the facility to be operational with the same target and shielding configuration.

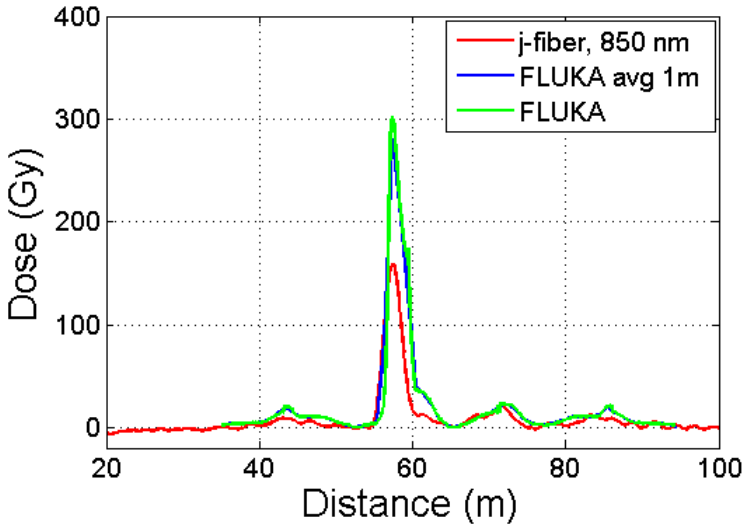

Figure 6.17: j-fiber MMF, dose profile as function of the distance after about 20 hours of irradiation compared to FLUKA (green) and FLUKA average over 1 m (blue), $\lambda = 850$ nm

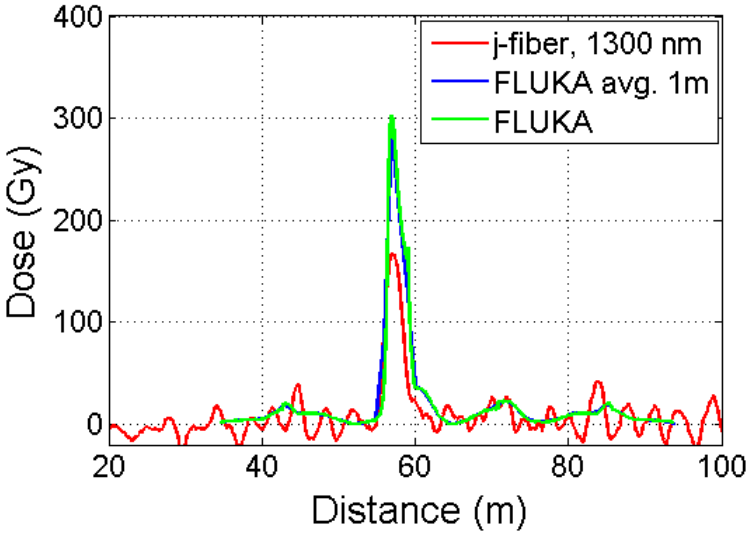

Figure 6.18: j-fiber MMF, dose profile as function of the distance after about 20 hours of irradiation compared to FLUKA (green) and FLUKA average over 1 m (blue), $\lambda = 1300$ nm

6.4 In-beam proton characterization

In the last section of this Chapter, some non-distributed measurements carried out at CHARM will be presented. The Draka SM, whose ^{60}Co characterization has been presented in Chapter 5, has been irradiated with only protons to better understand possible particle type dependencies of the RIA.

6.4.1 Experimental setup

When the target is not inserted into the irradiation hall at CHARM, no mixed field is being generated and the proton beam coming from the PS crosses the hall mostly unaffected. It is therefore possible to directly irradiate a fiber sample by placing it in the beam or what is called the "in-beam" position. In particular, the fiber sample is taped to a plexiglass card which is mounted on a test box shown in Fig.6.19, in such a way to be orthogonal to the impinging beam.

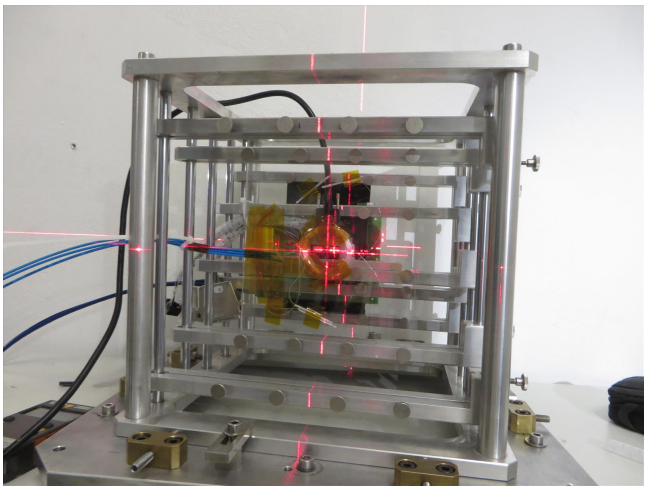

Figure 6.19: Test box holding the plexiglass card on which the fiber sample is taped to

As can be seen from Fig. 6.19, the test box can support several cards and other users may place their samples or electronic components to be tested. For the irradiation discussed in this section, a 12 m 34 cm long Draka SM fiber sample has been installed on the plexiglass card which is aligned with the test box by means of a laser.

The sample is winded in 5 cm diameter spool to avoid bending losses and have

been spliced on both ends to radiation resistant fibers used as lead fibers. Once the optical fiber sample is mounted in the test box, the test box itself is mounted on a remotely controllable conveyer called Montrac. This system consists in a "shuttle" or conveyer which moves on tracks and can bring the test box in the desired test position along the path of the track which can be seen in Fig. 6.20.

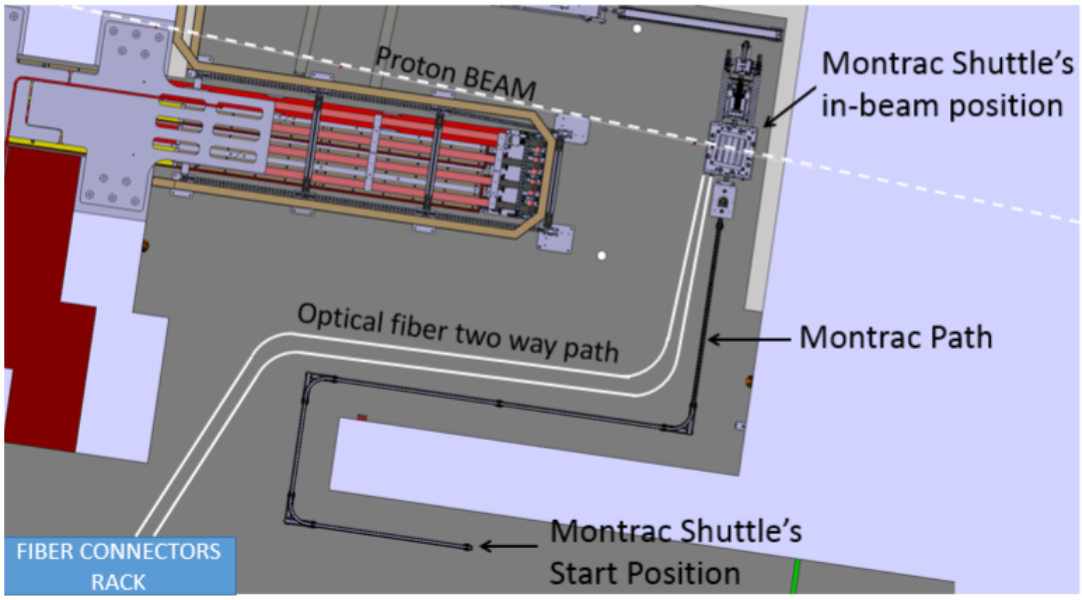

Figure 6.20: Fiber layout for in-beam measurements at CHARM

Fig. 6.20 also shows the path of the radiation resistant lead fibers which cross the irradiation hall and link the fiber sample placed in test position to the fiber connectors rack, without being affected by any possible radiation which is anyway extremely low given the absence of the target. This way, once reference measurements have been acquired, one knows that the observed induced attenuation will only be present in the fiber sample and not in the lead fibers. The length of the lead fiber between the fiber connectors rack and the in-beam test position is of about 35 m. From the fiber connectors rack situated close the irradiation hall and depicted in Fig. 6.20, 25 m long radiation resistant patch-chords reach the control room situated one floor above the irradiation hall and where the EXFO IQS-1743 optical power meter is placed.

To irradiate a sample directly with the proton beam, the so-called "blown-up beam" configuration needs to be set. This beam configuration allows to have a larger beam spot on the fiber under test, ensuring a smaller error on the beam spot

positioning as well as a larger area with lower intensity gradients. The blown-up beam shape is slightly elliptical with a major axis of about 10 cm and a minor axis of about 8 cm. Fig. 6.21 shows an estimation of a map for the dose deposited by $1.5 \cdot 10E15$ protons impinging in 1 day in the test position. It is possible to observe that at 2.5 cm from the center of the beam, corresponding to where the fiber is placed, the dose is relatively uniform.

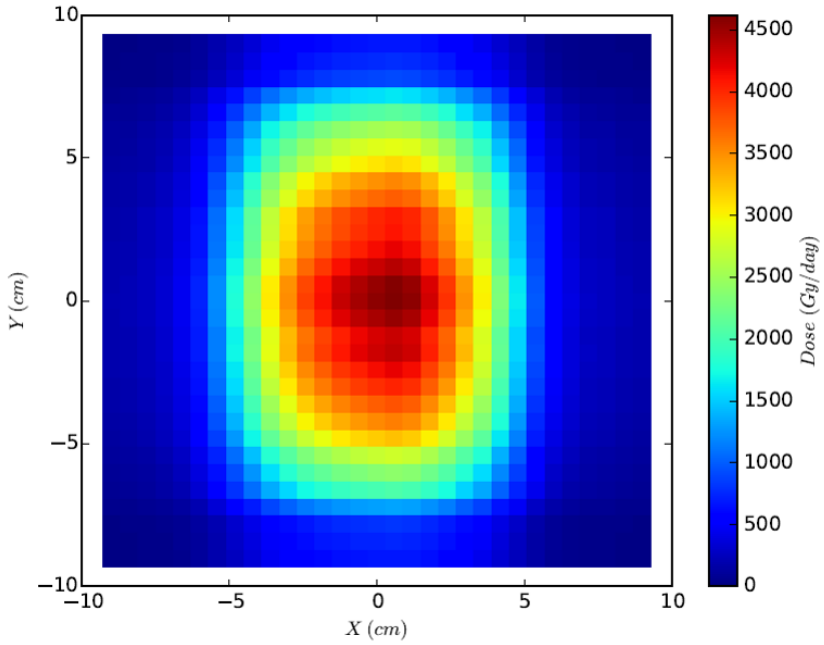

Figure 6.21: In-beam dose map for $1.5 \cdot 10E15$ protons on target in 1 day

An additional information on the dose's uniformity is provided by dose measurements carried out with a set of radfets depicted in Fig. 6.22. As for the fiber samples, the RadFET were mounted on the test box and left in-beam for 1 hour.

The result of the RadFET measurements are shown in Fig. 6.23 from which it can be understood that the dose does change along a 5 cm diameter circumference with respect to the center of the central RadFET (FB373). In particular, the dose varies up to a factor 1.7 along the circumference while a rough estimation based on the average considering that the circumference "touches" 12 RadFETs equally, results in about 210 Gy of mean dose.

During the irradiation test discussed in this section, the dose rate has unfortunately not been perfectly constant with about 12-13% of variation across the run

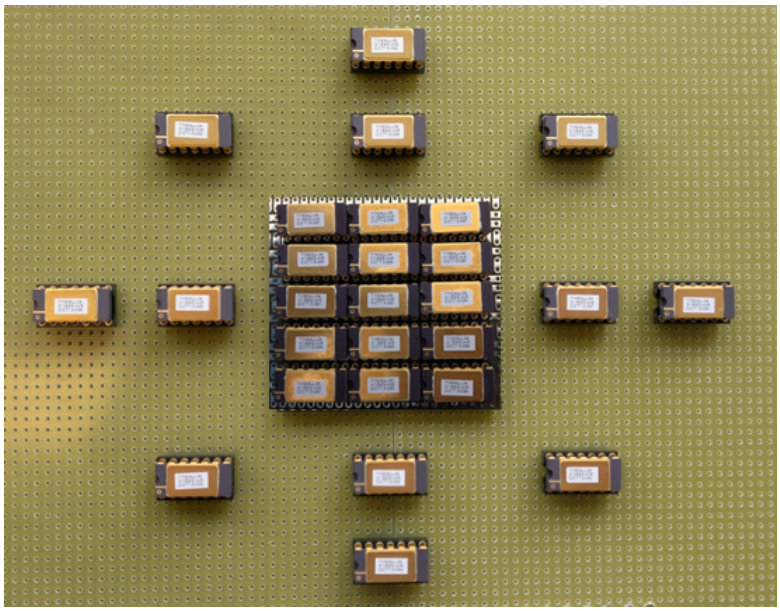

Figure 6.22: Radfet layout for in-beam dose estimation [102]

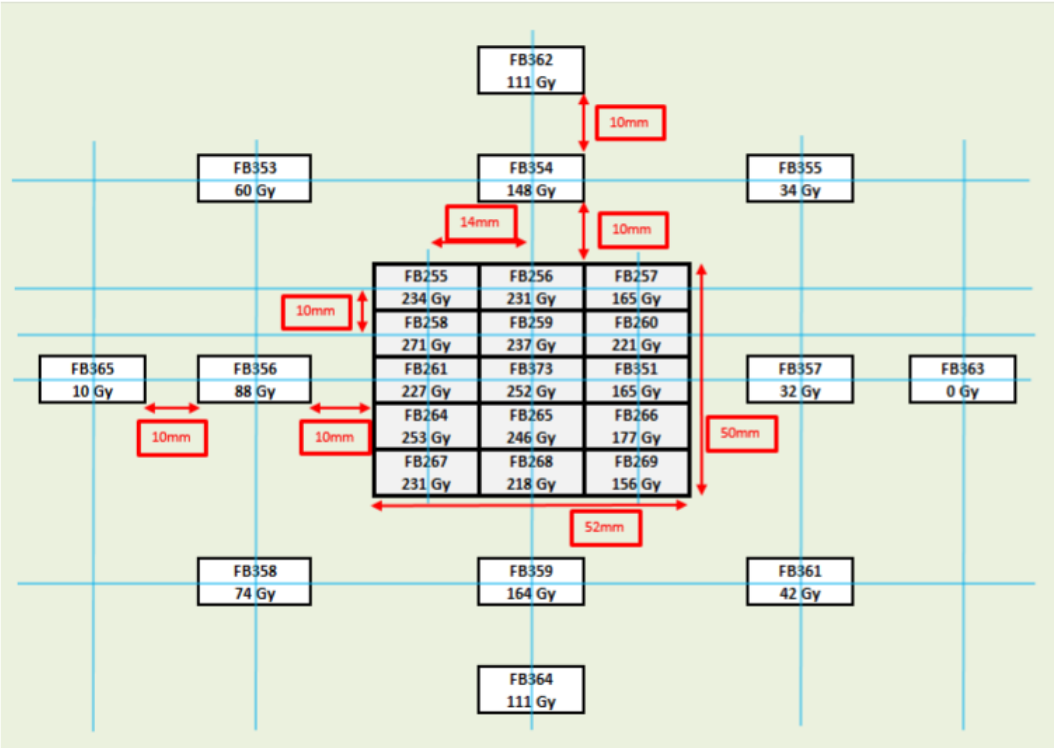

Figure 6.23: Radfet dose estimation [102]

with values ranging between 200 Gy/h (around 55 mGy/s) and 230 Gy/h (around 64 mGy/s). This information has been provided by a RadMON system (presented in Chapter 1) also mounted on the test box together with the fiber and which allowed estimate the dose as function of time online. In the results presented in the next subsection, the dose rate calculated from the RadMON measurements has therefore been considered even though the RadMON measured the dose in the center of the beam and not exactly in the same position of the fiber samples. It must therefore be taken into consideration that, with reference to 6.23, the dose values used for the characterization results are probably slightly overestimating the real values.

6.4.2 Results

Power Meter measurements

The irradiation of the samples lasted for a little more than 41 hours reaching about 9.4 kGy. Unfortunately, we were not able to set up the automatisation of the power meter measurements and therefore do not have a continuous flow of data along the whole duration of irradiation. For this reason we managed to acquire data in the linear range between about 500 Gy up to 1.1 kGy and in the non-linear range between 3 kGy and 6 kGy and some points around 9 kGy. The results of the irradiation are presented in Fig. 6.24 and Fig. 6.25 in terms of RIA as function of the accumulated dose and where they are directly compared with the results from the ^{60}Co irradiation already discussed in Chapter 5.

For the comparison showed in Fig. 6.24 and Fig. 6.25, the best curve in terms of SNR and dose range has been chosen from the corresponding ^{60}Co characterization, this is why for the 1300 nm comparison we used the curve corresponding to a dose rate of 1.1 Gy/s and for the 1550 nm comparison the curve corresponding to a dose rate of 0.45 Gy/s. From Fig. 6.24 and Fig. 6.25 it can be observed that both at 1310 nm and 1550 nm the proton and gamma characterization curves seem to have the same overall trend but in both cases an RIA offset is present between the curves. The insert, both in Fig. 6.24 and Fig. 6.25, shows a zoom of the linear part of the curves which both at 1310 nm and 1550 nm seem to be relatively parallel. A more detailed and quantitative analysis for both the linear

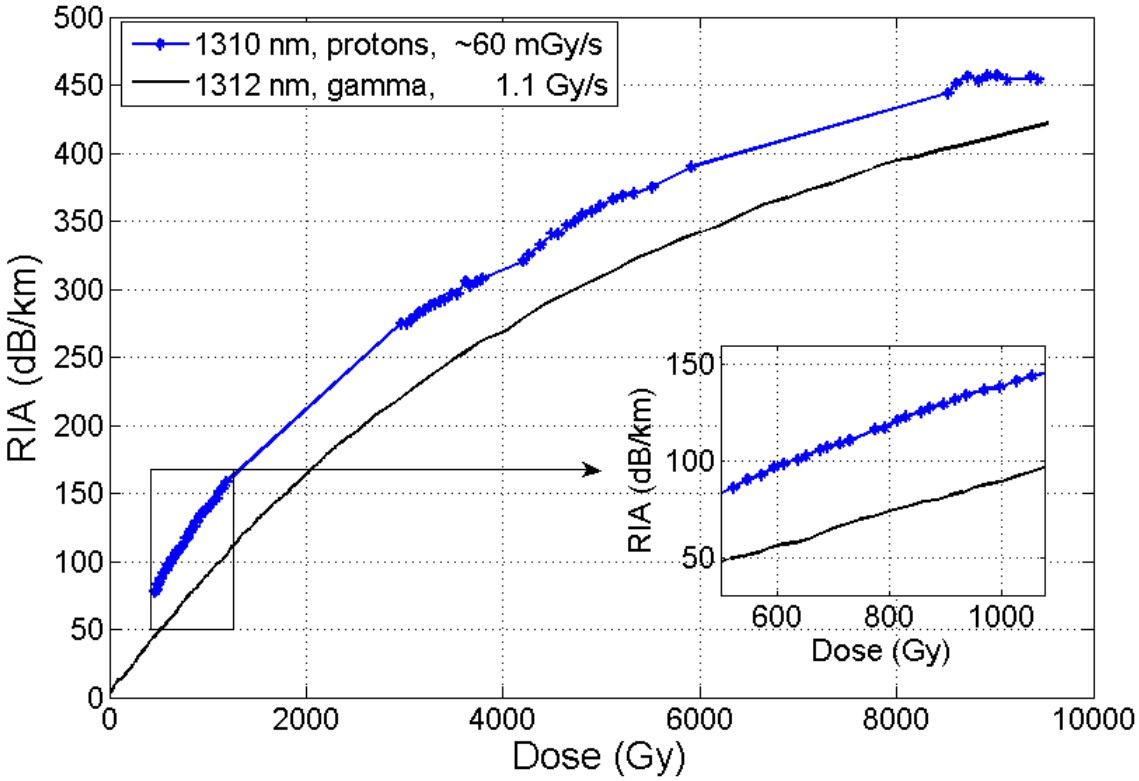

Figure 6.24: Draka SM: RIA as function of the accumulated dose, proton-^{60}CO comparison, λ =~ 1310 nm

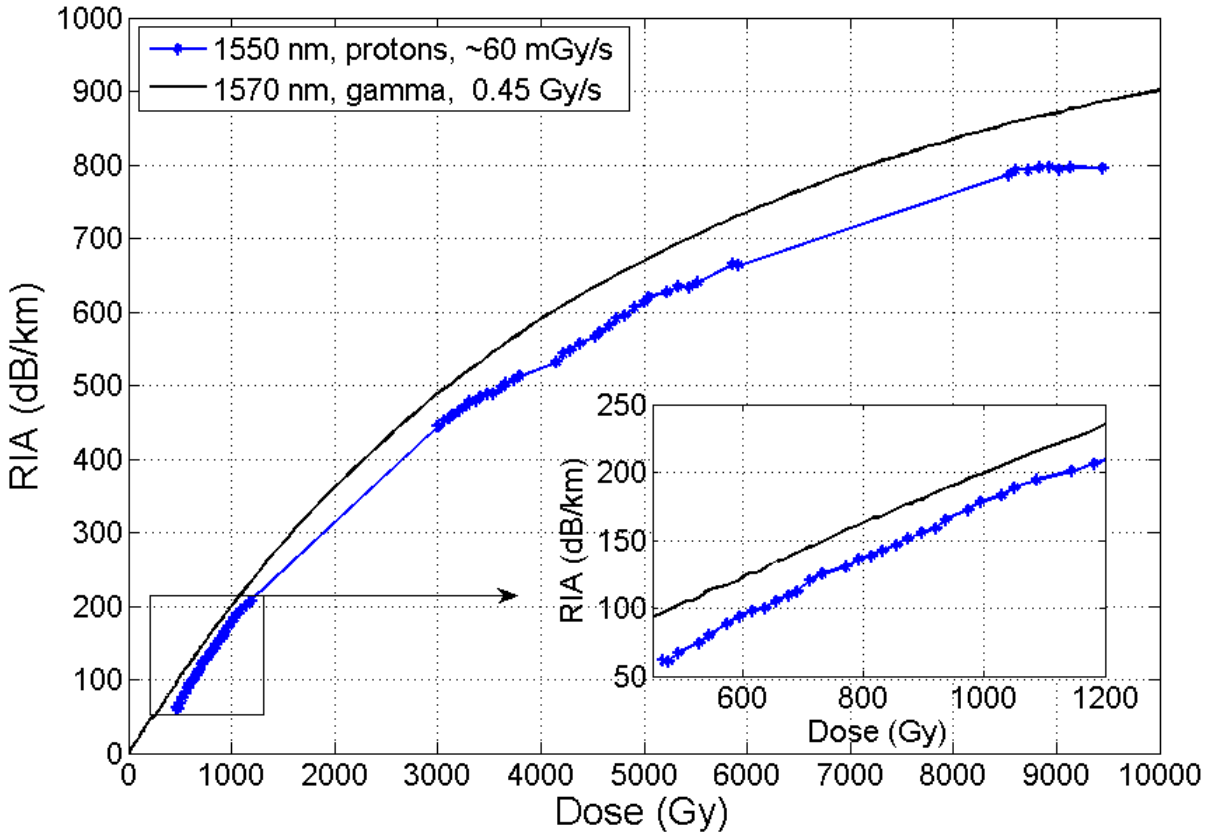

Figure 6.25: Draka SM: RIA as function of the accumulated dose, proton-^{60}CO comparison, λ =~ 1550 nm

and non-linear parts follows now supported by Fig. 6.26, Fig. 6.27, Fig. 6.28 and Fig. 6.29. In particular, Fig. 6.26 and Fig. 6.27 show how both at 1310 nm and 1550 nm, the linear part of the proton characterization curve can be well modelled by a linear fit. The obtained slopes representing the sensitivity of the Draka SMF, match very well the ones presented in Chapter 5 for the ^{60}Co. For the proton irradiation at 1310 nm we obtain 110 μdB/m/Gy compared the 100 μdB/m/Gy obtained for the ^{60}Co at the same wavelength, meaning a 10% difference between the two irradiation using two different particle types. At 1550 nm, for the proton irradiation we obtain 210 μdB/m/Gy compared to the 200 μdB/m/Gy obtained for the ^{60}Co at 1570 nm, meaning 5% difference between the two irradiations. Considering the already discussed uncertainties on the dose rate for both irradiations, these results show a very good match between irradiation with protons and with gamma.

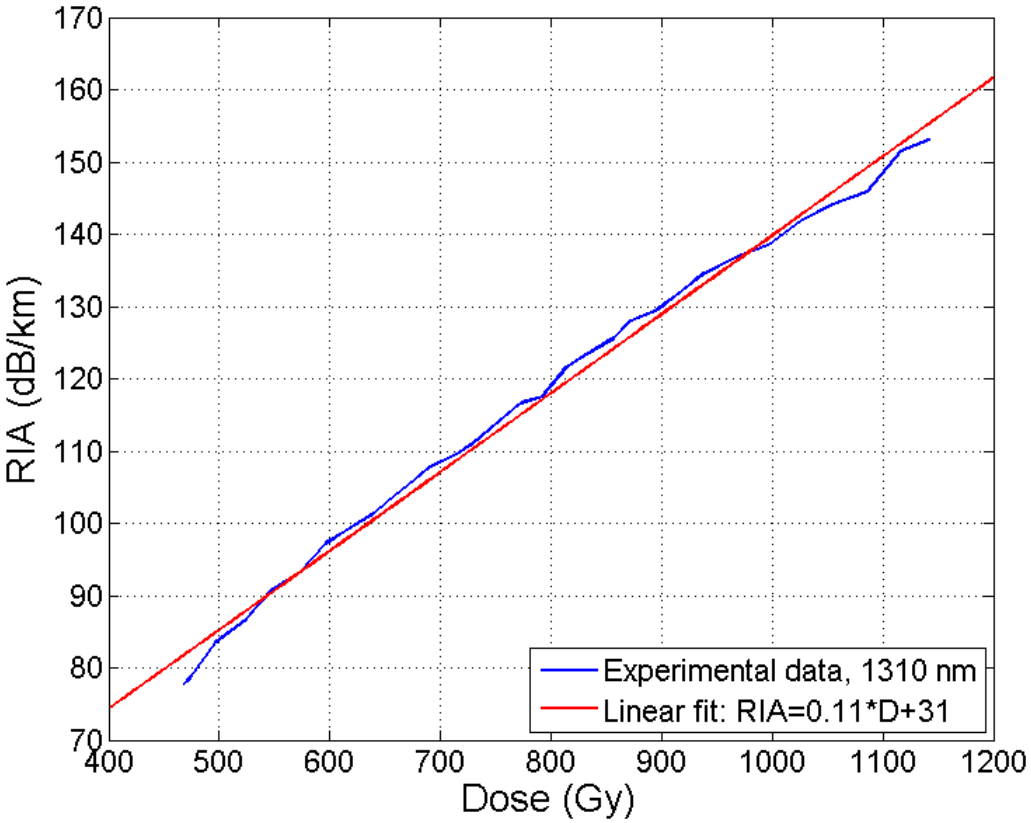

Figure 6.26: Draka SM's proton irradiation response in the linear range, λ = 1310 nm

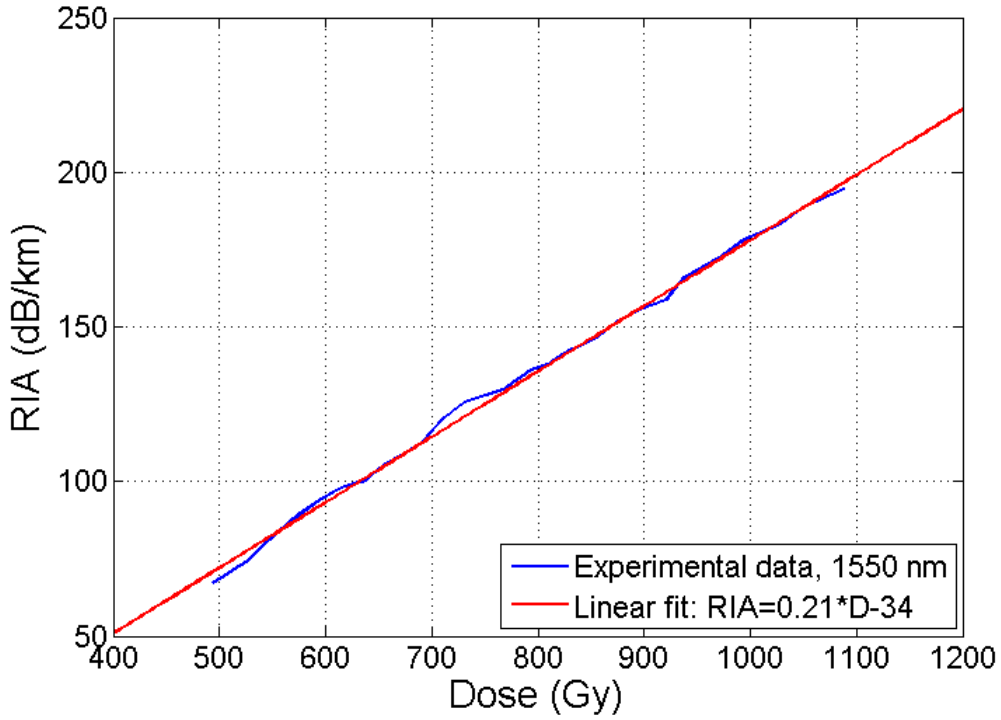

Figure 6.27: Draka SM's proton irradiation response in the linear range, $\lambda = 1550$ nm

The non-linear part of the characterization curves of the proton and gamma characterization has also been compared. Fig. 6.28 and Fig. 6.29 show the ratio obtained between the RIA for proton irradiation and the RIA for gamma irradiation. It can be observed that at 1310 nm the ratio ranges from about 1.09 and 1.23 indicating an offset between the protons and the gamma irradiation ranging between about 10% and a little more than 20%. The ratio therefore remains constant within 10%-12% over the whole non-linear range indicating the curves have similar trends. At 1550 nm the ratio ranges from about 0.88 and 0.92 indicating an offset between the protons and the gamma irradiation of about 8%-12%. The ratio therefore remains constant within less than 5% over the whole non-linear range indicating the curves have similar trends. These offsets are most probably due to the various uncertainties present in both measurements including the ones on the dose rate and sample length. The results of this analysis strongly suggest an independence of the attenuation induced by different particle types, at least between protons and gamma, as expected from the theory presented in Chapter 3.

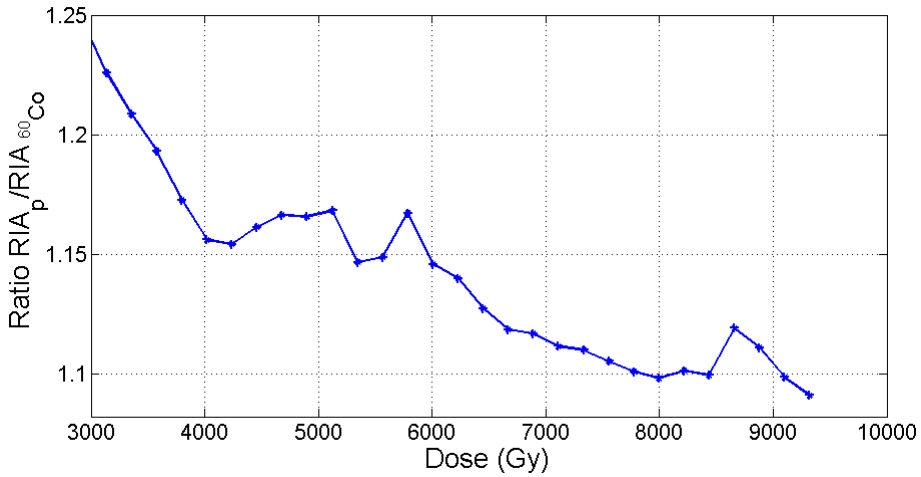

Figure 6.28: Ratio $RIA_{protons}/RIA_{^{60}Co}$, λ =~ 1310 nm

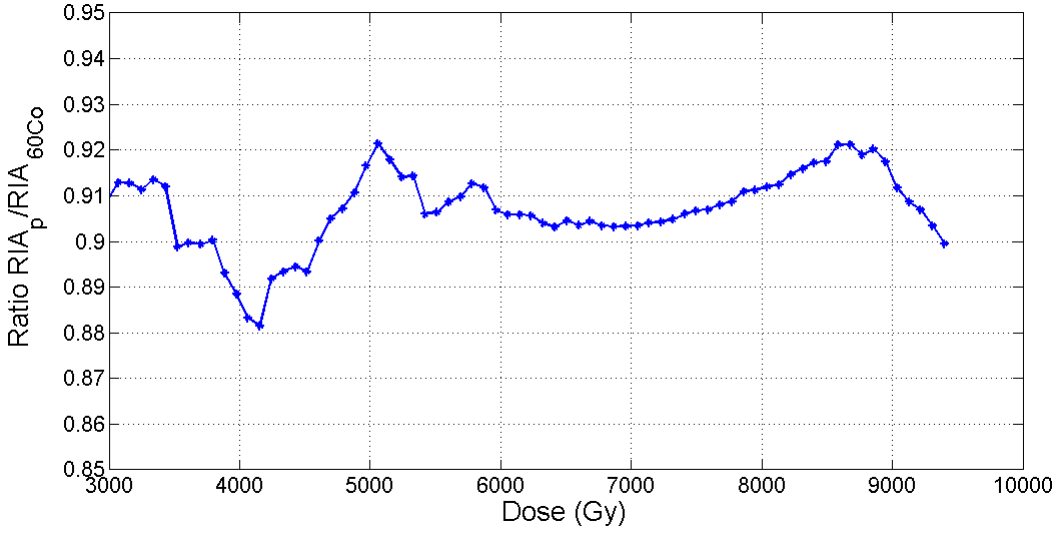

Figure 6.29: Ratio $RIA_{protons}/RIA_{^{60}Co}$, λ =~ 1550 nm

7 Distributed temperature measurements at CHARM

Accurately measuring temperature distributions in harsh environments affected by mixed field radiation as the one present in the LHC is of great importance if not necessary in the assistance to a distributed optical fiber radiation sensor given the temperature dependence of the RIA in certain radiation sensitive optical fibers as explained in Chapter 3. A Raman Distributed Temperature Sensor (RDTS) assisted by a DOFRS could strongly benefit from a temperature compensation allowing for more reliable radiation sensing results.
At the same time, reliable distributed temperature measurements in harsh environments, could also be very useful to monitor the temperature at CERN's accelerators for safety purposes ensuring an immediate and reliable detection of abnormal temperature variations which could indicate the presence of a fire or a cooling liquid leakage. Given the space resolved nature of the RDTS, the localization of the fault could quickly be communicated helping reducing the intervention time.
In this Chapter, the theory behind Raman-based distributed temperature sensing will be provided followed by the experimental results of distributed measurements carried out in the CHARM facility.

7.1 Temperature dependence of spontaneous Raman

Since its discovery in the mid 80s, distributed fiber optic sensing using the temperature dependence of the Raman scattering has been exploited to develop dis-

tributed sensors, in particular for temperature sensing [4]. Such sensors are in fact having a wide success in the last years thanks to the unique features they provide which more conventional sensors do not offer. Raman-based distributed temperature sensors have the ability to measure temperature at thousands of points along a sensing fiber in an accurate and fast way without the need of multiplexing thousands of discrete sensors. Such an ability is particularly interesting for the temperature monitoring of large or long structures as oil and gas pipelines, oil wells, power cables, tunnels, nuclear reactors and many more. In the next section the basic characteristics of Raman scattering in optical fibers is presented as well as the sensing configuration of Raman based distributed temperature sensors.

7.2 Spontaneous Raman Scattering in Optical Fibers

Raman scattering is generated by the interaction of light with resonant modes of the molecules in a medium. Two kinds of interactions are mostly considered, one between the photons and the vibrational modes of the molecules, generally called vibrational Raman scattering, and the other between the photons and rotational modes generating the so-called rotational Raman scattering. It is important to bare in mind that vibrational Raman scattering is much stronger than the rotational one and exhibits a frequency shift one order of magnitude greater than the one due to rotational Raman scattering [103].
The Raman scattering can be described in terms of quantum energy levels as depicted in Fig. 7.1. In fact, a molecule initially in its ground state which we indicate by "vibrational state 1" can be excited by an incident photon of frequency ω_{photon} to a higher energy level which we indicate by "vibrational state 2" by means of an intermediate virtual state. The incident photon is therefore virtually absorbed simultaneously to the emission of a photon with frequency ω_{Stokes}. Such a process corresponds to what is known as Raman Stokes scattering where the production of a downshifted frequency photon (lower energy photon) takes place following the conservation of energy: $\omega_{Stokes} = \omega_{photon} - \Omega_R$ where Ω_R is the frequency associated with the energy of the vibrational mode. If on the other hand, the molecule already has some vibrational energy and is already in "state 2", the incident photon

can absorb a quantum of energy from the medium giving rise to the emission of an upshifted frequency photon (higher photon energy) at $\omega_{anti-Stokes} = \omega_{photon} + \Omega_R$. This second process is known as Raman anti-Stokes scattering.

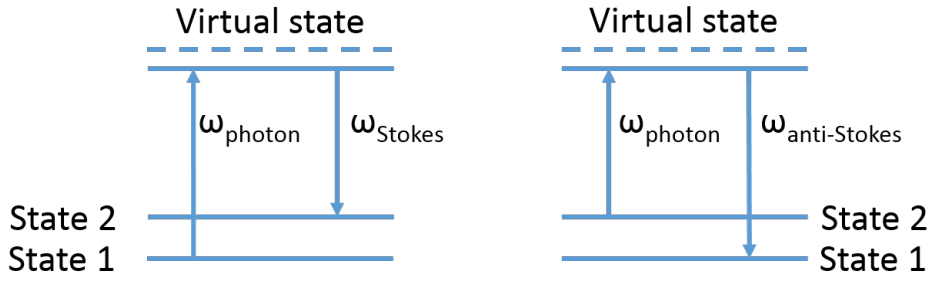

Figure 7.1: Energy level diagrams describing both the Raman Stokes and anti-Stokes scattering

The induced Raman frequency shift Ω_R is a significant fraction of the optical frequency due to the high energy of the vibrational modes. Typically, the Raman spectrum exhibits several peaks at different frequency shifts depending on the vibrational energy of the involved modes. In addition, not every vibrational mode leads to a strong Raman scattering and the Raman intensity is expected to vary from mode to mode [103]. In a quantum mechanical approach, vibrational modes are represented by optical phonons which have a much higher energy than acoustic phonons involved in Brillouin scattering for example. For this reason, the Raman frequency shift in optical fibers is usually three orders of magnitude higher than the Brillouin frequency shift as schematically depicted in Fig. 4.1 along with other spectral components resulting from light scattering in an inhomogeneous medium [70].

It is to be noted that for each molecular vibration, two Raman components can be observed: the Stokes process associated with the absorption of energy from the incident photon and the anti-Stokes process associated with the emission of a photon with energy higher than the one of the incident photon. The Placzek model of spontaneous Raman scattering describes such a process as amplitude modulation producing lower and upper sidebands in the scattered spectrum. Following this interpretation, the induced dipole moment P of a molecule can be expressed as follows [104]:

$$
\begin{aligned}
P &= \beta E_p cos(w_p t) \\
&= \beta_0 + \left[\frac{\partial \beta}{\partial Q} Q_0 cos(\Omega_R t)\right] E_p cos(\omega_p t) \\
&= \beta_0 E_p cos(\omega_p t) + \frac{\partial \beta}{\partial Q}\frac{Q_0}{2} E_p cos[(\omega_p + \Omega_R)t] \\
&+ \frac{\partial \beta}{\partial Q}\frac{Q_0}{2} E_p cos[(\omega_p + \Omega_R)t]
\end{aligned} \tag{7.1}
$$

where β is the molecular polarizability, ω_p and Ω_R are the frequencies of the incident light and the molecular vibration, E_p and Q_0 are the amplitude of the pump field and molecular vibration respectively. To be noted that the the first right-side term of equation 7.1 denotes Rayleigh scattering while the second and third terms denote Raman anti-Stokes and Stokes scattering respectively.
Since optical phonons need to have a certain level of energy to be transferred to the scattered photons, in typical conditions, the Raman anti-Stokes process can only occur through thermal excitation of the molecules. For this reason the anti-stokes component is expected to vanish at a temperature T = 0K. Since spontaneous Raman Stokes scattering can still occur at T = 0K, it turns out that both Raman components do not exhibits the same intensity. According to the Placzek model however, both Raman components should have the same power, even if the only molecular motion come from zero-point fluctuations at T = 0K [104]. The asymmetry between both Raman components can be explained by the Raman amplification of the zero-point fluctuations at the Stokes frequency [104]. In fact, modulation and amplification contributions to the Stokes component are the same at T = 0K, leading to the cancellation of the anti-Stokes sideband due to absorption, as shown in Fig. 7.2.

Thermal excitation of the vibrational modes increases both Stokes and anti-Stokes intensities for different increasing temperatures but the above mentioned asymmetry remains. The transition rate for the Stokes process W_S due to thermal excitation is proportional to $1 + N_\Omega$, while the transition rate for the anti-Stokes process W_{AS} is proportional to N_Ω as shown in equations Eq. 7.2 and Eq. 7.3:

$$
W_S \propto N_0(1 + N_\Omega) \quad Stokes, \tag{7.2}
$$

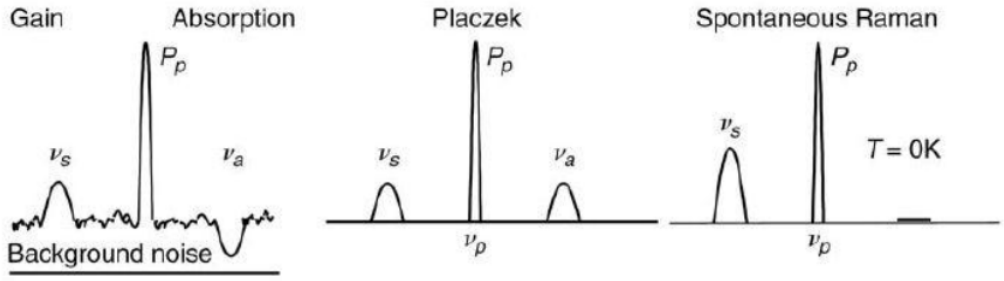

Figure 7.2: Raman amplification of the Placzek Stokes sideband and simultaneous absorption of the Placzek anti-Stokes sideband, both at T = 0K [104]

$$W_{AS} \propto N_0 N_\Omega \quad anti - Stokes \tag{7.3}$$

where N_0 is the incident photon number which is proportional to the light intensity. N_Ω is the Bose-Einstein thermal population factor which is proportional to Q_0^2 where Q_0 is the thermal amplitude of the molecular vibration, determining theamplitudes of the second and third right-side terms of Eq.7.1. The Bose-Einstein thermal population factor is expressed the following way:

$$N_\Omega = \frac{1}{exp(h\nu_R/k_B T) - 1} \tag{7.4}$$

where h is the Planck constant, k_B the Boltzmann factor, $\nu_R = \Omega_R = 2\pi$ is the vibrational frequency and T is the absolute temperatures in degrees Kelvin. The ratio of the anti-Stokes to Stokes intensities is $exp(-h\nu_R/k_B T)$ evidencing that at high temperatures the anti-Stokes scattered intensity approaches the Stokes intensity. In addition, the ratio tends to zero at T = 0K due to the inexistent anti-Stokes component at such a temperature.

Finally, it is worth to mention an important feature of Raman scattering which is related to the frequency dependence of the scattered light. From the Placzek model, it can be found that the electric field of the scattered light is proportional to $\nu_i^4 = (\omega_i/2\pi)^4$ (with $i = S,\ AS,\ or\ R$ for the Stokes, anti-Stokes and Rayleigh components, respectively). The Raman scattering cross-section for the Stokes component for example, defined as the ratio of the scattered Stokes power and the incident pump power, is given by:

$$\sigma \propto \frac{P_S}{P_0} \propto \nu_S^4 \frac{n_0}{n_S} \left(\frac{\partial \beta}{\partial Q}\right)^2 Q_0^2 \tag{7.5}$$

where n_0 and n_S are the refractive index at the pump and Stokes wavelengths and the factor $\partial\beta/\partial Q$ relates the Raman scattering cross-section with the Raman gain coefficient.

It is a well known fact that the composition and structure of a material can be characterized by the Raman scattering frequency shift in the material itself. Raman spectroscopy has therefore been used to analyze composition and impurities in optical fibers and as consequence optical fiber devices based on the Raman effect have also been developed [4]. The measured Raman spectrum obtained in a silica fiber pumped at 532 nm is depicted in Fig. 7.3 [105][106]. As can be observed, the Raman spectrum is sufficiently displaced from the incident light wavelength and can therefore easily be separated by means of standard optical filters.

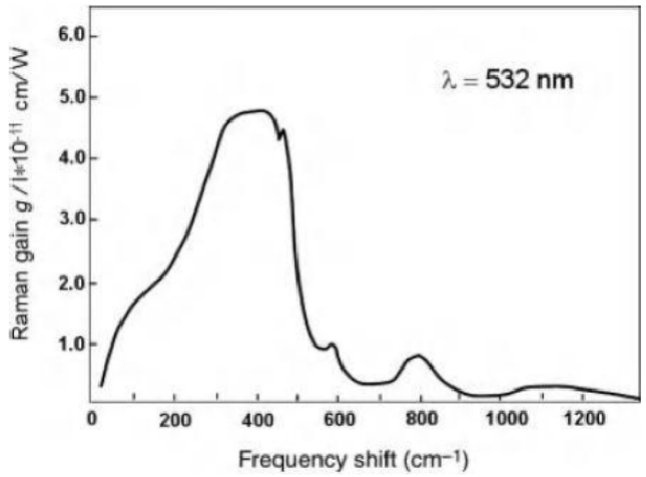

Figure 7.3: Raman gain spectrum for vitreous silica

The peak wave number shift of Raman scattering of vitreous silica measured by a pump laser beam at 532 nm is 420 cm^{-1} which corresponds to a peak frequency shift of 13 THz. The line-width is relatively large, about 9 THz and it is attributed to the molecular structure of vitreous silica. It is worth noticing that the effective Raman cross-section depends on the specific fiber structure which implies a different mode distribution between step-index and gradient-index fibers as well as between single-mode optical fibers (SMF) and multi-mode optical fiber (MMF). The scattering capture fraction therefore depends both on the effective

refractive index n and the fiber numerical aperture (NA) [4] as follows:

$$S = \frac{3}{2n^2}(NA)^2 \tag{7.6}$$

The spontaneous Raman scattering process is a rather weak process. For example, in the case of condensed matter the scattering cross-section per unit volume for the Raman Stokes component is only in the order of 10^{-6} cm^{-1} while it is even lower for a 50/125 μm graded-index MMF. As a result, only $2.5x10^{-9}$ of the power of an incoming optical pulse is backscattered in 1 m of fiber at the anti-Stokes Raman line [107]. In the case of SMFs, this value is even further reduced due to their lower capture factor.

In step-index fibers, a homogeneous distribution of the light over the effective cross-section (A) of the core can be assumed. If a small volume of fiber Adz is considered, there should therefore exist NAdz molecules inside of it, where N is the molecule density of the fiber core [108]. The total power of these molecules, considering both the Raman Stokes and Raman anti-Stokes components can be written as:

$$dP_S = (1 + N_\Omega)\Gamma_S P_0 dz \tag{7.7}$$

$$dP_{AS} = N_\Omega \Gamma_{AS} P_0 dz \tag{7.8}$$

where N_Ω is the Bose-Einstein thermal population factor, Γ_S and Γ_{AS} are the Raman Stokes and anti-Stokes capture coefficients and P_0 the power of the incident light [108]. Equations 7.7 and 7.8 point out that, since both Stokes and anti-Stokes powers depend on the Bose-Einstein probability distribution of phonons, the spontaneous Raman scattering results to be a temperature dependent process caused by thermally driven molecular vibrations. This temperature dependence provides a mechanism to perform distributed temperature sensing based on spontaneous Raman scattering using an optical fiber [105]. Taking into account that at room temperature $N_\Omega \simeq 0.1$, it is important to put emphasis on the fact that the intensity of the Raman Stokes light (downshifted frequency component) exhibits only a slight temperature dependence while the intensity of the Raman anti-Stokes light (upshifted frequency component) shows a strong dependence on the local fiber temperature. Fig. 7.4 shows the temperature sensitivity of the spontaneous anti-Stokes Raman scattering which has been measured over a range

of temperature from -52°C to +100°C. In particular, the figure reports a quasi-linear relative sensitivity of 0.8%/K at around room temperature which changes slightly to 1.2%/K at about -52°C [109]. Even though the absolute power of the anti-Stokes Raman component is more than 30 dB weaker than the Rayleigh backscattered component, its sensitivity is high enough to allow the development of a distributed temperature sensor for real applications.

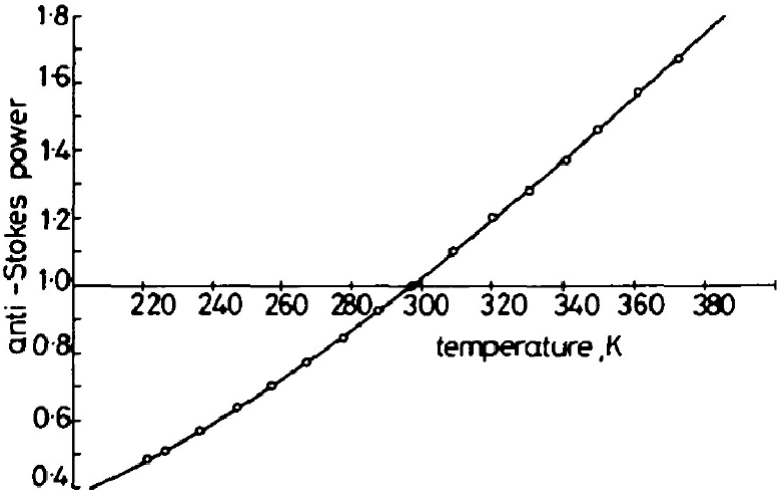

Figure 7.4: Raman anti-Stokes signal measured as a function of the fiber temperature. The vertical axis being normalized at room temperature [109]

7.3 The Raman Distributed Temperature Sensor (RDTS)

RDTS temperature sensors in which the temperature estimation is usually obtained by measuring the Stokes and anti-Stokes spontaneous Raman backscattering intensities generated by optical pulses propagating along the sensing fiber, often exploit OTDR techniques to be realized [110]. One of the key advantages of an OTDR based RDTS is that it can be effectively implemented using standard MMF telecommunication fibers which are relatively inexpensive and commonly available. To better understand how this kind of sensors work, a typical configuration of a Raman-OTDR-based sensor system is shown in Fig. 7.5, which consists of a pulsed pump laser to perform OTDR measurements with pulses of

duration proportional to the required spatial resolution as explained in Chapter 4, an optical circulator to deliver optical pulses to a long sensing fiber, which is usually an MMF to transmit higher peak-power optical pulses and to pick-up the returned weak signal. An optical narrow band pass filter is used to allow the Stokes and anti-Stokes components to be detected separately with high isolation from the backscattered Rayleigh component. To be noted that although the Raman frequency shift of 13 THz is quite large, about 100 nm at around 1550 nm, the side lobe suppression ratio of the filter must be high enough remembering that the Raman scattering intensity is much lower than that of the Rayleigh scattering, typically 30 dB lower. Given the low intensity of spontaneous Raman scattering, a single receiver is usually composed of an avalanche photodiode (APD) followed by a high-gain transimpedance amplifier (TIA) and an analog-to-digital converter (ADC) connected to a processor.

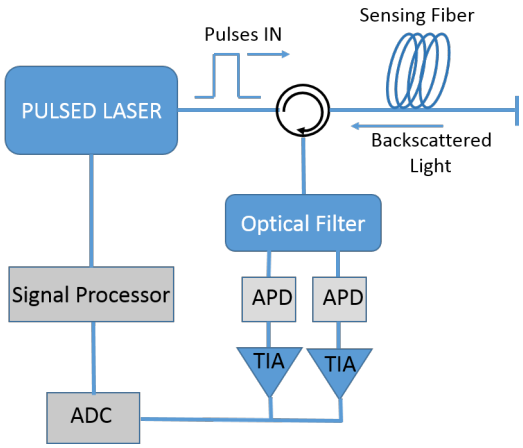

Figure 7.5: Generic block diagram of a typical single-ended OTDR-based RDTS temperature sensor

The wavelength dependence of the Raman scattering has been analyzed and it has been demonstrated that long wavelength lasers are beneficial forloweroptical loss and longer sensing fibers [111].

The performance of an RDTS temperature sensor can be expressed in terms of sensing distance, precision of the localization of an event, precision and range of the measured temperature as well as the measurement time. The basic technical concern to improve these performances is to enhance the SNR since a higher SNR means to be able to sense over longer distances, having a faster response of the sen-

sor data readout, a higher spatial resolution and a higher precision of temperature measurement [4]. Of course some fundamental trade offs subsist, for example, to enhance the SNR, multiple data collection and averaging can be performed resulting however in longer measurement times to obtain the final temperature profile. The spatial resolution of RDTS is a fundamental parameter which is determined by the laser pulse duration and the photoreceiver's response. By shortening the pulse duration of the employed laser source it is possible to increase the spatial resolution as it was already explained in Chapter 4 when discussing OTDRs. However, another trade off takes places since shorter pulses mean fewer photons to be integrated leading consequently to either longer data processing times and/or to lower sensing distances.
Finally, it is important to explain that the OTDR traces of the anti-Stokes component alone are not commonly used for temperature sensing, since these traces also depend on fiber losses, whose variations might be easily interpreted as a temperature change, inducing errors in the measurement. To overcome this problem, the anti-Stokes intensity trace needs to be normalized by a temperature independent trace, such as the Stokes (which is only slightly temperature dependent) or the Rayleigh component, so that local fiber loss effects are effectively cancelled out. [112][113].

7.3.1 Single-ended RDTS

In principle, RDTS based on OTDR techniques require the access to only one fiber-end as was schematically depicted in Fig. 7.5. The spontaneous Raman backscattered light is therefore measured at the near fiber-end allowing one to detect the temperature distribution.
In particular, a pump pulse propagates along an optical fiber and generates spontaneous Raman scattering depending on the pulse position along the fiber at each particular time. The Stokes Raman power reaching the photodiode at the near fiber-end ($z = 0$) and backscattered from a region of extension ΔL which is equal to half of the pulse width at a position z, is given by [86]:

$$P_S(z)|_{z=0} = (1 + N_\Omega)\Gamma_S P_0 \Delta L \, exp[-(\alpha_S + \alpha_P)z] \tag{7.9}$$

where P_0 is the pump power and α_S and α_P are the fiber loss coefficients at the Stokes and pump wavelengths. Similarly, the anit-Stokes Raman power reaching the fiber input ($z = 0$):

$$P_{AS}(z)|_{z=0} = N_\Omega \Gamma_S P_0 \Delta L \, exp[-(\alpha_{AS} + \alpha_P)z] \tag{7.10}$$

where α_{AS} is the fiber loss coefficient at the anti-Stokes wavelength.
If the ratio of the ani-Stokes to Stokes power is calculated [114], we obtain:

$$\begin{aligned} R(z) &= \frac{P_{AS}(z)}{P_S(z)} \\ &= C_R \, exp[-(\alpha_{AS} + \alpha_S)z] \left(\frac{N_\Omega}{1 + N_\Omega} \right) \\ &= C_R \, exp[-(\alpha_{AS} + \alpha_S)z] exp\left[\frac{-h\Delta\nu}{k_B T(z)} \right] \end{aligned} \tag{7.11}$$

where C_R is a constant which takes into account the differences in the Raman capture factor and in the response of the receiver at the Stokes and anti-stokes wavelengths; α_S and α_{AS} are the fiber attenuation coefficients at the Stokes and anti-Stokes wavelengths, respectively; $\Delta\nu$ is the frequency separation between the Raman and pump signals, h is the plank constant, k_B is the Boltzmann constant, and T(z) is the fiber temperature. As can be seen from Eq. 7.11 the ratio R(z) depends on the wavelength-dependent losses (WDL) of the fiber ($\alpha_{AS} - \alpha_S$). In case this factor can be properly characterzied as a function of the distance, it can be corrected from 7.11 leading to an expression which is independent of the launching conditions [114]:

$$R(z) = C_R \, exp\left[\frac{-h\Delta\nu}{k_B T(z)} \right] \tag{7.12}$$

Using Eq. 7.12 it is difficult to measure the absolute temperature because of possible inaccuracies when determining the coefficients C_R, value which can differ from fiber to fiber. If however, a reference measurement is used at a known temperature T_{ref}, the obtained reference ratio $R_{ref}(z)$ can be used for calibration, allowing for an accurate estimation of the temperature along the fiber according

to [114]:

$$T(z) = \left(\frac{1}{T_{ref}(z)} - \frac{k_B}{h\Delta\nu} ln \left[\frac{R(z,T)}{R_{ref}(z,T_{ref})} \right] \right)^{-1} \tag{7.13}$$

To be noted that Eq. 7.13 is obtained by taking the ration $R(z,T)/R_{ref}(z,T_{ref})$ and using Eq. 7.12. It is worth to say that in order to neglect the laser power fluctuations and the local power losses, the ratio of anti-Stokes to Rayleigh could also be used [86]. Following a similar reasoning as the one just presented it is possible to find that the absolute temperature measurement can also be estimated as:

$$T(z) = \frac{h\Delta\nu}{k_B} ln^{-1} \left[\frac{C_R}{R(z,T)} + 1 \right] \tag{7.14}$$

Noting that similarly to the previous case when the anti-Stokes to Stokes ratio was used, also in this case C_R can be obtained using a reference trace at a known temperature.

7.3.2 Double-ended RDTS

The single-ended interrogation scheme described in the previous subsection is intrinsically sensitive to variations of the sensing fiber's attenuation due to external factors such as splices, connector or bending losses as well as radiation induced losses, given that the RDTS is based on the measurement of the spontaneous Raman power backscattering along the fiber [107][115]. The equations presented in the previous section assume in fact that the differential wavelength-dependent losses are constant in time and uniform along the fiber. This however, is not always the case and there are several real case applications where the fiber is installed in harsh environments where it is exposed to conditions which could spectrally change the fiber's attenuation. The differential WDL is therefore not constant anymore and the single-ended RDTS is not suitable for such applications. This is the case of geothermal wells applications for example, where the differential wavelength dependent attenuation typically varies with time as a consequence of high temperature and hydrogen exposure [116]. It is also the case of nuclear power plants monitoring where the presence of ionizing radiation increases the optical fiber attenuation with time and a spectral dependence [107][117][118]. As introduced in the second Chapter of this thesis, ionizing radiation is also present at particle energy and it is why single-ended RDTS are not suitable for tempera-

ture measurements in such environments. In fact, the ratio anti-Stokes/Stokes or anti-Stokes/Rayleigh is expected to change during the sensor's lifetime due to the exposure to external harsh conditions leading to significant errors in the temperature estimation. The gradual deviation of the temperature trace with respect from the real value is then observed, with this detrimental effect increasing over increasing distances.

To correct the differential WDL dependence of the temperature measurements, several techniques have been proposed in literature [107][116][117][118], among which the use of a double-ended Raman detectio scheme (or "loop configuration") where the sensing optical fiber is connected to the sensor from both ends has been demonstrated to provide a simple and effective solution to compensate differential attenuation issues [107][119]. In such a configuration, pump pulses are alternatively sent into the sensing fiber from both fiber ends. This way the anti-Stokes signal and either the Stokes or the Rayleigh component can be measured in both forward and backward directions. Geometric averages between the acquired traces are then taken in the two opposite directions. Of course in such a configuration, the RDTS needs access to both fiber-ends as schematically depicted in Fig. 7.6.

Figure 7.6: Double-ended RDTS configuration

Assuming that $z = 0$ corresponds to the fiber's input when the forward direction is measured, the anti-Stokes power obtained in both forward $P_{AS}^{Forw}(z)$ and backward $P_{AS}^{Back}(z)$ directions can be expressed as:

$$P_{AS}^{Forw}(z)|_{z=0} = C_{AS}^{Forw} exp[-(\alpha_{AS} + \alpha_P)z]N_\Omega \tag{7.15}$$

$$P_{AS}^{Back}(z)|_{z=L} = C_{AS}^{Forw} exp[-(\alpha_{AS} + \alpha_P)(L - z)]N_\Omega \tag{7.16}$$

where C_{AS}^{Forw} and C_{AS}^{Back} are constants that take into account the differences in the Raman capture factor at the different wavelengths, α_{AS} and α_P are the fiber loss coefficients at the anti-Stokes and pump wavelengths, L is the fiber length and N_Ω is the Bose-Einstein thermal population factor. Forward and backward traces

of the Raman Stokes component are similarly given by:

$$P_S^{Forw}(z)|_{z=0} = C_S^{Forw} exp[-(\alpha_S + \alpha_P)z](1 + N_\Omega) \tag{7.17}$$

$$P_S^{Back}(z)|_{z=L} = C_S^{Forw} exp[-(\alpha_S + \alpha_P)(L - z)](1 + N_\Omega) \tag{7.18}$$

where α_S is the fiber loss coeffcient at the Stokes wavelength.
The ratio between the anti-Stokes and the Stokes powers can then be obtained in both forward $R^{Forw}(z)$ and backward $R^{Back}(z)$ directions as follows:

$$\begin{aligned} R^{Forw}(z) &= \frac{P_{AS}^{Forw}(z)}{P_S^{Forw}(z)} \\ &= \frac{C_{AS}^{Forw}}{C_S^{Forw}} exp[-(\alpha_{AS} - \alpha_S)z] exp\left[\frac{-h\Delta\nu}{k_B T(z)}\right] \end{aligned} \tag{7.19}$$

$$\begin{aligned} R^{Back}(z)|_{z=L} &= \frac{P_{AS}^{Back}(z)}{P_S^{Back}(z)} \\ &= \frac{C_{AS}^{Back}}{C_S^{Back}} exp[-(\alpha_{AS} - \alpha_S)(L - z)] exp\left[\frac{-h\Delta\nu}{k_B T(z)}\right] \end{aligned} \tag{7.20}$$

By taking the geometric mean of these two ratios it is possible to obtain the ratio in loop configuration [107]:

$$\begin{aligned} R^{Loop}(z) &= \sqrt{R^{Forw}(z) \cdot R^{Back}(z)} \\ &= \left[\frac{C_{AS}^{Forw} C_{AS}^{Back}}{C_S^{Forw} C_S^{Back}}\right]^{\frac{1}{2}} exp\left[-(\alpha_{AS} - \alpha_S)\frac{L}{2}\right] exp\left[\frac{-h\Delta\nu}{k_B T(z)}\right] \end{aligned} \tag{7.21}$$

The temperature profile can then be estimated using a reference ratio $R_{Ref}^{Loop}(z)$ obtained in loop configuration at a known temperature T_{ref}, according to:

$$T(z) = \left(\frac{1}{T_{ref}(z)} - \frac{k_B}{h\Delta\nu} ln\left[\frac{R^{Loop}(z,T)}{R_{Ref}^{Loop}(z,T_{Ref})}\right]\right)^{-1} \tag{7.22}$$

An equivalent expression could also be obtained when using the anti-Stokes to Rayleigh ratio.

From Eq. 7.22, it is clear that the use of a double-end configuration cancels out all loss factors depending on the position z along the fiber. This nice feature leads to a self-calibrated temperature measurement which does not depend on the optical loss variation occurring during the sensor's lifetime [107][119]. The geometric mean of the ratios in forward and backward directions indeed allows for a full compensation of any variation in the wavelength dependent losses without the need of any other calibration [107].

To conclude on the RDTS interrogation schemes, the double-ended one certainly has some important advantages over the single-ended one. In particular, the double-ended scheme greatly simplifies the calibration process but also provides a higher accuracy on the temperature measurements with respect to the single-end scheme. Given that the optical losses are intrinsically cancelled out in loop configuration the system becomes robust and insensitive to bending or connector losses as well as any time depending losses as the radiation induced ones. These features make the RDTS system in double-ended configuration highly suitable for temperature measurements and monitoring at high energy physics experiments and facilities.

7.3.3 Limitations of the RDTS

RDTS system have some limitations which are worth to be briefly discussed in this section. A few of these limitations are common with OTDR systems on which the RDTS are in fact based. For example, while the spatial resolution is mainly determined by the pulse width other factors do also influence it. In particular, the bandwidth of the receiver needs to be large enough for the required spatial resolution: bandwidth$> 1/T$ where T is the pulse width. The sampling rate of the ADC might also impact on the spatial resolution by introducing an additional signal loss if it is not properly chosen (especially valid for high spatial resolution). Finally, modal dispersion present in multimode fibers broadens the pulses degrading the spatial resolution in case of long sensing distances.
Other limitations come from the fact that MMF are used for RDTS. The use of multimode fibers is certainly the best choice for RDTS given their higher (generally) numerical aperture and Raman capture factors with respect to SMF. The

Raman scattering generated in MMFs is therefore expected to be higher than in SMFs [120]. Multimode fibers also hold a larger effective area making the onset of nonlinear effects much higher than the thresholds shown by SMFs. For example, the Stimulated Raman Scattering (SRS) unwanted in the case of distributed measurements because impairing the correctness of the measurement, has a threshold about 10 times higher in MMFs with respect to SMFs. As a consequence, it is also possible to sent higher peak power pulses in MMFs (some tens of Watts) with respect to SMFs (1 Watt) without reaching the detrimental SRS threshold.
This said, two factors do limit the performances of RDTS which use MMFs in applications where a meter-scale spatial resolution is requested over long distances: modal dispersion and a higher attenuation coefficient. In fact over long distances above about 10 km , pulse durations of about 10 ns corresponding to 1 m spatial resolution, start to be insufficient from an SNR point of vue since they do not care enough energy to obtain clean traces at the end of the sensing fibers and because of the higher attenuations of MMFs. Modal dispersion of course causes pulses to broaden with the distance. It is also worth mentioning that to keep a meter-scale spatial resolution over longer distances, graded-index MMF fiber are required [108].

In conclusion, the most critical issue limiting RDTS systems is certainly the trade-off between spatial resolution and sensing distance. To overcome this, a high number of averages is required leading to an improved SNR, leading however also to longer measurement times. However, in many applications, involving fire detection or cooling liquid leakage detection, the measurement times need to be short. To cope with this limitation, coding techniques have been presented in literature and a brief introduction about the employment of optical pulse coding for RDTS will be provided in the next section.

7.4 Optical Pulse Coding for RDTS

As mentioned in the previous section, RDTS OTDR-based system suffer from the trade-off between spatial resolution and sensing distance mainly due to the limited SNR when requested to have both high spatial resolution and long sensing distances. To increase the SNR in such systems and enhance their overall

performances, the use of optical coding techniques similar to the ones introduced for OTDRs in Chapter 4 can be implemented [84][85][86][121][122]. In particular, correlation-based coding techniques can be successfully applied to OTDR and RDTS systems. The main principle behind correlation techniques is to spread the signal in the time domain, increasing the average power of the probe signal as well as the backscattered one. This is achieved by launching into the fiber pulse sequences with particular properties which allow to obtain the impulse response of the fiber by correlating the detected signal with the pump pulses following a decoding process. It is therefore possible to perform measurements with a higher dynamic range and improved SNR with a spatial resolution determined by the pulse duration of each pulse contained in the sequences [84][85]. It is worth noticing that this way although the SNR is improved, the onset of nonlinear effects is still avoided.

Among the correlation codes, complementary-correlation Golay codes have been widely and successfully used in OTDR systems. Such codes offer a coding gain (defined in Chapter 4) which is defined as $G_{coding} = \sqrt{L}2$ where L is the length of the code [84]. The SNR enhancement and subsequent noise reduction in the acquired traces can profit a Golay-coded RDTS in different ways. For example, for a given spatial resolution one can obtain a higher temperature accuracy with respect to a single-pulse RDTS with the same measurement time or provide the same temperature accuracy as a single-pulse RDTS but with a shorter measurement time. For a given spatial resolution, a Golay-coded RDTS can also allow to reach longer sensing distances with the same temperature resolution and similar measurement time as a non-coded RDTS.

7.5 Results of Raman distributed temperature measurements in the mixed-field environment

As explained in the theory presented at the beginning of this Chapter, wavelength dependent losses impair the correct measurement of temperature with singled ended RDTS systems and that is why doubled ended systems are needed in such cases. We have also seen that the RIA has a strong dependence on the wavelength and that increasing doses increase the wavelength dependent radiation induced

losses. In a harsh environment with ionizing radiation an RDTS used in double ended configuration is therefore needed if one wished to correctly measure the temperature as Fernandez Fernandez et al. showed for the case of gamma irradiation [107].
In this section, we will show the effectiveness of Raman DTS technology in double ended configuration to accurately measure temperature distributions in harsh environments affected by mixed field radiation as the one created at CHARM.

7.5.1 Experimental setup

For the Raman based distributed temperature measurements at CHARM we have chosen the radiation tolerant multimode (MM) graded index (50/125 μm) MaxCap Bendbright optical fiber by Draka. The fiber has first been characterized at Fraunhofer INT with the setup described in Section 5.1 where it was gamma-irradiated with a dose rate of 0.23 Gy/s up to 11 kGy at a constant temperature of 24°C. The RIA as function of the wavelength for different total accumulated dose values in the fiber is shown in Fig. 7.7.

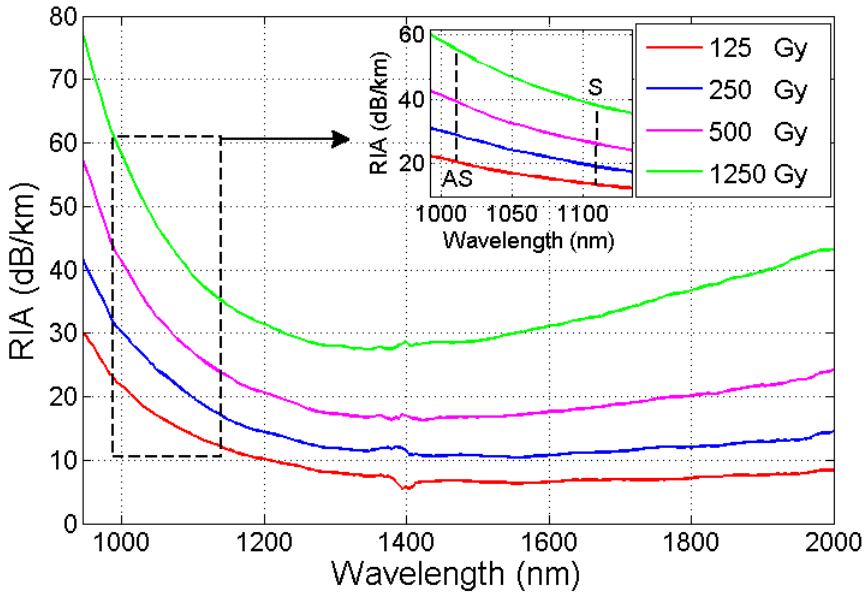

Figure 7.7: RIA as function of wavelenth for the Draka radiation tolerant MM fiber, dose rate: 0.23 Gy/s

Fig. 7.7 clearly shows the wavelength dependence of the RIA and it is evident that the Raman Stokes and anti-Stokes light components will be affected differently depending on the total dose the optical fiber is exposed to. In particular, the difference between the RIA at about 1017 nm (wavelength of the anti-Stokes Raman component) and the one at about 1115 nm (wavelength of the Stokes Raman component) is of about 6-7 dB/km after the fiber accumulates 125 Gy and reaches up to a little more than 16 dB/km after the fiber accumulates 1.25 kGy. The radiation tolerant fiber from Draka has been installed in the facility in such a way that it can be interrogated from both sides from the same rack. The red and green lines in Fig. 7.8 represent the 115 m long path of the optical fiber within the facility. The path runs at two different heights from the ground, 95 cm and 280 cm (back and forth). The fiber is therefore exposed to different radiation environments and respective intensities, reaching a great variety of total accumulated doses depending on its position and on its height, with dose rates ranging from a few μGy/s up to a few tens of mGy/s as shown in Fig. 7.9.

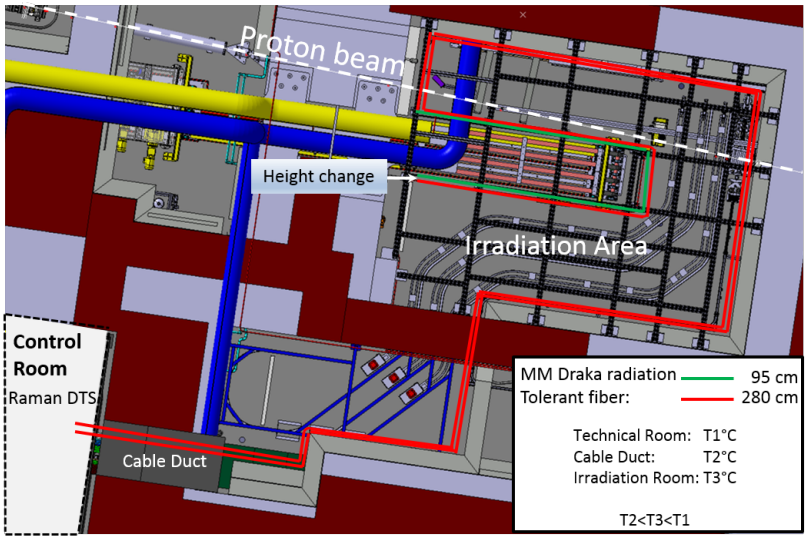

Figure 7.8: 2D view of the CHARM facility including the path of the radiation tolerant MM fiber

For the distributed temperature measurement, a Raman DTS system from INFIBRA Technologies S.r.l. is used. The system operates on graded-index multimode fibers at 1064 nm over a maximum sensing distance of 5 km and with a meter scale spatial resolution. The DTS is located in the control room indicated in both

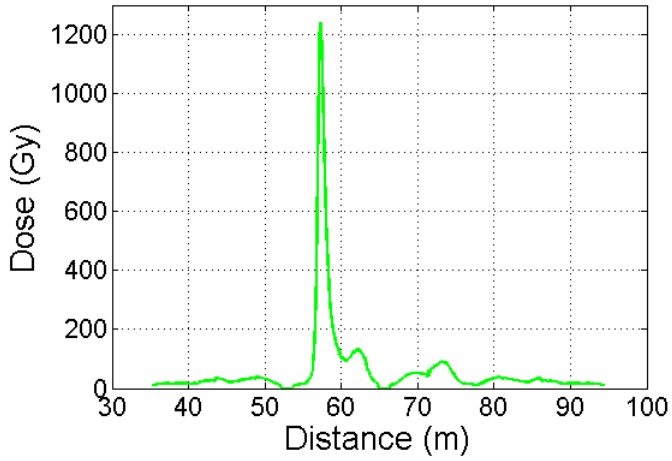

Figure 7.9: Dose profile along the fiber's path

Fig. 6.1 and Fig. 7.8 where both ends of the radiation tolerant fiber reach the same rack as schematically depicted in Fig. 7.10

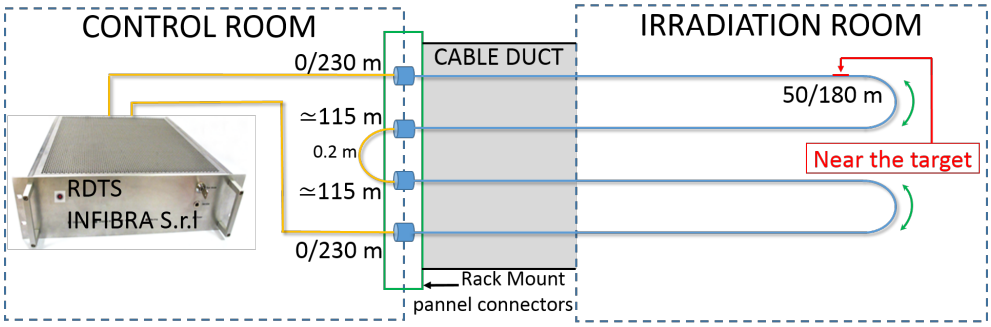

Figure 7.10: RDTS control unit and optical fiber setup

Fig. 7.10 also shows the optical fiber setup and indicates the distances along the radiation tolerant optical fiber's path from the Raman DTS to which it is connected. In particular, the point in which the fiber passes close to the target is indicated at a distance of either 50 m or 180 m from the RDTS depending on the direction of light propagation in the fiber.

7.5.2 Temperature profile

The total accumulated dose along the fiber's path after 24 hours of irradiation, ranges from a few tens of Gy up to the highest value of 1.25 kGy at the position

50 m/180 m within the CHARM facility and from the RDTS, which is where the fiber passes near to the target as depicted in Fig. 7.10. The dose value at that location has been estimated with FLUKA calculations which have been benchmarked by measurements nearby carried out with the RADMON system [9] as well as conventional passive radiation dosimeters.

Fig. 7.11 shows the temperature profiles measured by the Raman DTS along the MM optical fiber before the beginning and at the end of the irradiation within the 24 hour measurement campaign. Note, that while high spatial gradients in the dose rate are present near the target, no significant temperature variations are observed in Fig. 7.11; the Raman DTS spatial sampling resolution is 0.5 meter therefore allowing to fully resolve the higher exposed zone which is about 2 meter wide.

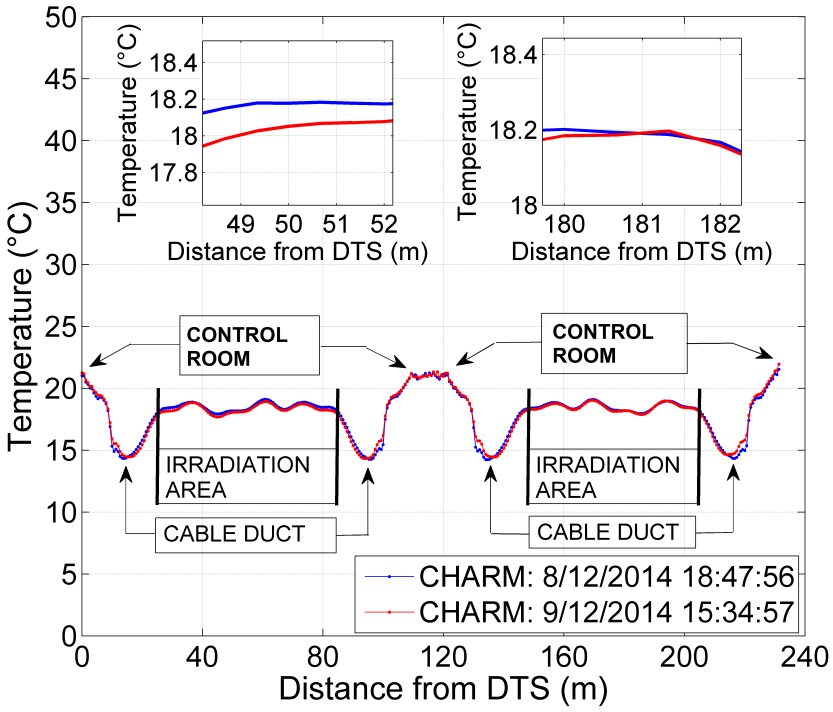

Figure 7.11: Temperature profiles along the radiation tolerant fiber before the beginning and at the end of irradiation

It is also to be noted that the temperature profiles on Fig. 7.11 are approximately symmetric due to the fiber deployment geometry within the facility. The

insets in Fig. 7.11, zooming the fiber sections corresponding to the higher exposed test positions, where the radiation levels ranged from 600 Gy to 1250 Gy, do not show any significant temperature variation during the whole measurement test as expected, since the irradiation area is meant to be kept at constant and uniform temperature by a ventilation system. The only temperature variations which can be observed are those along the path in the cable duct, which is exposed to external daily temperature changes.

In order to point out the presence of radiation induced losses in MM radiation tolerant fibers exposed to high radiation doses, in Fig. 7.12 and Fig. 7.13 we report a zoom of the Raman Stokes and anti-Stokes OTDR traces respectively around the position at a distance of 50 m from the RDTS, at two different times, the beginning of the measurement and after 24 hours of irradiation. It is worth reminding from Chapter 6 that the typical Raman frequency shift is of about 13 THz and therefore the anti-Stokes component's wavelength is around 1017 nm while the Stokes component's wavelength is around 1115 nm.

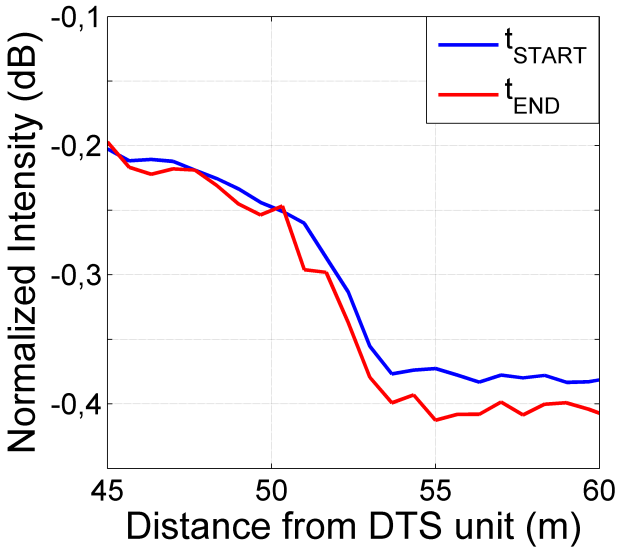

Figure 7.12: Raman Stokes trace at the beginning of the measurement (t_{START}) and after 24 hours (t_{END})

As can be see from Figs. 7.12 and 7.13, while the induced loss is significant on the Stokes trace it is more difficult to appreciate it on the anti-Stokes one. This is due to the fact that when these measurements have been carried out, the radiation tolerant fiber had already been irradiated for several weeks accumulating

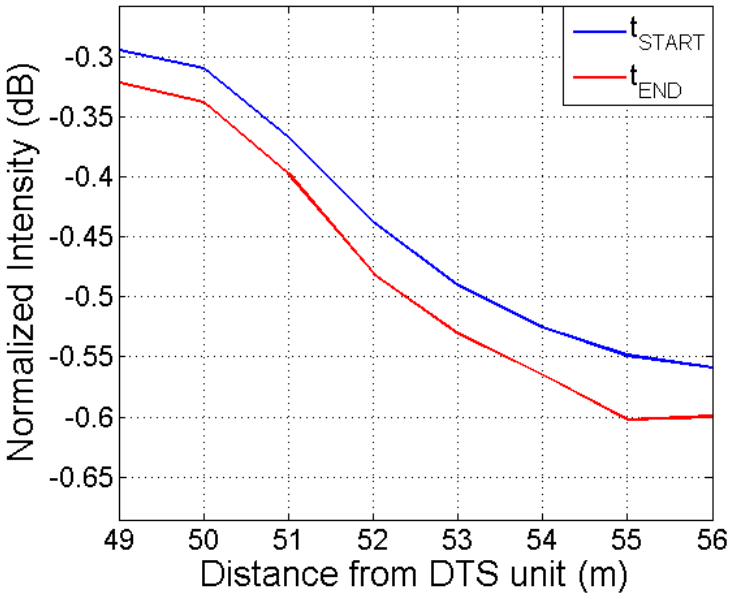

Figure 7.13: Raman anti-Stokes trace at the beginning of the measurement (t_{START}) and after 24 hours (t_{END})

more than 10 kGy of dose explaining also why a loss is observed before the start of irradiation. Due to the previously accumulated dose, the fiber's RIA response to dose had therefore already started to saturate especially for the more sensitive optical wavelengths, which is the case for the anti-Stokes component (~1017 nm) with respect to Stokes component (~1115 nm). Radiation induced losses are however present and give rise to a significant wavelength dependent loss leading to a differential RIA, ΔRIA, of about 14 dB/km. To obtain this value the first step is to calculate the RIA for each component $RIA_{anti-Stokes}$ and RIA_{Stokes} in the following way:

$$RIA_{anti-Stokes} = |A_{aS}^{END} - A_{aS}^{START}| \tag{7.23}$$

and

$$RIA_{Stokes} = |A_{S}^{END} - A_{S}^{START}| \tag{7.24}$$

where A_{aS}^{START}, A_{S}^{START} are the attenuation on the trace before the start of irradiation and A_{aS}^{END}, A_{S}^{END} are the attenuation at the end of irradiation for the anti-Stokes and Stokes components respectively. Theses attenuations, associated to their respective loss event, have been calculated by computing a moving deriva-

tive with respect to a defined step size (of a few meters) along the traces. It is worth noting that the trace before the start of irradiation is obtained by averaging around 90 traces to reduce the noise and obtain a more accurate value of the RIA. Once the radiation induced attenuation for each component $RIA_{anti-Stokes}$ and RIA_{Stokes} have been obtained it is sufficient to to take the absolute value of the difference between them to obtain the differential radiation induced attenuation, $\Delta RIA = |RIA_{Stokes} - RIA_{anti-Stokes}|$.
The obtained ΔRIA is slightly lower than the one calculated from the spectral characterization. It is however worth noticing that the value we obtained cannot be directly compared with the differential RIA value one could calculate from the spectral characterization showed in Fig. 7.7 given that the irradiation conditions were not the same. In fact, the dose rate applied was not the same in both cases and it is known that radiation tolerant (phosphorous-free) fibers exhibit a dose rate dependence in the response of the RIA as function of the total accumulated dose. Another difference lies in the fact that in one of the two cases the fiber had already started to saturate. The evaluation of the WDL is however not the purpose of the RDTS measurements, what matters is that even though a significant WDL and differential RIA are present, the temperature measurements are reliable as it is the case.

By comparing the temperature values obtained by the DTS with the ones obtained by a radiation resistant PT100, a temperature detector available within the CHARM facility, we also verify that the temperature distribution measured by the Raman DTS is reliable and in the spatial regions exposed to higher dose levels as well. For example, Fig. 7.14 compares the Raman DTS temperature measurement with the PT100 placed at a position about 40 m distant from the DTS.

As can be seen, a very good agreement between the two measurement can be appreciated with a maximum difference lower than 0.5°C which is within the measurement accuracy of the PT100.

Finally, Fig. 7.15 reports the standard deviation estimation from the temperature measurements collected by the DTS control unit during the field trial on the fiber placed in the irradiation area. It is worth noticing that the absence of any significant standard deviation change along the sensing fiber demonstrates the

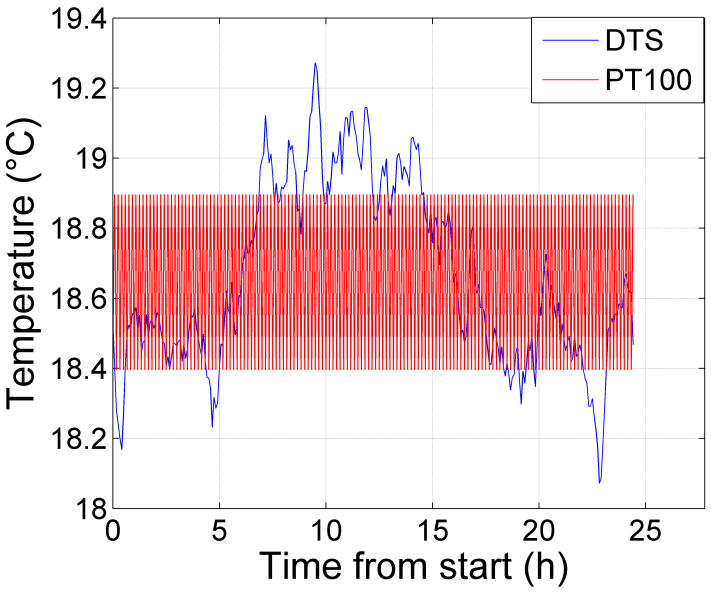

Figure 7.14: Temperature values versus time, comparison between the Raman DTS and the PT100 at position 40 m

distributed temperature measurement stability in the mixed field radiation environment, thus excluding detrimental effects in the highly exposed test positions and ensuring a correct temperature measurement all along the fiber's path up to 115 m of distance.

The successful temperature measurement and analysis previously shown in Figs. 7.11, 7.14 and 7.15 clearly demonstrates that the Raman DTS operating in loop configuration can effectively correct for WDL induced by a mixed field radiation environment in a radiation tolerant optical fiber. While the dynamic range of the DTS from INFIBRA S.r.l was largely sufficient to correctly measure the temperature also in the most distant positions along the fiber's path, it is worth noticing that by selecting a radiation resistant fiber, the RIA will be lower allowing for either longer sensing distances or even higher temperature resolutions.
Except for a temperature characterization of the sensing sytem (RDTS + fiber) to confirm the temperature resolution is not affected by temperature variations, the distributed temperature measurements detailed in this Chapter already demonstrates that a commercial Raman DTS used in double end configuration could be used out of the box to monitor temperature variations in accelerators' tunnels for safety purposes.

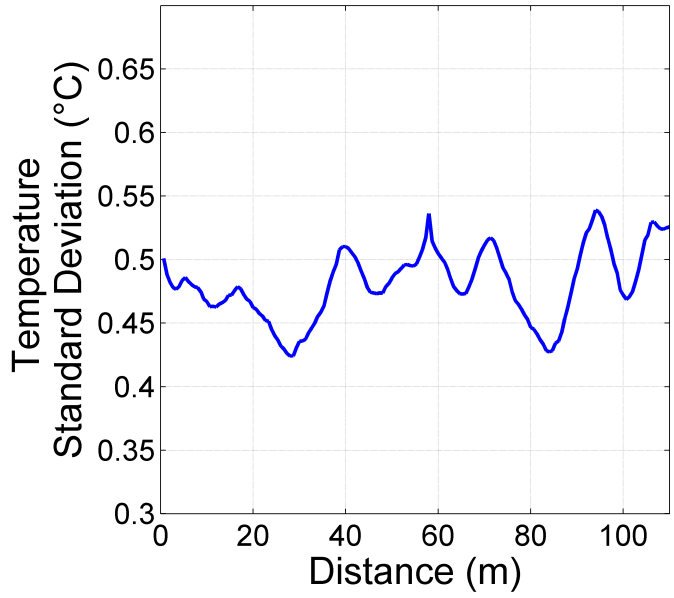

Figure 7.15: Temperature standard deviation versus distance

For the temperature compensation of DOFRS, a temperature characterization of the selected radiation sensitive fiber would of course be required to understand in which way the RIA is affected by temperature variations and as a consequence, how it may be compensated by the temperature profiles provided by the RDTS.

8 Final discussion and further developments

This Thesis dissertation has been focused on the feasibility study of an distributed optical fiber radiation sensing system to be used at high energy physics accelerators and experiments. The multi-disciplinary nature of this research topic requires the knowledge of various theories and fundamental concepts from the fields of radiation physics and photonics. For this reason, Chapters two, three and four have been dedicated to this purpose. In particular, Chapter 2 has provided the fundamental concepts of radiation-matter interaction, dosimetry, radiation detectors and CERN's radiation environment. Chapter three and four were dedicated to providing the fundamentals of radiation effects on Silica-based optical fibers and optical fiber sensors.

In Chapter five the results from the characterization of a selection of P-co-doped fibers have been presented. In particular, two MM GI (50/125 μm) one from j-fiber and the other from OFS as well as two SMF one from Draka and the other from a manufacturer which didn't want to be cited (which we named X), have been irradiated at the ^{60}Co facility at the Fraunhofer-Institut für Naturwissenschaftlich-Technische Trendanalysen in Germany. Except for the SMF from manufacturer X, all fiber have been gamma irradiated at different dose rates such to obtain a full characterization of their response to radiation in terms of RIA as function of the accumulated dose. In double logarithmic scale, most of the fibers presented a linear relation between the RIA and the deposited dose up to a couple of kGy which is quite restrictive although sufficient to monitor low dose areas such as some segments of the LHC where annual doses do not reach more than a few hundreds of Gy. The measurable dose variation range can also be extended by using the non-linear range of the fibers' response curve taking into account higher un-

certainties. This could be achieved by using different fitting models as for example the first-order kinetic model. Almost all the fibers under test saturated at around 20 kGy not allowing to correctly estimate doses above that value. Even though the tested fibers were P-co-doped, a dose rate dependence has been observed on all fibers. In particular, a 30% to 40% variation in the RIA was observed for the j-fiber MMF, 20%-25% for the Draka SMF and up to a factor 2 of variation in RIA due to dose rate for the MMF OFS. Given that our main interest is to measure dose variations rather than absolute dose values, we have considered such dependence as being acceptable under a certain condition if following a specific measurement approach. The approach we have proposed is to consider the slopes of the linear part of the curve corresponding to different dose rates have and verify that these have the same magnitude within a 20% tolerance which is an acceptable uncertainty for our dosimetry application. This was the case for both the j-fiber MM and the Draka SMF but not for the OFS MM which showed strong variations in its sensitivity at different dose rates. The sensitivity of the j-fiber MMF was found to be around 3.5 mdB/m/Gy over the whole range of dose rates at 830 nm and around 1 mdB/m/Gy over the whole range of dose rates at 1312 nm. Draka's SMF was far less sensitive, with sensitivities of about 100 μdB/m/Gy at 1312 nm and about 200 μdB/m/Gy at 1570 nm over the whole range of dose rates.
The most promising fiber among the tested ones, is actually fiber X which showed a high sensitivity to dose (about 4 mdB/m/Gy at 1312 nm and about 5 mdB/m/Gy at 1570 nm) allowing to measure low doses and didn't saturate yet at 60 kGy allowing for high dose measurement although not having a linear response at that point anymore. However, the dose rate dependence of the fiber has not been investigated and it is not possible to comment on that. Unfortunately, fiber X has been developed by its manufacturer for research purposes and is not commercially available. The sample we characterized was kindly provided by Alexey Faustov from the Belgian Nuclear Research Center (SCK-CEN) with whom we compared our characterization results obtaining a good match as detailed in section 5.2.2.
Among the characterized fibers none completely fulfills the requirements for a DOFRS to be used at high energy physics accelerator or experiments, but the j-fiber MMF and the Draka SMF can be considered suitable for dosimetry in areas where the radiation levels are not too high: from a few hundreds of Gy up to the kGy (if exchanged annually) per year. The main difficulty in choosing a com-

mercially available P-co-doped fiber comes from the fact that manufacturers do not disclaim the exact composition of the fiber preventing from making a suitable choice or a pre-selection in the first place. In subsection 5.4.1, we have therefore briefly presented a couple of custom designed fiber which have been jointly developed by Prof. Sylvain Girard and his group at the Laboratoire Hubert Curien of the Université Jean Monnet Saint-Etienne and the Photonics Division of the ixBlue company situated in Lannion (France). For example, a Hole-Assisted optical fiber have been developed, the idea in using such fibers being that a longitudinal gas-loading can be easily performed thanks to the fibers' dedicated holes located in the outer part of the cladding. The proposed treatment procedure is highly interesting for radiation sensing applications given the possibility to regenerate an irradiated fiber link without the need of removing and replacing it, having in addition the option to access it only from one of its two output ends. The use of HAOF as sensing element, could ensure the long life of a HAOF-based radiation sensing system. For this reason, it is planned to test Hole-Assisted optical fibers in irradiation facilities at CERN.

In Chapter six of this Thesis, the results from the distributed optical fiber radiation measurements at the CHARM facility have been presented. To the best of our knowledge, this is the first time that this kind of measurement are performed in such a complex and challenging radiation environment both in terms of particle spectra and dose rate ranges. By means of an OTDR device, distributed measurements of the attenuation profile as function of the dose have been performed on the two MM and the SM Draka fibers previously characterized at Fraunhofer INT with different interrogation and acquisition parameters. Based on the previously presented characterizations which allowed to calculate calibration factors relating the RIA to the dose for each fiber and following an accurate processing, dose profiles along the installed fibers' path have been estimated and compared to FLUKA simulations as well as to RadFETs installed at key positions along the fibers.
In particular, for 5 ns interrogation pulse duration, all the fibers showed consistent results with each other estimating the highest dose peak a factor 2 lower to FLUKA and localizing it correctly along the fiber path. This difference with respect to simulations is however in agreement with previously done benchmarks

with other detectors such as BLM, RPL and RadFETs which also estimated the dose with a factor 2 lower with respect to FLUKA [101]. This is at least partially due to the fact that FLUKA estimates dose in air while the fiber estimates it in SiO_2, hence a conversion factor should be applied. In addition, it needs to be remembered that the estimation of the dose by means of the OTDR-based system implies an averaging of the dose over the spatial resolution. Between the two suitable fibers for dosimetry, the j-fiber MMF and the Draka SMF, due to the limited SNR provided by 5 ns duration pulses, only in the case of the j-fiber MMF which has a higher sensitivity, was it possible to also localize and detect smaller dose peaks.
The j-fiber's dose profile acquired with 5 ns duration pulses and 180 s acquisition time has also been directly compared with a set of RadFETs placed in the surroundings of where the highest doses were to be expected. Only 15% of difference between the measurements of the two sensors has been observed which, taking into account that RadFETs are punctual and the fiber is distributed with a 50 cm spatial resolution, is very promising.
Further distributed measurements with 10 ns pulse duration and 30 s acquisition time have been carried out with the j-fiber MMF allowing to obtain even better results thanks to the higher SNR provided that the high energy carried by longer pulses and even though the acquisition time was shorter. In particular, it was possible to correctly localize and detect dose variation down to 10-15 Gy which is very promising for the monitoring of all low dose segments of the LHC tunnel. Of course, the combination of a 10 ns duration pulse with longer acquisition time would provide even better results since the acquired traces could be more averaged providing an SNR enhancement. In most cases, for distributed optical fiber radiation sensing the acquisition time is not a strong limitation because the measurement rate can be quite low. In fact, the measurement time should be sufficiently long to allow for a dose variation equal or bigger than the dose resolution to take place. For low annual accumulated dose, for example 10 kGy which correspond to an average dose rate of about 0.3 mGy/s, it would take almost 10 hours to reach a detectable dose variation of 10 Gy. As a consequence very long acquisition times can be implemented.

Finally, in Chapter seven, optical fiber distributed temperature measurements

in the mixed-field of CHARM have been presented. After providing the theoretical background to understand Raman-based distributed temperature sensing, the experimental setup including the details about the radiation tolerant fiber's path within CHARM have been shown. The temperature measurements carried out using an RDTS by INFIBRA Technologies S.r.l. have successfully demonstrated that the temperature profile along the fiber's path remains unaffected by the impinging mixed-particle radiation which induced up to 1.25 kGy in a segment of the fiber. This was possible by using the RDTS in double-ended configuration such as to effectively compensate for wavelength-dependent losses. The temperature values obtained by the RDTS were compared with the ones obtained by a radiation resistant PT100 placed at a high dose location. A very good agreement between the two measurement was found with a maximum difference lower than 0.5°C which is within the measurement accuracy of the PT100.

To conclude, with the work presented in this Thesis dissertation it has been demonstrated that distributed optical fiber dosimetry in the challenging and complex mixed-field radiation environment at high energy physics accelerators and experiments, is feasible. The proof of principle has fully succeeded and we can now tackle the challenge of an industrial installation taking into account that some optimizations need to be done. In fact, during the feasibility study some limitations have been pointed out and mainly concern two fundamental aspects of a DOFRS: the one concerning the sensing element which is the fiber and the one related to the control unit of the sensor which in our case was the OTDR device. The characterization of the selected fibers has shown that commercially available P-co-doped fibers offered a range limited to about 20 kGy over which the dose could be estimated, after which they saturated. The SMF from manufacturer X, developed for research purposes, would already potentially allow to estimate the dose up to about 60 kGy. A dose rate dependence, slight an acceptable for some fiber and more strong and unacceptable for another has also been observed although P-co-doped fibers shouldn't exhibit such dependence. A great variety of sensitivities to dose have been evidenced, with up to a maximum factor 40 between different fibers. These observations strongly suggest two possible ways of proceeding to ensure the correct monitoring of the full dose range which can be

found in a real case scenario at particle accelerators: the use of different fibers with different sensitivities to sense areas with different radiation levels and the custom design of optical fibers. Ideally, the combination of these methods should ensure the ability to monitor dose variations extending from a few tens of Gy up to 100 kGy as required. A further optimization could be performed by implementing the use of multiple sources with different wavelengths to be used in the OTDR. Based on the spectral characterization of a fiber, a careful choice of the wavelength could allow for an even more extended dose sensing range. Also, a dedicated processing of traces at different wavelengths could allow to get rid of spurious losses.
This leads us to the limitations observed when using a commercial OTDR. In particular, in our case it was not possible to set acquisition times longer than 180 s which would have allowed to obtain a higher SNR and better detect the dose peaks. In addition, even though certain commercial OTDR are thought for testing long-haul telecommunication links, their dynamic ranges could be improved to cope with the extremely high attenuation values induced by ionizing radiation. This could be achieved by designing highly sophisticated and sensitive APD-based receivers combined with adequate processing and/or implementing the use of pulse codes which would bring an intrinsic SNR enhancement through the coding gain. The custom design of an OTDR-based sensing system might therefore be indicated to deliver the full potential of an DOFRS.
Further measurements and developments will therefore include: the testing at CHARM of custom designed fibers in collaboration with the Laboratoire Hubert Curien of the Université Saint-Etienne, completing the systematic study of the interrogation and acquisition parameters of OTDR-devices as well as starting the prototyping phase of a custom-designed OTDR-based radiation sensing system control unit. To better understand dose deposition in air and silica, FLUKA simulations will be performed. Finally, in collaboration with INFIBRA Technologies S.r.l, the temperature characterization of selected radiation sensitive fibers will be carried out to fully understand the dependence of the RIA on the temperature and the possible implementation of an RDTS-based compensation system.

Bibliography

[1] K. Grattan and T. Sun, "Fibre Optic Sensor Technology: an overview," *Sens. Actuators, A*, vol. 82, no. 1-3, pp. 40–61.

[2] A. Kersey, "A Review of Recent Developments in Fiber Optic Sensor Technology," *Opt.Fiber Technol.*, vol. 2, no. 3, pp. 291–317, 1996.

[3] B. Culshaw, "Fibre Optic Sensor Technology - An Engineering Reality or an Scientific Opportunity," *in Proc. of SPIE, Fourth European Workshop on Optical Fibre Sensors*, vol. 7653, no. 765304, 2010.

[4] F. Yu and S. Yin, "Eds.,Fiber Optic Sensors," *New York: Marcel Decker*, 2002.

[5] International Atomic Energy Agency, "Optimization of SNR Improvement in the Noncoherent OTDR Based on Simplex CodesAssessment and management of ageing of major nuclear power plant components important to safety: In-containment instrumentation and control cables," *Tech.Rep. IAEA-TECDOC-1188, Corning Cable Systems LLC, December 2000. http://www-pub.iaea.org/MTCD/publications/PDF/te*$_1$*188v1*$_p$*rn.pdf.*, vol. 1, 2000.

[6] M. Brugger *et al.*, "REVIEW OF CRITICAL RADIATION AREAS FOR LHC ELECTRONICS AND MITIGATION ACTIONS. RADIATION MONITORING AND FIRST RESULTS ," *Proceedings of Chamonix 2010 workshop on LHC Performance*, 2010.

[7] J. Saraiva and M. Brugger, "Radiation Levels at CERN's Injectors and their Impact on Electronic Equipment," *11th International Topical Meeting on Nuclear Applications of Accelerators*, 2013.

[8] J. Mekki, M. Brugger, and R. Alia, "Radiation Levels at CERN's Injectors and their Impact on Electronic Equipment," *CHARM: A New Mixed Field Facility at CERN for Radiation Test in Ground, Atmospheric, space and Accelerator representative environments*, 2015.

[9] G.Spiezia *et al.*, "The LHC Radiation Monitoring System - RadMon," 2011.

[10] B. Evans and G. Sigel, *IEEE Trans. Nucl. Sci.*, vol. 21, p. 113, 1974.

[11] B.D. Evans and G.H. Sigel, "Radiation Resistant Fiber Optic Materials and Waveguides," *IEEE Trans. Nucl. Sci.*, vol. 22, pp. 2462–2467, 1975.

[12] P. Mattern *et al.*, *IEEE Trans. Nucl. Sci.*, vol. NS-21, p. 81, 1974.

[13] E. Friebele, G. Sigel, and M. Gingerich, "Radiation response of fiber optic waveguides in the 0.4 to 1.7 μ region," *IEEE Trans. Nucl. Sci.*, vol. 25, pp. 1261–1266, 1978.

[14] S. Girard *et al.*, "Radiation effects on silica-based optical fibers: Recent advances and future challenges," *IEEE Trans. Nucl. Sci.*, vol. 60, no. 3, pp. 2015–2036, 2013.

[15] J. Polf *et al.*, "A real-time, fibre optic dosimetry system using Al_2O_3 fibres," *Radiation Protection Dosimetry*, vol. 100, no. 1-4, pp. 301–304, 2002.

[16] S. Girard *et al.*, "Feasibility of radiation dosimetry with phosphorus-doped optical fibers in the ultraviolet and visible domain," *Journal of Non-Crystalline Solids*, vol. 357, no. 8, pp. 1871–1874, 2011.

[17] B. Evans, "The Fiber Optic Dosimeter on the Navigational Technology Satellite 2," *IEEE Trans. Nucl. Sci.*, vol. 25, pp. 1619–1624, 1978.

[18] H. Henschel *et al.*, "Fibre optic radiation sensor systems for particle accelerators," *Nuclear Instruments and Methods in Physics Research A*, 2004.

[19] A.Holmes-Siedle and L.Adams, *Handbook of radiation effects*, 1993.

[20] E.J.Friebele, "Optical Fiber Waveguides In Radiation Environments," *Optical Engineering*, 1979.

[21] K. Krane, *Introductory Nuclear Physics, 3rd Edition*, 1987.

[22] J.Beringer *et al.*, "The Review of Particle Physics," *Phys. Rev.D86, 010001*, 2012.

[23] U. Amaldi and G.Kraft, "http://cerncourier.com/cws/article/cern/29777," *CERN Courier*, 2006.

[24] G. Knoll, *Radiation Detection and Measurement 3rd Edition*, 1999.

[25] F.Wrobel, "Short Course Notebook - New Challenges for Radiation Tolerance Assessment," *Conférence RADECS 2005*, 2005.

[26] MIT OpenCourseWare (OWC), "Nuclear Science and Engineering, Introduction to Ionizing Radiation, Lecture Notes."

[27] F.Berghmans *et al.*, *An Introduction to Radiation Effects on Optical Components and Fiber Optic Sensors*, 2008.

[28] A. Vasilescu and G. Lindstroem, "Displacement damage in silicon, on-line compilation," *http://rd50.web.cern.ch/RD50/NIEL/default.html*.

[29] CERN, "http://home.web.cern.ch/about/accelerators," *CERN*, 2013.

[30] T. Böhlen *et al.*, "The FLUKA Code: Developments and Challenges for High Energy and Medical Applications," *Nuclear Data Sheets*, vol. 120, pp. 211–214, 2014.

[31] H. Bach and N. Neuroth, "The Properties of Optical Glass." *Springer-Verlag*, 1995.

[32] S. Agnello, "Gamma ray induced processes of point defect conversion in silica," *Universita di Palermo*, 2000.

[33] D. Griscom, "Intrinsic and extrinsic point defects in $a-SiO_2$ in "The Physics and Technology of Amorphous SiO_2"," *R. A. B. Devine, Ed. New York: Plenum*, 1988.

[34] T. Ma and P. Dressendorfer, "Ionizing Radiation Effects in MOS Devices and Circuits," *New York: Wiley-Interscience*, 1989.

[35] E. Lell *et al.*, "Radiation effects in quartz, silica and glasses," *Progr. Ceramic. Sci., New York*, 1966.

[36] E. Friebele *et al.*, "Optical fiber waveguides in radiation environments, II," *Nuclear Instruments and Methods in Physics Research Section B: Beam Interactions with Materials and Atoms*, 1984.

[37] K. Jang *et al.*, "Measurement of Cerenkov radiation induced by the gamma-rays of Co-60 therapy units using wavelength shifting fiber," *Sensors (Basel)*, 2014.

[38] K.W. Jang *et al.*, "Fast-neutron-induced changes in quartz and vitreous silica," *Phys. Rev. B*, 1958.

[39] G. Origlio, "Properties and Radiation Response of Optical Fibers: Role of Dopants," *PhD Dissertation, Université Jean Monnet of Saint-Etienne and Università Degli Studio of Palermo*, 2009.

[40] M. Cannas, L. Vaccaro, and B. Boizot, "Spectroscopic parameters related to non-bridging oxygen hole centers in amorphous-SiO_2," *Journal of Non-Crystalline Solids*, 2006.

[41] S. Girard *et al.*, "γ-rays and pulsed X-ray radiation responses of nitrogen, germanium doped and pure silica core optical fibers," *Nucl. Instrum. Meth. Phys. Res. B*, 2004.

[42] B. Brichard *et al.*, "Radiation-hardening techniques of dedicated optical fibres used in plasma diagnostic systems in ITER," *J. Nucl. Mater.*, 2004.

[43] P. Chernov, "Spectroscopic manifestations of self-trapped holes in silica," *Phys. Stat. Sol.*, 1989.

[44] E. J. Friebele, "Correlation of Single Mode Fiber Fabrication Factors and Radiation Response," *Final Rep., NRL/MR/6505-92-6939*, 1991.

[45] E. Friebele *et al.*, "Correlation of single-mode fiber radiation response and fabrication parameters," *Appl. Opt.*, 1991.

[46] M. Ott, "Radiation effects data on commercially available optical fiber: Database summary," *in Proc. IEEE NSREC Data Workshop*, 2002.

[47] G. Keiser, "Optical Fiber Communications," *New York: McGraw-Hill*, 1991.

[48] D. Ehrt, P. Ebeling, and U. Natura, "UV Transmission and radiation-induced defects in phosphate and fluoride-phosphate glasses," *J. Non-Cryst. Solids*, 2000.

[49] D. Griscom *et al.*, "Fundamental defect centers in glass: Electron spin resonance and optical absorption studies of irradiated phosphorus-doped silica glass and optical fibers," *J. Appl. Phys.*, 1983.

[50] M. Paul *et al.*, "Radiation response behavior of high phosphorous doped step index multimode optical fibers under low dose gamma irradiation," *J.Non-Cryst. Solids*, 2009.

[51] A.Faustov *et al.*, "Comparison of Gamma-Radiation Induced Attenuation in Al-Doped, P-Doped and Ge-Doped Fibres for Dosimetry," *IEEE Transactions on Nuclear Science*, vol. 60, no. 4, 2013.

[52] M. Van Uffelen, "Modélisation de Systèmes D'acquisition Et De Transmission à Fibres Optiques Destinés à Fonctionner En Environnement Nucléaire," *Thèse de Doctorat, Université de Paris XI, Paris*, 2001.

[53] P. Borgermans, "Spectral and Kinetic Analysis of Radiation Induced Optical Attenuation in Silica: Towards Intrinsic Fiber Optic Dosimetry?" *Thèse de doctorat, Vrije Universiteit, Brussels*, 2001.

[54] S. Girard, "Analyse De LA Réponse Des Fibres Optiques Soumises à Divers Enivronnements Radiatifs," *Thèse de doctorat, Univesité de Saint-Etienne, France*, 2003.

[55] D. L. Griscom, M. E. Gingerich, and E. J. Friebele, "Model for the dose, dose-rate and temperature dependence of radiation-induced loss in optical fibers," *IEEE Trans. Nucl. Sci.*, 1994.

[56] H. Henschel, O. Köhn, and H. Schmidt, "Influence of dose rate on radiation induced loss in optical fibres," *in Proc. SPIE Ser. 1399*, 1991.

[57] E. Friebele, C. Askins, and M. Gingerich, "Effect of low dose rate irradiation on doped silica core optical fibers," *Appl. Opt.*, 1984.

[58] T. Wijnands *et al.*, "Optical absorption in commercial single mode optical fibers in a high energy physics radiation field," *IEEE Trans. Nucl. Sci.*, 2008.

[59] International and Electrotechnical and Commission (IEC), "Technical report: Nuclear radiation - Fibre optic guidance," *IEC, Geneva*, 2003.

[60] J. Kuhnhenn, S. Höffgen, and U. Weinand, "Quality Assurance for Irradiation Tests of Optical Fibers: Uncertainty and Reproducibility," *IEEE Transactions on Nuclear Science*, vol. 56, no. 4, 2009.

[61] S. Girard *et al.*, "Combined High Dose and Temperature Radiation Effects on Multimode Silica-Based Optical Fibers," *IEEE Trans. Nucl. Sci.*, 2013.

[62] H. Henschel, O. Köhn, and H. Schmidt, "Optical fibres as radiation dosimeters," *Nuclear Instruments and Methods in Physics Research B69*, 1992.

[63] H. Henschel and O. Köhn, "Regeneration of Irradiated Optical Fibres by Photobleaching?" *Proceedings of RADECS*, 1999.

[64] E. Friebele and M. Gingerich, "Photobleaching effects in optical fiber waveguides," *Applied optics*, vol. 20, no. 19, pp. 3448–3452, 1981.

[65] E. Guillermain, J. Kuhnhenn, D. Ricci, and U. Weinand, "Macro-bending influence on radiation induced attenuation measurement in optical fibres," *IEEE Transactions on Nuclear Science*, vol. 61, 2014.

[66] D. Griscom, "Radiation hardening of pure-silica-core optical fibers: Reduction of induced absorption bands associated with self-trapped holes," *Appl. Phys. Lett.*, 1997.

[67] H. Henschel *et al.*, "Comparison between fast neutron and gamma irradiation of optical fibres," *IEEE Trans. Nucl. Sci.*, 1998.

[68] K. Kikuchi *et al.*, "Measurement of Raman Scattering in Single-Mode Optical Fiber by Time-Domain Reflectometry," *IEEE J.Quantum Electron.*, vol. 24, no. 10, pp. 1973–1975, 1988.

[69] G. Agrawal, *Nonlinear Fiber Optics 4th ed.*, 2007.

[70] R. Boyd, "Nonlinear Optics, 2nd ed." *San Diego, CA - London: Academic Press*, 2003.

[71] K. Hill and G. Meltz, "Fiber Bragg Grating Technology Fundamentals and Overview," *IEEE J. Lightw. Technol.*, vol. 15, no. 8, pp. 1263–1276, 1997.

[72] A. Kersey *et al.*, "Fiber Bragg Grating Technology Fundamentals and Overview," *IEEE J. Lightw. Technol.*, vol. 15, no. 8, pp. 1442–1463, 1997.

[73] R. Measures, "Structural Monitoring with Fiber Optic Technology," *California: Academic Press*, 2001.

[74] J. Dakin, "Distributed Optical Fiber Sensors," *in Fiber Optic Sensors, R. Willsch and R. T. Kersten, Eds. Bellingham, WA: SPIE, SPIE Milestone Series*, vol. MS108, pp. 284–311, 1995.

[75] M. Niklès, "Fibre optic distributed sensing systems: Perspectives and challenges for high performance applications," *presented at the 3rd EWOFS*, vol. SPIE 6619, pp. 284–311, 2007.

[76] A. Rogers, "Distributed optical-fibre sensing," *Meas. Sci. Technol.*, vol. 10, no. 8, pp. R75–R99, 1999.

[77] D. Derickson, "Fiber Optic Test and Measurement," *New York, USA: Prentice Hall*, 1997.

[78] K. Aoyama *et al.*, "Optical Time Domain Reflectometry in a Single-Mode Fiber," *IEEE J. Quantum. Electron.*, vol. QE-17, no. 6, pp. 862–868, 1981.

[79] R. Hui and M. O'Sullivan, "Fiber Optic Measurement Techniques," *San Diego, CA, USA: Academic Press*, 2009.

[80] G. Mussi *et al.*, "−152.5 dB sensitivity high dynamic-range optical frequency-domain reflectometry," *Electron. Lett.*, vol. 32, no. 10, pp. 926–927, 1996.

[81] R. Bernini *et al.*, "Frequency-domain approach to distributed fiber-optic Brillouin sensing," *Opt. Lett.*, vol. 27, no. 5, pp. 288–290, 2002.

[82] R. Bernini and other, "An Accurate High-Resolution Technique for Distributed Sensing Based on Frequency-Domain Brillouin Scattering," *IEEE Photon. Technol. Lett.*, vol. 18, no. 1, pp. 280–282, 2006.

[83] V. Lanticq *et al.*, "Distributed Optical Fibre Sensors for Structural Health Monitoring: Upcoming Challenges, Optical Fibre, New Developments," *Vukovar Croatia: Christophe Lethien, In-Tech*, 2009.

[84] M. Nazarathy *et al.*, "Real-time long-range complementary correlation optical time-domain reflectometer," *J.Lightwave Technol.*, vol. 7, no. 1, pp. 24–38, 1989.

[85] M. Jones, "Using Simplex codes to improve OTDR Sensitivity," *IEEE Photon. Technol. Lett.*, vol. 5, no. 7, pp. 822–824, 1993.

[86] H. Lee *et al.*, "1.65 μm Raman-based distributed temperature sensor," *Electron. Lett.*, vol. 35, no. 21, pp. 1869–1870, 1999.

[87] M. Golay, "Complementary Series," *IRE Trans. Inf. Theory*, vol. 7, no. 2, pp. 82–87, 1961.

[88] M. Harwit and N. Sloane, "Hadamard Transform Optics," *New York: Acamedic Press*, 1979.

[89] L. Cheng *et al.*, "An improved design for optimum double-coding in Hadamard transform spectroscopy," *Meas.Sci.Technol.*, vol. 2, no. 12, pp. 1177–1180, 1991.

[90] D. Lee *et al.*, "Analysis and Experimental Demonstration of Simplex Coding Technique for SNR Enhancement of OTDR," *in Proc.of IEEE LTIMC 2004*, 2004.

[91] D. Lee *et al.*, "Optimization of SNR Improvement in the Noncoherent OTDR Based on Simplex Codes," *J. Lightwave Technol.*, vol. 24, no. 1, pp. 322–328, 2006.

[92] J. Park *et al.*, "Raman-Based Distributed Temperature Sensor With Simplex Coding and Link Optimization," *IEEE Photonics Technology Leters*, 2006.

[93] W. Gaebler, "Characteristics of fiber optic radiation detectors," *SPIE 403*, 1983.

[94] H. Henschel *et al.*, *IEEE Trans. Nucl. Sci.*, 1988.

[95] "Nuclear Radiation - Fibre Optic Guidance," *IEC TR 62283, Technical Report*, 2003.

[96] E. Friebele *et al.*, "Procedure for Measuring Radiation-Induced Attenuation in Optical Fibers and Optical Cables ," *NATO Nuclear Effects Task Group A/C 243, Panel IV (RSG.12)*, 1992.

[97] E. Reignier *et al.*, "Low-Dose Radiation-Induced Attenuation at InfraRed Wavelengths for P-Doped, Ge-Doped and Pure Silica-Core Optical FIbers," *IEEE Transactions on Nuclear Science*, vol. 54, no. 4, 2007.

[98] S.Girard *et al.*, "On-site Regenration Technique for Hola-Assisted Optical Fibers Used In Nuclear Facilities," *Nuclear and Space Radiation Effects Conference (NSREC)*, 2015.

[99] D. Di Francesca, "Role of Dopants, Interstitial O_2 and Temperature in the Effects of Irradiation on Silica-based Optical Fibers," 2015.

[100] D. Di Francesca *et al.*, "Cerium Codoping Effect on the Radiation Response of Germanosilicate and Phosphosilicate Multimode Optical Fibers," *RADiations Effects on Components and Systems Conference (RADECS)*, 2015.

[101] J.Mekki *et al.*, "CHARM: A New Mixed Field Facility at CERN for Radiation Test in Ground, Atmospheric, Space and Acceerator Representative Enivornments," *RADECS 2015 Proceedings*, 2015.

[102] P. Boisseaux-Bourgeois, "RadFET measurements CHARM 2015," *R2E, Internal report*, 2015.

[103] E. Ru and P. Etchegoin, "Principles of Surface Enhanced Raman Spectroscopy," *1st ed. Amsterdam - Oxford: Elsevier*, 2009.

[104] M. Islam, "Raman amplifiers for Telecommunications 1, Physical principles," *New York, US: Springer-Verlag*, 2004.

[105] E. Udd and W. Spillman, "Fiber Optic Sensors, An Introduction for Engineers and Scientists," *2nd ed. John Wiley & Sons, Inc. Hoboken, New Jersey*, 2011.

[106] R. Stolen *et al.*, "Raman oscillation in glass optical waveguide," *Applied Physics Letters*, vol. 20, pp. 60–62, 1972.

[107] A. Fernandez Fernandez *et al.*, "Radiation-tolerant Raman distributed temperature monitoring system for large nuclear infrastructures," *IEEE Transactions in Nuclear Science*, vol. 52, pp. 2689 – 2694, 2005.

[108] M. Farahani and T. Gogolla, "Spontaneous Raman Scattering in Optical Fibers with Modulated Probe Light for Distributed Temperature Raman Remote Sensing," *Journal of Lightwave Technology*, vol. 17, no. 8, pp. 1379–1391, 1999.

[109] A. Hartog and A. Leach, "Distributed temperature sensing in solid-core fibres," *Electronics Letters*, vol. 21, no. 23, pp. 1061–1062, 1985.

[110] B. Culshaw, "Optical fiber sensor technologies: opportunities and-perhaps-pitfalls," *J. Lightwave Technol.*, vol. 22, no. 1, pp. 39–50, 2004.

[111] P. Samson, "Analysis of the wavelength dependence of Raman backscatter in optical fiber thermometry," *Electron. Lett.*, vol. 26, pp. 163–165, 1990.

[112] M. A. Soto *et al.*, "Distributed temperature sensor system based on Raman scattering using correlation-codes," *Electron. Lett.*, vol. 43, no. 16, pp. 862–864, 2007.

[113] A. Signorini *et al.*, "40 km long-range Raman-based distributed temperature sensor with meter-scale spatial resolutions," *Optical Fiber Communication Conference (OFC), San Diego, US*, 2010.

[114] J. Dakin *et al.*, "Distributed optical fiber Raman temperature sensor using a semiconductor light-source and detector," *Electron. Lett.*, vol. 21, pp. 569–570, 1985.

[115] K. Suh and C. Lee, "Auto-correction method for differential attenuation in a fiber-optic distributed-temperature sensor," *Opt. Lett.*, vol. 33, no. 16, pp. 1845–1847, 2008.

[116] M. Jaaskelainen, "Temperature Monitoring of Geothermal Energy Wells," *in Proceedings of Fourth European Workshop on Optical Fiber Sensors*, 2010.

[117] A. Kimura *et al.*, "Application of a Raman distributed temperature sensor to the experimental fastreactor JOYO with correction techniques," *Meas. Sci. Technol.*, vol. 12, no. 7, pp. 966–973, 2001.

[118] E. Takada *et al.*, "Correction Techniques of Radiation Induced Errors for Raman Distributed Temperature Sensor and Experiment at the Experimental Fast Reactor: JOYO," *J.Nucl.Sci.Technol.*, vol. 35, no. 8, pp. 547–553, 1998.

[119] S. Tyler *et al.*, "Environmental temperature sensing using Raman spectra DTS fiber-optics methods," *Water Resour.Res.*, vol. 45, p. W00D23, 2009.

[120] J. Niu and J. Xu, "Coupling efficiency of laser beam to multimode fiber," *Opt. Commun*, vol. 274, pp. 315–319, 2007.

[121] G. Bolognini *et al.*, "Improved Performance in Raman-BAsed Distributed Temperature Sensing With Coded OTDR and Discrete Raman Amplification," *in Proc. of International Conference on Optical Fiber Sensors*, 2006.

[122] G. Bolognini *et al.*, "Performance Enhancement of Raman-Based Distributed Temperature Sensors Using Simplex Codes," *in Proc. of International Conference on Optical Fiber Sensors*, 2006.

List of publications

International journals

1. **I. Toccafondo**, A. Thornton, E. Guillermain, J. Kuhnhenn, J. Mekki, M. Brugger and F. Di Pasquale, "Distributed Optical Fiber Radiation Sensing at CERN High Energy AcceleRator Mixed Field Facility (CHARM)", *IEEE Transactions on Nuclear Sciences*, to be submitted, 2015

2. **I. Toccafondo**, T. Nannipieri, A. Signorini, E. Guillermain, J. Kuhnhenn, M. Brugger and F. Di Pasquale, "Raman Distributed Temperature Sensing at CERN", *IEEE Photonics Technology Letters*, Vol. 27, Issue 20, pp. 2182-2185, 2015

3. Y. Muanenda, M. Taki, T. Nannipieri, A. Signorini, C.J. Oton, F. Zaidi, **I. Toccafondo** and F. Di Pasquale, "Advanced Coding Techniques for Long-Range Raman/BOTDA Distributed Strain and Temperature Measurements", submitted to *IEEE Journal of Lightwave Technology*, 2015

4. M. Taki, Y. Seifu Muanenda, **I. Toccafondo**, A. Signorini, T. Nannipieri, and F. Di Pasquale, "Optimized Hybrid Raman/Fast-BOTDA Sensor for Temperature and Strain Measurements in Large Infrastructures", *IEEE Sensors Journal*, Vol. 14, No. 12, 2014.

5. M. Taki, F. Zaidi, **I. Toccafondo**, T. Nannipieri, A. Signorini, S. Faralli, and F. Di Pasquale, "High-performance hybrid Raman/fiberBragg grating fiber-optic sensor based on simplex cyclic pulse coding", *Optics Letters*, Vol. 38, Issue 4, pp. 471-473, (2013)

6. **I. Toccafondo**, M. Taki, A. Signorini, F. Zaidi, T. Nannipieri, S. Faralli and

F. Di Pasquale, "Hybrid Raman/FBG Sensor for Distributed Temperature and Discrete Dynamic Strain Measurements", *Optics Letters*, Vol.37, Issue 21, pp. 4434-4436, 2012

Peer-reviewed conference proceedings

1. **I. Toccafondo**, T. Nannipieri, A. Signorini, E. Guillermain, J. Kuhnhenn, M. Brugger and F. Di Pasquale, "Raman distributed temperature measurement at CERN high energy accelerator mixed field radiation test facility (CHARM)", presented at and to be published in proceedings of *24th International Conference on Optical Fibre Sensors (OFS)*, 28th September - 2nd October, Curitiba, Brazil

2. **I. Toccafondo**, A. Thornton, E. Guillermain, J. Kuhnhenn, J. Mekki, M. Brugger and F. Di Pasquale, "Distributed Optical Fiber Radiation Sensing at CERN High Energy AcceleRator Mixed Field Facility (CHARM)", presented at and to be published in proceedings of *RADECS 2015*, 14th-18th September 2015, Moscow, Russia

3. **I. Toccafondo**, M. Brugger, F. Di Pasquale, E. Guillermain, J. Kuhnhenn, "First steps towards a distributed optical fiber radiation sensing system", in proceedings of *International Conference on Space Optics, ICSO 2014*, 7th-10th October 2014, Tenerife, Canary Islands, Spain

4. Y.Muanenda, M.Taki, **I.Toccafondo**, A.Signorini, T.Nannipieri, C.J. Oton, F.Di Pasquale, "Cyclic pulse coding for hybrid fast BOTDA/Raman sensor", Proc. SPIE 9157 of *23rd International Conference on Optical Fibre Sensors*, 2nd June 2014, Santander, Spain

5. A. Signorini, **I. Toccafondo**, F. Zaidi, M. Taki, T. Nannipieri, F. Di Pasquale, "Hybrid Fiber Optic Sensors for Simultaneous Distributed and Dynamic Discrete Measurement", in proceedings of *Symposium on Advanced Distributed Optical Fiber Sensor Systems for Security and Safety Applications: Hybrid Distributed Optical Fiber Sensors (FW2I)*, Frontiers in Optics, 6th-10th October 2013, Orlando, Florida, United States